Diplomarbeit

Master's Thesis

Numerical Analysis of Rock Mass Falls using PFC^{3D}
A comparison of two cases:
Thurwieser Rock Avalanche and Frank Slide

ausgeführt zum Zwecke der Erlangung des akademischen Grades
eines Diplom-Ingenieurs unter der Leitung von

Univ.Prof. Dipl.-Ing. Dr.techn. Rainer Poisel
E203
Institut für Ingenieurgeologie, TU-Wien
und
Univ.Ass. Dipl.-Ing. Dr.techn. Alexander Preh
E203
Institut für Ingenieurgeologie, TU-Wien

eingereicht an der Technischen Universität Wien
Fakultät für Bauingenieurwesen
von

Onur KOÇ
0427086
Kenyongasse 23-25 / 619
1070 Wien

Wien, im Februar 2008

Acknowledgements

I would like to express my deep gratitude towards Univ. Prof. Dipl.-Ing. Dr.tech. Rainer Poisel, who has given me an opportunity to be a part of “Benchmarking Exercise” project. His great tolerance with my never-ending questions and his excellent supervision made this work possible.

Second of all, I would like to thank Dipl.-Ing. Dr.tech. Alexander Preh for his marvelous patience with even my irrelevant problems and for his outstanding guidance through out this work.

Furthermore, I am indebted to all institute employees for their kind attitude towards me.

I am grateful to my friend Ozan Yalniz, who has supported me not just by our long-distance telephone talks, but also by proofreading the entire work for me.

I cannot forget my friend Kurt Mair am Tinkhof. He has helped me a lot through out this work. I wish to thank him for standing by me and encouraging me.

A special thank should go to my family and to my fiancé Zeynep Özbek. Without their support I could not even imagine to finish this work.

Abstract

Rock mass falls, especially in mountain ranges like the Alps, belong to natural morphological phenomena. If they occur near population areas, they comprise great hazard to human life and to the nearby infrastructure. Thus it is very important to predict any possible occurrence and foresee the likely pathway of rock avalanches, so that precautions could be taken just in time.

In order to evaluate the qualification of the numerical program *PFC* modified for run out modeling two cases were selected for comparing reality and simulation: Punta Thurwieser rock avalanche with a steep Fahrböschung and Frank Slide showing a gentle Fahrböschung.

PFC^{3D} (Particle Flow Code in 3 Dimensions) is a discontinuum mechanics program developed by ITASCA CONSULTING GROUP. *PFC* models the movements and interactions of stressed assemblies of spherical particles either in or getting contact with wall elements. The particles may be bonded together at their contact points to represent a solid that may fracture due to progressive bond breakage. Every particle is checked on contact with every other particle at every timestep. Thus PFC can simulate not only failure mechanisms of rock slopes but also the run out of a detached and fractured rock mass. The run out model using *PFC* consists of two basic elements: two dimensional wall elements which represent the non moved ground and spherical elements representing the rock mass particles in motion.

Parameter variations showed that the parameters necessary to get results coinciding with observations in nature in the particular cases are completely different. The diagrams of mean particle velocities and kinetic energy over time clearly point out that some 30 percent of total kinetic energy is rotational kinetic energy in Thurwieser, whereas the contribution of rotational kinetic energy in Frank Slide is zero. Thus Frank run out is a real “slide” of a coherent mass, whilst Punta Thurwieser run out is a rock mass fall with much internal movement.

Therefore, the prediction of the run out kinematics and the fixing of the parameters is a demanding task in each case when modeling run outs.

Table of Contents

1 Landslides, Rock Mass Falls

In geotechnical terminology the term landslide is often expressed differently. As a general definition, the United States Geological Survey (USGS) has introduced "Landslides" as:

"A wide range of ground movement, such as rock falls, deep failure of slopes, and shallow debris flows. Although gravity acting on an over-steepened slope is the primary reason for a landslide, there are other contributing factors:

- erosion by rivers, glaciers, or ocean waves create oversteepened slopes
- rock and soil slopes are weakened through saturation by snowmelt or heavy rains
- earthquakes create stresses that make weak slopes fail
- earthquakes of magnitude 4.0 and greater have been known to trigger landslides
- volcanic eruptions produce loose ash deposits, heavy rain, and debris flows
- excess weight from accumulation of rain or snow, stockpiling of rock or ore, from waste piles, or from man-made structures may stress weak slopes to failure and other structures (USGS, 2007)"

On the other hand rock mass falls are special types of landslides, which occur on rock material as the name implies.

1.1 Landslides and their Classification

The landslides in general term classified by their two characters:

- by material (e.g. rock, earth, debris)
- by the type of movement (e.g. rock fall, debris flow) (VARNES, 1978)

By material, landslides are divided into three categories (after VARNES), namely: rock (a hard or firm mass that was intact and in its natural place before the initiation of movement), earth (describes material in which 80 percent or more of the particles are smaller than 2 mm) and debris (contains a significant proportion of coarse material, 20 to 80 percent of the particles are larger than 2 mm and the remainder are less than 2 mm).

By their type of movement, landslides are classified into five types: falls, topples, slides, spreads and flows. VARNES has introduced a last type: complex landslides which are a combination of two or more of the main movement types. (See Figure 1.1)

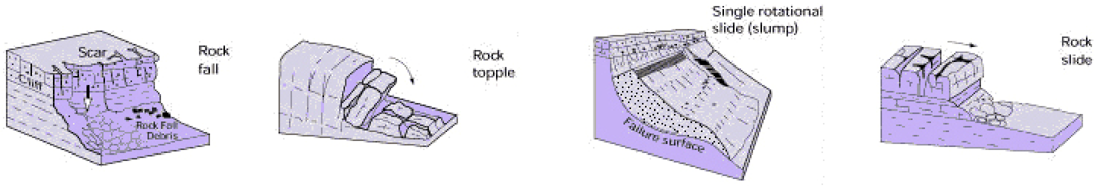

a. Rock fall b. Rock topple c. i. Rock slide (Rotational) c. ii. Rock slide (Translational)

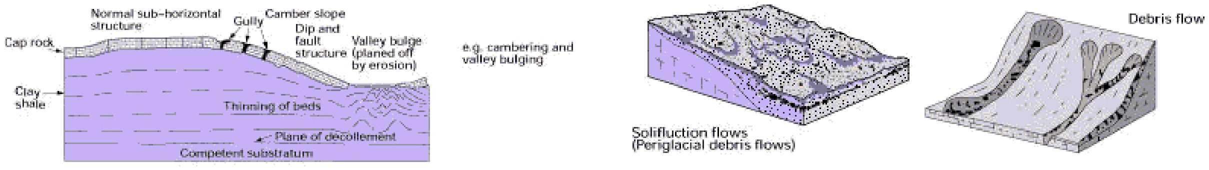

d. Spreads e. Debris flows

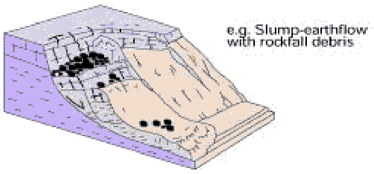

f. Complex slides

Figure 1.1 Classification of landslide types (VARNES, 1978)

These categories are described in detail as follows:

- *Falling:* Detachment of a mass from a steep sloppy cliff, which has little or no movement in tangential direction. Generally, after the detachment, the material falls in a free falling, rolling and/or bouncing manner.
- *Toppling:* Rotation of the material around an axis horizontal and parallel to the slope surface. This type of movement is generally in rock falls observed.
- *Sliding:* Sliding is generally defined as the downslope movement of a soil or rock mass occurring dominantly on rupture surfaces with intense shear strain. Movement can either be rotational (Figure 1.1.c.i) or translational (Figure 1.1.c.ii)
- *Spreading:* Fracturing and lateral extension of coherent rock or soil materials due to liquefaction or plastic flow of subjacent material (GEONET, 2007)

- *Flowing:* Sequential sliding movement, which advances by viscous flow in saturated materials.
- *Complex slides:* Combination of two or more above mentioned types.

Naturally, it is hard to explain the complex movement behavior of soil or rock with these six categories. The necessity to explain the soil behavior in detail has forced the experts to divide the above mentioned categories into subdivisions.

Besides movement types it is also important to know the initial failure mechanisms of landslides.

1.1.1 Initial Failure Mechanisms

The classification given by VARNES (1978) explains in fact the landslide movement types, but it lacks the capability of distinguishing the initial failure mechanisms with the run out types (e.g. rock toppling is a typical example of initial failure movement, while debris flows express a run out movement)

A more detailed and up-to-date version of VARNES' classification explaining the initial failure mechanism of the rockslides has been introduced by POISEL & PREH (2004). Figure 1.2 and Figure 1.3 illustrate these initial failure mechanisms thoroughly.

This catalogue of initial failure mechanisms takes into account the geological setting and the geometry of the slope, the joint structure, the habitus of the rock blocks, as well as the mechanical behavior of the rocks and of the rock mass (deformation and strength parameters) (POISEL & PREH, 2004). As in the VARNES' case, many classifications of rock slope failure mechanisms do not distinguish the initial failure or detachment mechanism and the possible run out (e.g. rockfall, rock slide, rock avalanche). Through the catalogue of initial failure mechanisms given below, sophisticated diagnose and more suitable judgment of the rockslide initial failure mechanism could be done.

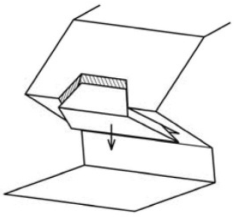	**Falling of rock blocks**	R.E. GOODMAN & G.-H. SHI Block Theory (1985)
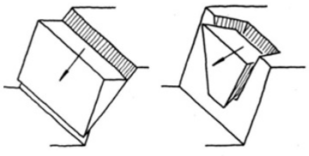	**Sliding of a rock block on a single or on two discontinuities** (translational sliding)	R.E. GOODMAN & G.-H. SHI Block Theory (1985)
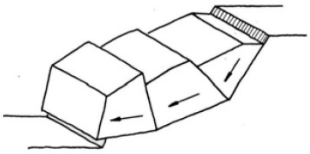	**Sliding of several rock blocks on a polygonal sliding plane**	P. GUSSMANN Kinematical Elements in Geomechanics. NUMOG (1988)
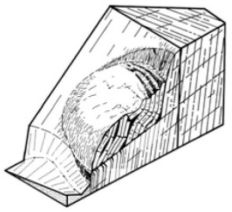	**Rock slumping** (backward rotation of rock blocks)	D.S. KIEFFER Ph.D Thesis University of California-Berkeley (1998)
	**Sliding of a fractional body on a shelly, newly formed sliding surface** (rotational sliding) (mainly in rock masses of low strength, e.g. heavily fractured rock; block dimensions << slope height)	A.W. BISHOP Geotechnique 5 (1955)
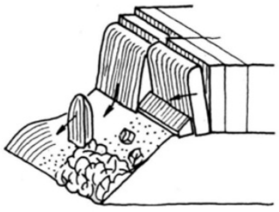	**Translational or rotational descent of tower– or slab-shaped blocks of competent rock upon an incompetent base** ("Hard on soft")	R. POISEL & W. EPPENSTEINER Proc. 5th Int.Symp. Landslides (1988)

Figure 1.2 Rock slope initial failure mechanisms and their mechanical models - Part 1 (POISEL & PREH, 2004)

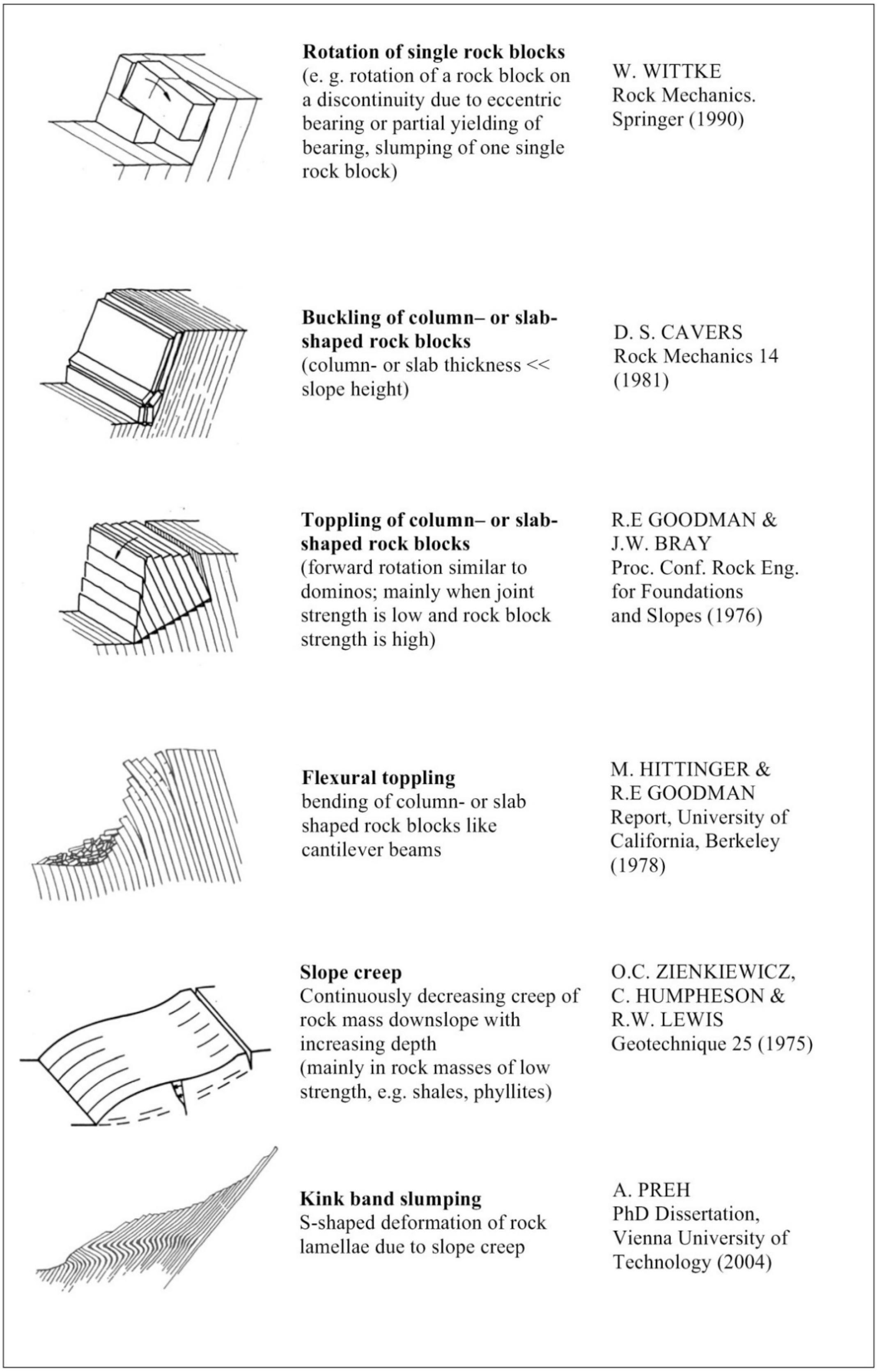

Rotation of single rock blocks (e. g. rotation of a rock block on a discontinuity due to eccentric bearing or partial yielding of bearing, slumping of one single rock block)	W. WITTKE Rock Mechanics. Springer (1990)
Buckling of column– or slab-shaped rock blocks (column- or slab thickness << slope height)	D. S. CAVERS Rock Mechanics 14 (1981)
Toppling of column– or slab-shaped rock blocks (forward rotation similar to dominos; mainly when joint strength is low and rock block strength is high)	R.E GOODMAN & J.W. BRAY Proc. Conf. Rock Eng. for Foundations and Slopes (1976)
Flexural toppling bending of column- or slab shaped rock blocks like cantilever beams	M. HITTINGER & R.E GOODMAN Report, University of California, Berkeley (1978)
Slope creep Continuously decreasing creep of rock mass downslope with increasing depth (mainly in rock masses of low strength, e.g. shales, phyllites)	O.C. ZIENKIEWICZ, C. HUMPHESON & R.W. LEWIS Geotechnique 25 (1975)
Kink band slumping S-shaped deformation of rock lamellae due to slope creep	A. PREH PhD Dissertation, Vienna University of Technology (2004)

Figure 1.3 Rock slope initial failure mechanisms and their mechanical models - Part 2 (POISEL & PREH, 2004)

1.2 Rock Mass Falls

A rock mass fall is often named as “Rock Avalanche”. The term “Rock Avalanche” has been first used by McCONNELL & BROCK (1904) to describe the “Frank Slide” in Alberta (Canada). It has been later described by CRANDELL (1968) in detail as follows: “very rapid downslope flowage of segments of bedrock that become shattered and pulverized during movement, which typically results from a very large rock fall or rockslide”.

In order to be consistent with the terminology worldwide while dealing with rock falls, it has been recommended by landslide experts to use a set of definitions. Figure 1.4 illustrates some important parts in a rockslide. The part that loose material (e.g. rock) detaches apart is called detachment area or *detached area*. The travel course that the detached material follows named as *run out path*, and the area, where the detached mass comes into a stabile position named as *deposit area*.

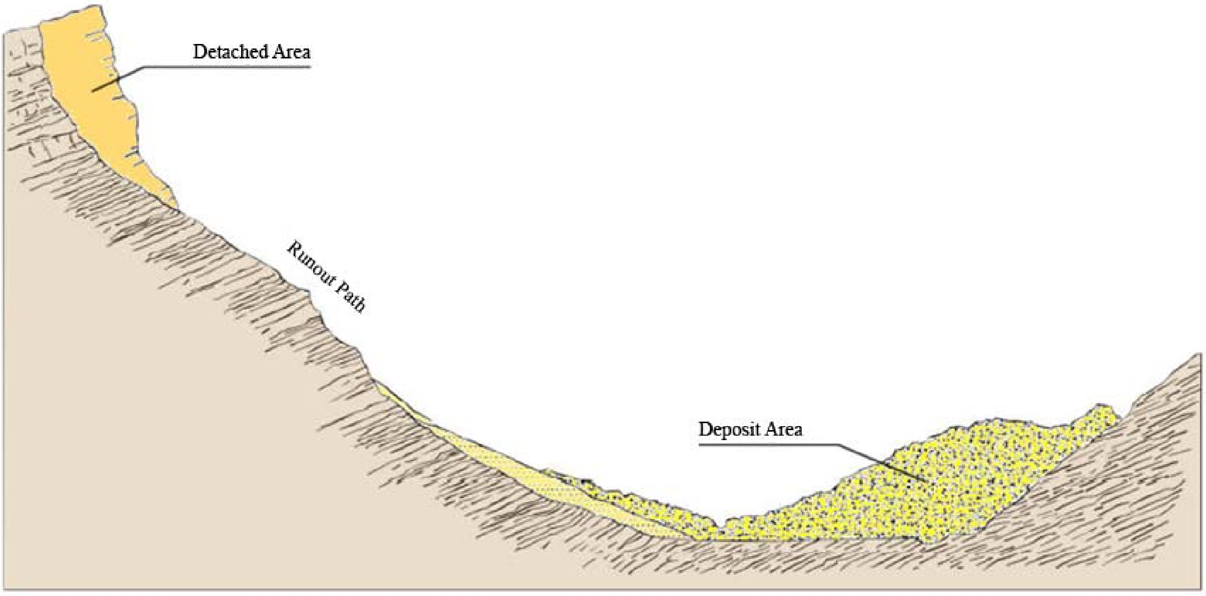

Figure 1.4 Denotation of different parts in a rockslide (HEIM, 1932)

The other important parameters to differentiate in defining a rockslide are slope (gradient) parameters, namely: geometric gradient (slope average angle) and Fahrböschung. The geometric gradient defined as the obtainable angle connecting the uppermost point of the detachment area from which the rock mass broke away and the farthest point of the detached loose material along the considered profile. On the other hand “Fahrböschung” (“travel angle”) is defined by HEIM (1932) as the slope of a line connecting the crest (uppermost part of the detached area) with the farthest point of the deposit area, measured on a straightened profile of the path (See Figure 1.5).

Figure 1.6 illustrates the energy line gradient of the detached rock mass.

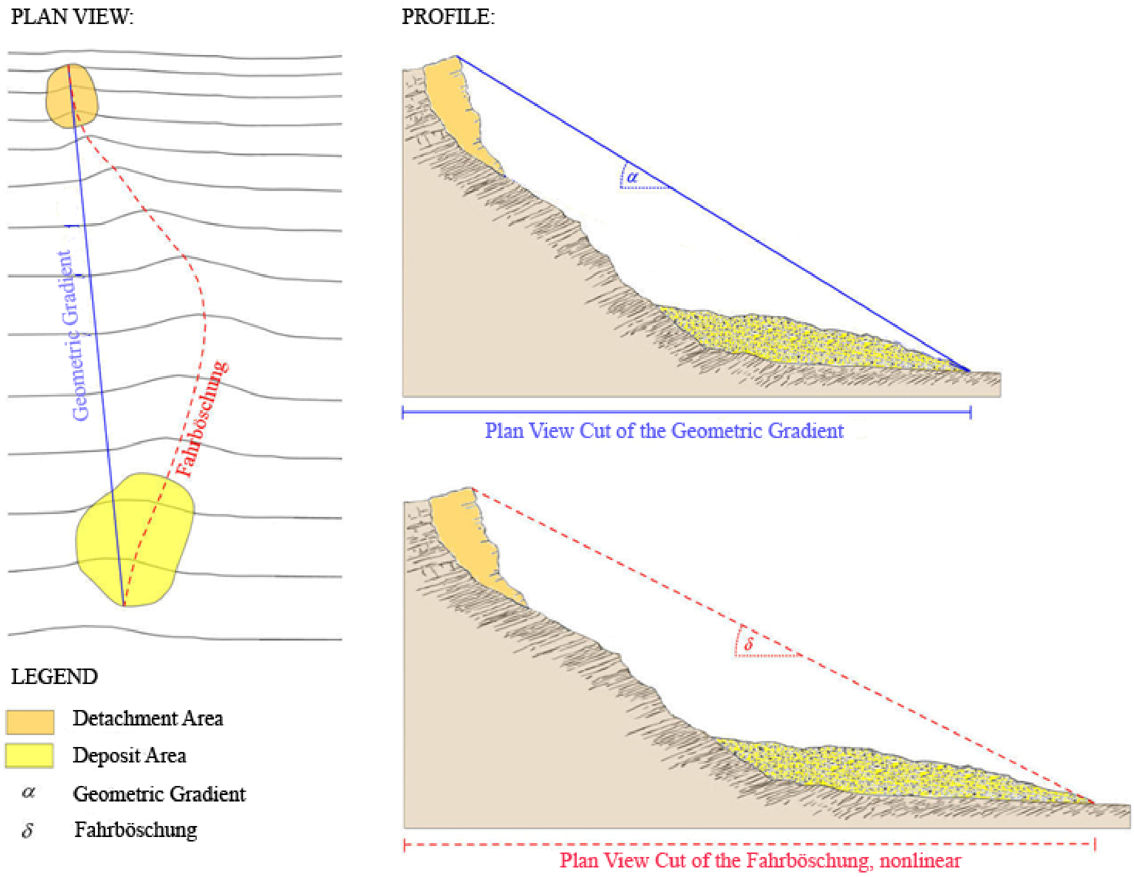

Figure 1.5 Geometric Gradient and Fahrböschung (HEIM, 1932)

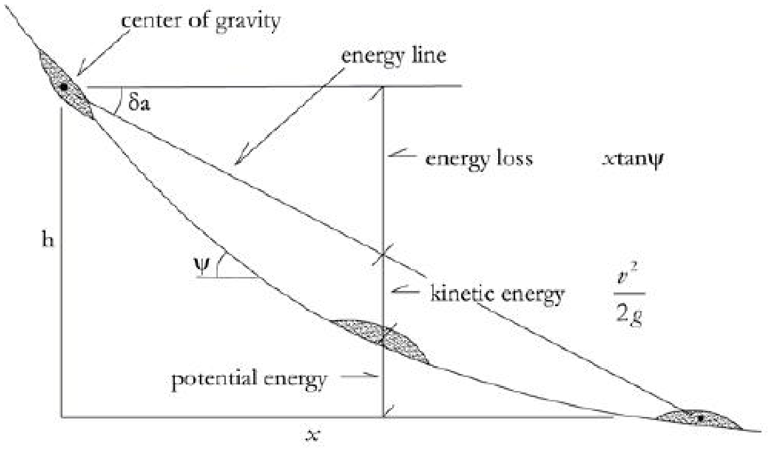

Figure 1.6 Gradient of energy line of the detached rock mass (SASSA, 1988)

1.2.1 Motion of Rock Masses on Slopes

Understanding and building a model of a rockslide necessitates constructing a mathematical model in which an actual rock block motion is explained. These motions are generalized into following individual movements:

- Free fall
- Bouncing
- Rolling
- Sliding

1.2.1.1 Free Fall

In free fall the main force acting on a rock block is gravitation and it has been observed that free fall occurs on slopes which are steeper than 90°, which means it can only happen in an overhang case.

For the calculation of the motion of a rock block in free fall the air resistance can be neglected, so that the velocity and the kinetic energy of the rock block can be calculated easily. It has been experimentally shown that air resistance has very small effect on a rock block, which could be neglected (BOZZOLO, 1987).

The velocity and the kinetic energy of the block can be written as follows:

$$v = \sqrt{2.g.h} \tag{1.1}$$

$$E_{kin} = \frac{1}{2}.m.v^2 \tag{1.2}$$

The formulas above include the following variables:

h… Fall height [m]

g… Gravitation constant [m/s^2]

m… Weight of the block [kg]

By impact great plastic deformations can occur and the block could loose its energy. The fall height indeed has great effect on the velocity and the kinetic energy of the block, but however it has rare implications on the motion process of the block. A bouncing motion follows generally the free fall action (BROILI, 1974).

1.2.1.2 Bouncing

Bouncing motion occurs when the air trajectory (parabola) intersects with the slope. Rock blocks have tendency to break upon their first contact with the slope. Regardless whether they crush or not, with the block size of 0.3 m^3 the energy loss is between 75% and 85%. Similar observations have been made with the block size of 1 to 10 m^3. The deciding factors by bouncing are block shape, slope geometry and ground conditions. It has been observed experimentally that the rock blocks which have bigger geometry tend to roll rather than bounce. It has been also observed that small blocks bounce further than the bigger ones and the bouncing movement is often followed by a rolling motion (BROILI, 1974).

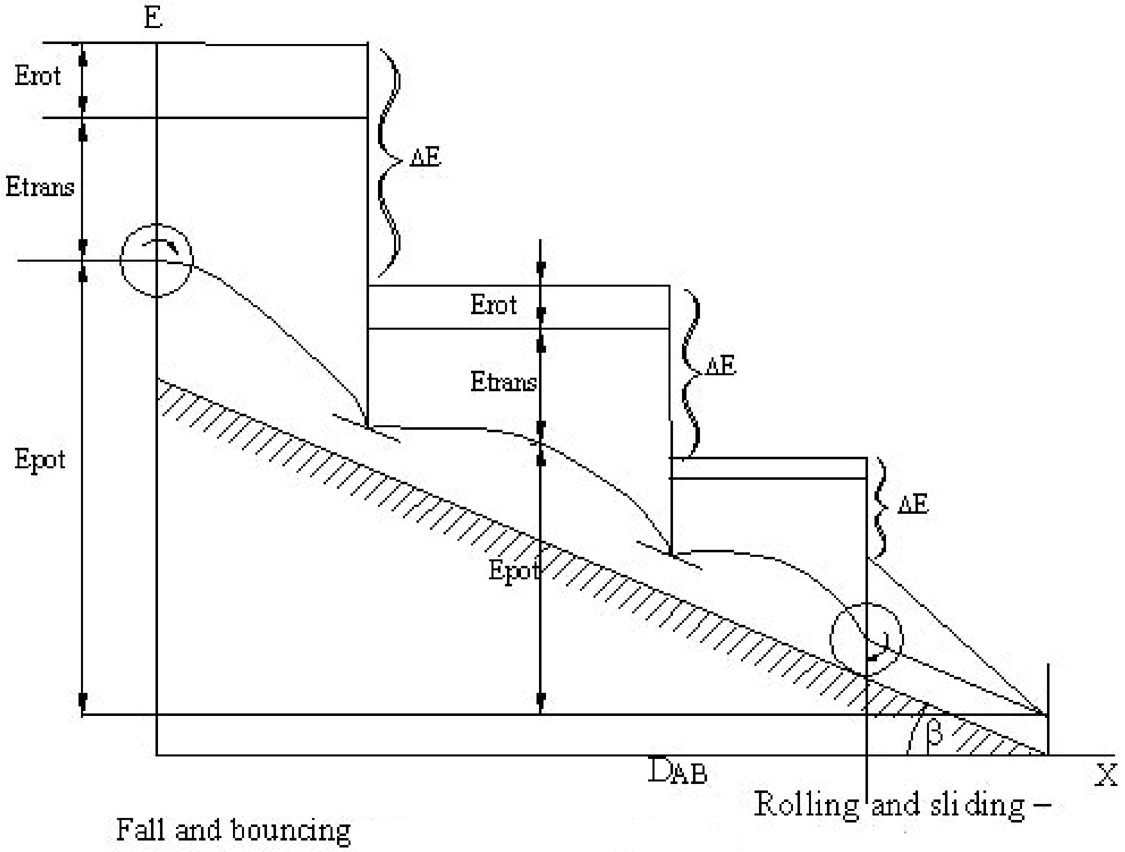

Figure 1.7 Bouncing and Fall Motion (GERBER, BÖLL, RICKLI, & GRAF, 1995)

Figure 1.7 illustrates the fall and bouncing motion including the potential and kinetic energy (rotational and translational kinetic energy) followed by rolling and/or sliding motion.

1.2.1.3 Rolling

Rolling is a motion where a rock block rotates around its axis without losing contact with the ground. Rolling is the prevailing way of motion with long trajectories on a moderate slope (EVANS & HUNGR, 1993).

The following four conditions define the way of this motion, if we take a close look at a single rolling block:

- The possibility of rolling depends to a high degree on the body shape. The ability to roll is asymptotically increased by the approximation of the round cross section with the centre of gravity (mass centre) in its geometric centre.
- Once the body starts rolling the motions continues even under the conditions that would not allow starting a rolling motion (unfavorable slope angle and coefficient of friction).
- Even with completely plane ground, non-circular rolling bodies start bouncing at a critical velocity.
- Beside body shape, the critical velocity depends on its size: for geometrically similar bodies, it is proportional to the square root of the linear dimensions. (PETJE, MIKOS, & MAJES, 2006)

To define the velocity of rolling, we must take a closer look at the energy equation:

$$E_{kin} = E_{trans} + E_{rot} = \frac{m.v^2}{2} + \frac{I.\omega^2}{2} \tag{1.3}$$

where *m* is the weight of the released particle [*kg*], *v* is the velocity [*m/s*], *I* is the moment of inertia and ω is the angular velocity [s^{-1}].

For a sphere, it is possible to rewrite the equation 2.3 as follows:

$$I = \frac{2}{5}.m.r^2;\ \omega = \frac{v}{r} \qquad (1.4;\ 1.5)$$

$$E_{kin} = E_{trans} + E_{rot} = \frac{1}{2}.m.v^2 + \frac{1}{5}.m.v^2 = \frac{7}{10}.m.v^2 \tag{1.6}$$

So we can deduce from equation 2.6 the fact that during the rolling motion of a particle 5/7 (71.4%) of kinetic energy belongs to translational energy and 2/7 (28.6%) to rotational energy. The total energy equation of a rolling block at point A (Figure 1.8) could be redefined as follows:

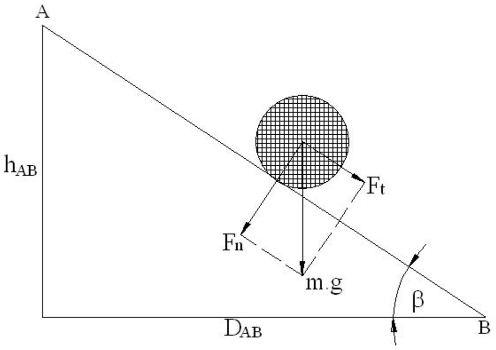

Figure 1.8 Rolling motion on a slope (PETJE, MIKOS, & MAJES, 2006)

$$E_A = E_{pot} + E_{kin} = m.g.h_{AB} + \frac{7}{10}.m.{v_A}^2$$

$$= m.g.\sin\beta\,.S_{AB} + \frac{7}{10}.m.{v_A}^2 \tag{1.7}$$

where *m* is the weight of the block, v_A is the velocity at point A, *β* is the slope angle and S_{AB} is the length of slope.

During the rolling motion both the sphere and the slope surface deform to form a resistance against rolling.

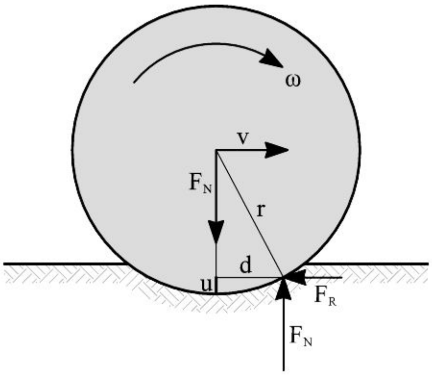

Figure 1.9 Illustration of the resistant forces during rolling motion (PREH A. , 2004)

As seen in Figure 1.9, the normal force (F_N) and the rolling resistance force (F_R) act on the point between the deformed surface of the slope and the sphere itself.

From equilibrium the rolling resistance could redefined as follows:

$$F_R = \frac{d}{r}.F_N = c_R.F_N \tag{1.8}$$

where c_R is the rolling resistance coefficient. This coefficient can be expressed in terms of sink depth *u* and radius *r* as follows:

$$c_R = \frac{\sqrt{u.(2r-u)}}{r} \tag{1.9}$$

At point B the energy equation changes into:

$$E_B = E_{kin} + E_{res} = \frac{7}{10}.m.{v_B}^2 + c_R.F_N.S_{AB}$$

$$= \frac{7}{10}.m.{v_B}^2 + c_R.m.g.\cos\beta\,.S_{AB} \tag{1.10}$$

where v_B is the velocity at point B.

From the conservation of energy law, the energies at point A and B should be the same, which gives:

$$v_B = \sqrt{{v_A}^2 + \frac{10}{7}.g.S_{AB}.(\sin\beta - c_R.\cos\beta)} \tag{1.11}$$

A constant velocity course occurs when the rolling resistance coefficient c_R equals the tangent of slope angle β. The inequality of $c_R < \tan\beta$ starts the rolling motion, where $c_R > \tan\beta$ ends it.

1.2.1.4 Sliding

Sliding is the motion where the block possesses only translational energy without the loss of contact with the slope plane. Sliding occurs only in initial or final phases of the motion. If the slope gradient increases, the sliding rock starts falling, rolling or bouncing (BOZZOLO, 1987).

As in Figure 1.8 the energies between points A and B should also be preserved. If the Coulomb's law of friction is inserted in this energy equilibrium, the velocity at point B could be achieved as follows:

$$v_B = \sqrt{{v_A}^2 + 2.g.S_{AB}.(\sin\beta - \mu.\cos\beta)} \tag{1.12}$$

where μ is the friction coefficient, which is the tangent of friction angle φ. Velocity changes with the relation of friction coefficient μ with the slope angle β as follows:

- $\mu = \beta$ than constant velocity ($v_A = v_B$)

- $\mu < \beta$ than sliding occurs
- $\mu > \beta$ than the block will be slowed down (brake)

It is possible to deduce that when two blocks having the same weight and velocity considered, if one starts to slide while the other performs pure rolling, than the rolling block possesses 5/7 of the kinetic energy of the sliding block.

1.2.1.5 Block Interaction

According to HEIM (1932), the movement procedure of cohesive rock masses, which have a volume larger than 500.000 m^3 and a fall height of few hundred meters, should be defined as stream like falls (Strömen). The stream like motion should not necessarily happen from the water-soil (rock) mixture like in debris flow, it could also happen in cohesive rock falls without the presence of water. Although the motion process is tried to be modeled with the help of continuum and fluid mechanics, the actual motion process remains unexplained.

2 Run out Models of Rock Slope Failures

At the moment an ideal model simulating both the initial failure mechanism of a rock slope and the run out does not exist. Thus rock slope failure models and run out models, based on the results of analyses of a particular rock slope failure have to be separated (POISEL & ROTH, 2004). An overview of run out models, which can be divided into empirical relations and into mechanical models, could be stated as follows:

1. Experiments in the field and physical models – experimental approach
2. Run out prediction methods – empirical approach
    - Single block
    - Rock avalanches
3. Run out prediction methods – mechanical models (analytical approach)
    - Lumped mass
    - Continuum mechanics
    - Kinetic theory
    - Discontinuum mechanics

2.1 Experimental Approach

Direct field observations of catastrophic motion of avalanches are extremely difficult to make; in fact there is only a limited number of field observations that would permit a partial verification of theoretical models. Laboratory experiments permit a control of both material properties and bed geometries, and thus facilitate a comparison of theory with experiment.

A satisfactory fit of a model computation with laboratory data still does not imply that the theory is adequate to describe large scale processes in nature. Apart from the idealizations of the laboratory experiment, scale effects might falsify the conclusions. However, finding satisfactory agreement between theory and experimental results in the small scale is still superior to none and it constitutes a step into the direction of treating the full problem (PIRULLI M. , 2005).

RITCHIE (1963) reported on extensive field experiments, testing the effectiveness of ditches and fences by using artificially triggered rockfalls. SPANG & SÖNSER (1995) gave results of small scale rockfall tests on artificial rock slopes when examining rail and tie walls.

BAGNOLD (1954) reported on experiments on a gravity-free dispersion of large solid spheres in a Newtonian fluid under shear, giving initial hints regarding the mechanisms of rock avalanches. HSÜ’s (1975) experiments on bentonite suspensions suggested that the flow of thixotrophic liquids is kinematically similar to the run out of rock slope failures (POISEL & ROTH, 2004).

Various experiments have been conducted through experts to understand the behavior of the mass movement during rockfalls, one of which for example experiments with about 10 m^3 of water-saturated sand and gravel were conducted at the U.S. Geological Survey debris flow flume (located in H.J. Andrews Experimental Forest, Oregon), a rectangular concrete chute 95 m long and 2 m wide that slopes 31° throughout most of its length and flattens at its base to adjoin an unconfined run out surface. Details are reported in IVERSON (1992), IVERSON (1997) and MAJOR & IVERSON (1999).

Figure 2.1 a. A debris flow discharging from the gate at the head of the flume. b. Debris flow passing instrumented cross section. (Images courtesy of U.S. Geological Survey)

2.2 Empirical Approach

2.2.1 Single Blocks

Empirical relations are, for example, rock fall tests in order to find areas of danger in a quarry. Based on extensive field experiments, RITCHIE (1963) gave design rules to find appropriate depths and widths of ditches related to slope geometry. Artificial rock falls carried out in situ by BROILLI (1974) showed that the movements are mainly influenced by the size of the rock blocks involved. The results of these in situ tests were used as a basis in the design of protection devices.

2.2.2 Rock Avalanches

The run out distance and the deposit area of a rock avalanche can be estimated by using statistical relations between the volume of a detached mass and the path profile of case studies, and also by using mass balance methods as carried out by HEIM (1932), SCHEIDEGGER (1973) and HSÜ (1975).

From empirical relations HEIM (1932) ascertained the dependence of the distance travelled by the rock mass upon the initial height, the regularity of terrain and the volume of the rockfall. He defined “Fahrböschung”, as already explained in chapter 1.2 (See Figure 1.5 and Figure 2.2)

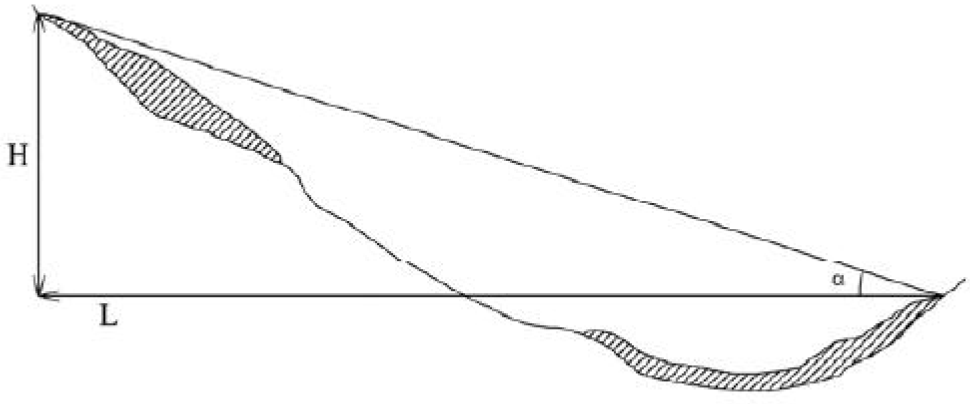

Figure 2.2 Profile of rock avalanche showing the definition of Fahrböschung (α) (HEIM, 1932)

SCHEIDEGGER (1973) formalized the HEIM’s relationship by defining a correlation between landslide volume and the ratio of the total fall height, H, to the total run out distance, L, based on data from 33 prehistoric and historic rock avalanches (See Figure 2.3)

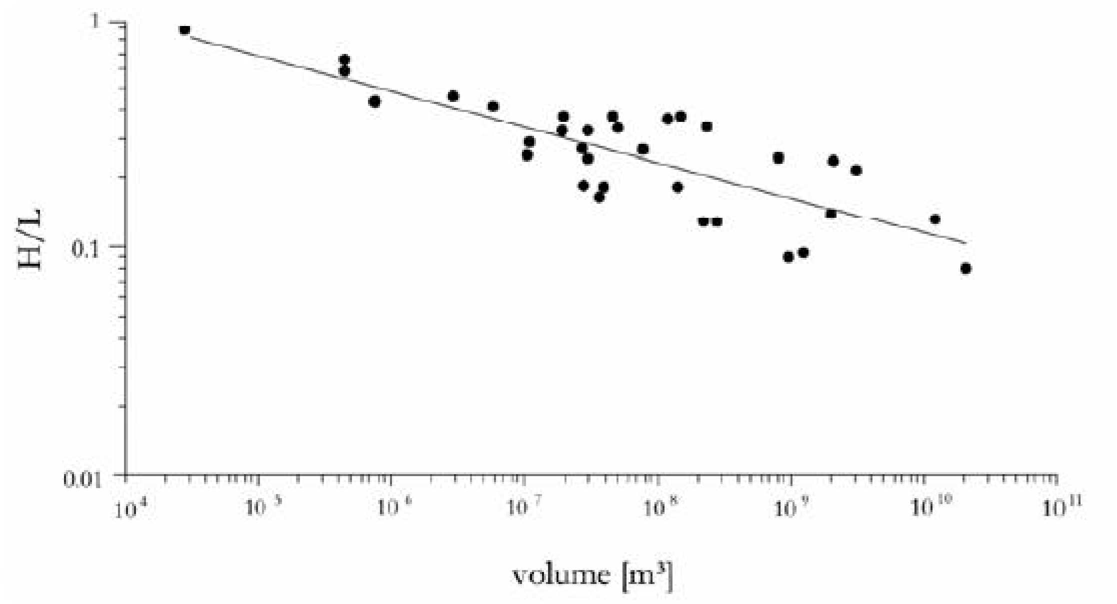

Figure 2.3 Correlation between rock avalanche volume and the tangent of the Fahrböschung angle (SCHEIDEGGER, 1973)

The empirical methods suffer from great scatter of data, making even the limited prediction very unreliable. It is difficult in this method to take account of the influences of the ground condition, the degree of saturation of the landslide mass, and the micro-topography (PIRULLI M. , 2005).

2.3 Analytical Approach

2.3.1 Lumped Mass

The lumped mass models idealize the motion of a slide block, by consequence they have an obvious limitation in being unable to account for internal deformation.

The block represents the mass of the potential slide. Friction between the block and plane prevents sliding below some critical angle of inclination; above the critical angle the mass accelerates according to Newton’s second law. Once the mass is in motion, deceleration occurs at angles of inclination below the critical angle. The energy line in Figure 1.6 illustrates the details in which the energy loss and the potential energy converted to kinetic energy are clearly expressed.

Even though the lumped mass models may provide reasonable approximations to the movement of the centre of gravity of the landslide, they are not able to provide information as to the spatial and temporal properties of an avalanche such as the velocity distribution and the evolution of the avalanche height and spread, aspects that are certainly not constant throughout the dimensions of the flowing mass and the time.

2.3.2 Continuum Mechanics

Continuum mechanics models for rapid landslides use techniques developed for analysis of the flow of fluids in open channels. There are, however, important differences between fluids and earth materials, even if the latter are saturated and highly disturbed. In addition, landslide paths are often much steeper and more varied than channels considered in most hydraulic calculations and landslide motion is highly unsteady. These characteristics make the analysis of the landslide motion exceedingly complex.

Although granular material is a large assemblage of discrete particles, it is here treated as a continuum. This implies that the depth and length of the flowing mass are large compared to the dimensions of a typical particle.

In this framework it becomes fundamental to find an “apparent” fluid whose rheological properties are such that the bulk behavior of the prototype landslide. The properties of the equivalent fluid do not correspond to those of any of the slide components.

Figure 2.4 a. Prototype of a heterogeneous and complex moving mass; b. A homogeneous "apparent fluid" replaces the slide mass (HUNGR, 1995)

A promising approach for describing unsteady and non-uniform flow on complex geometry is the depth averaged Saint Venant approach, in which the avalanche thickness (H) is very much smaller than its extent parallel to the bed (L), which is often the case for geographic flows. The material is assumed to be incompressible and the mass and the momentum equations are written in a depth averaged form.

Depth averaging allows us to avoid a complete three dimensional description of the flow: the complex rheology of the granular material is incorporated in a single term describing the frictional stress that develops at the interface between the flowing material and the rough surface (POULIQUEN & FORTERRE, 2002).

Depth averaged equations have been introduced in the context of granular flows by SAVAGE & HUTTER (1989). In their model, the moving mass is supposed to be volume preserving, is cohesionless and obeys a Mohr-Coulomb yield criterion both inside the deforming mass as well as at the sliding basal surface, but with different internal, φ, and bed, δ, friction angles.

Key elements of the work by SAVAGE & HUTTER (1989) included:

1. derivation and scaling of depth-averaged momentum and mass conversation equations to obtain one-dimensional shallow flow equations approximately normalized to account for the finite size of avalanching masses;
2. formulation of shallow flow equations using the Coulomb equation for basal shear resistance and an earth pressure equation for the influence of Coulomb friction on longitudinal normal stresses;
3. numerical solution of the one-dimensional shallow flow equations using a Lagrangian finite difference scheme suitable for tracking propagation and deformation of an avalanching mass; and
4. experimental testing that demonstrates the veracity of the model.

HUNGR (1995) presented a numerical model for rapid landslides, e.g. debris and rock avalanches, called DAN. The model is based on a Lagrangian solution of equations of motion and allows the selection of variety of material rheologies, which can vary along the slide path or within the slide mass. It also allows for the internal rigidity of relatively coherent slide debris moving on a thin liquefied basal layer. The data required for analyzing a landslide with DAN includes: material rheology (frictional, Bingham fluid), slope profile geometry, top profile of the initial mass and path width (provided e.g. by a rockfall program). The solution is explicit and occurs in timesteps. An assembly of mass and boundary blocks is set up to approximate the initial configuration of the slide mass. The new velocity of each boundary block at the end of a timestep is obtained from the old velocity by numerical integration of Newton´s second law. A second integration is used to obtain the displacements of the boundary blocks. The average depth of the flow in the mass blocks is determined so as to maintain their constant volume (PIRULLI M. , 2004).

2.3.3 Discontinuum Mechanics

Discontinuum mechanics modeling is based on the relatively new science of discontinua introduced in geomechanics almost forty years ago (GOODMAN, TAYLOR, & BREKKE, 1968). The run out mass is modeled as an assembly of particles moving down a surface. Its structure is often called a “fabric” referring to the microstructure of the particle mass collection, space between particles within the mass (pore space), arrangement of particles, and their static and dynamic motion interaction contact laws (MITCHELL, 1976).

Loose soils, concrete, and rock with fracture planes are all examples of discrete grain structures forming a discontinuum fabric formation.

The Discrete (Distinct) Element Method (DEM) is the term given to the numerical analysis procedure that simulates the behavior within the discontinuum mechanics. Formulation of discontinua by DEM was originally developed by CUNDALL (1971). (See for details Chapter 3.1).

Circular disks and spherical particles are most frequently studied due to the simplified particle contact detection mathematical algorithms and available computer power.

Much research has been published on the limitations of circular disks and spherical shaped particles. Most soils and fragmented rock particles are more angular and blocky which:

- increases voids within the fabric of granular mass,
- increases interlocking between particles, and
- inhibits rolling

Disks and spheres, unlike fragmented particles, produce a low shear resistance and induce rolling that dominates deformation of fabric (See Figure 4.1). Therefore, an adjustment should be undertaken.

WILL & KONIETZKY (1998) used the Particle Flow Code (PFC^{2D}) by ITASCA to analyze rock fall and rock avalanche problems.

ROTH (2003) adapted the contact management in PFC^{3D} in simulating rock avalanches in three dimensions (See Figure 2.5). The adjustment procedure is explained thoroughly in chapter 4.

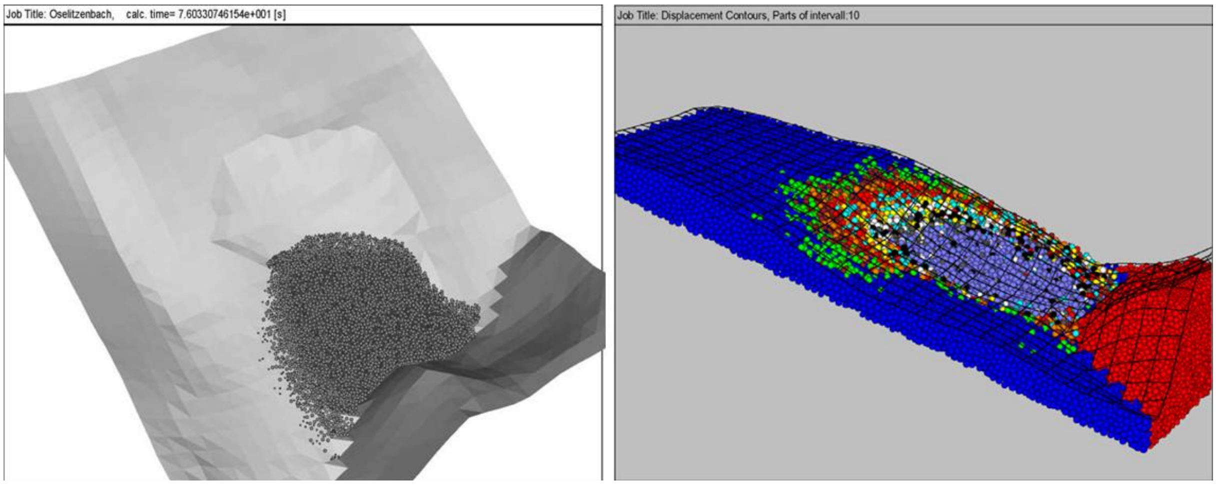

Figure 2.5 Example of PFC applications. a. Ball-Wall model (ROTH, 2003) b. All-Ball model (PREH A. , 2004)

The participants in the benchmarking exercise, which was held at the 2007 International Forum on Landslide Disaster Management, proposed several rock slide simulation cases carried through various run out programs. The Table 2.1 and 2.2 illustrate the participants and their simulation programs, under which only the PFC program works with the discontinuum mechanics idea; the other computer programs have the continuum mechanics background.

Table 2.1 The participants and their simulation programs (LANDSLIDE FORUM, 2007)

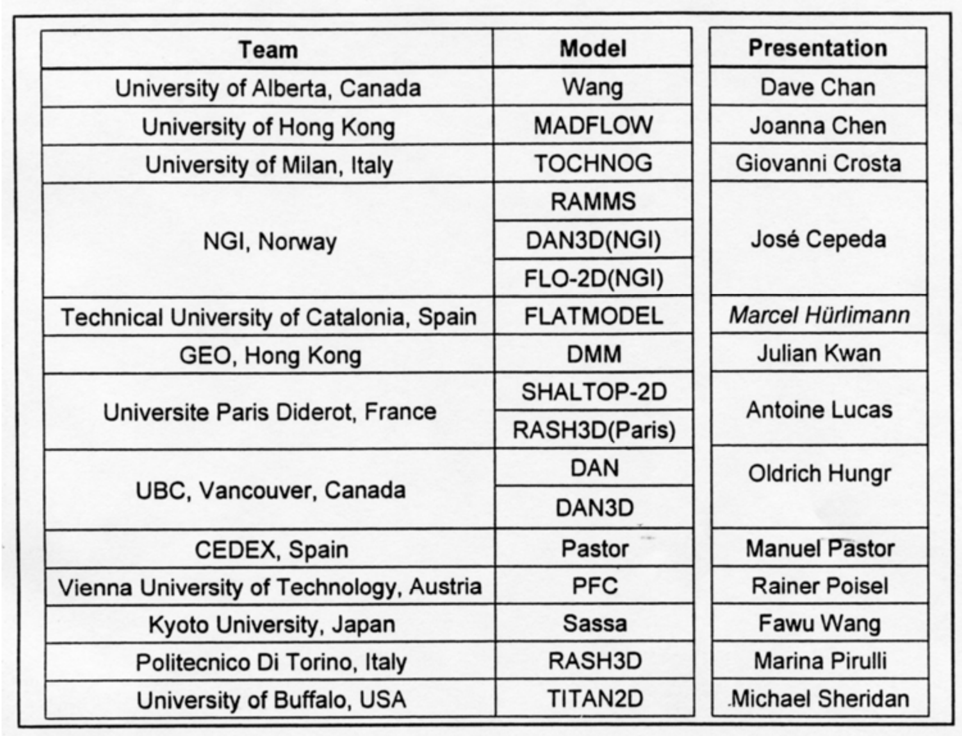

Team	Model	Presentation
University of Alberta, Canada	Wang	Dave Chan
University of Hong Kong	MADFLOW	Joanna Chen
University of Milan, Italy	TOCHNOG	Giovanni Crosta
NGI, Norway	RAMMS	José Cepeda
	DAN3D(NGI)	
	FLO-2D(NGI)	
Technical University of Catalonia, Spain	FLATMODEL	*Marcel Hürlimann*
GEO, Hong Kong	DMM	Julian Kwan
Universite Paris Diderot, France	SHALTOP-2D	Antoine Lucas
	RASH3D(Paris)	
UBC, Vancouver, Canada	DAN	Oldrich Hungr
	DAN3D	
CEDEX, Spain	Pastor	Manuel Pastor
Vienna University of Technology, Austria	PFC	Rainer Poisel
Kyoto University, Japan	Sassa	Fawu Wang
Politecnico Di Torino, Italy	RASH3D	Marina Pirulli
University of Buffalo, USA	TITAN2D	Michael Sheridan

Table 2.2 The matrix of the participant groups and their selected rock slide cases (LANDSLIDE FORUM, 2007)

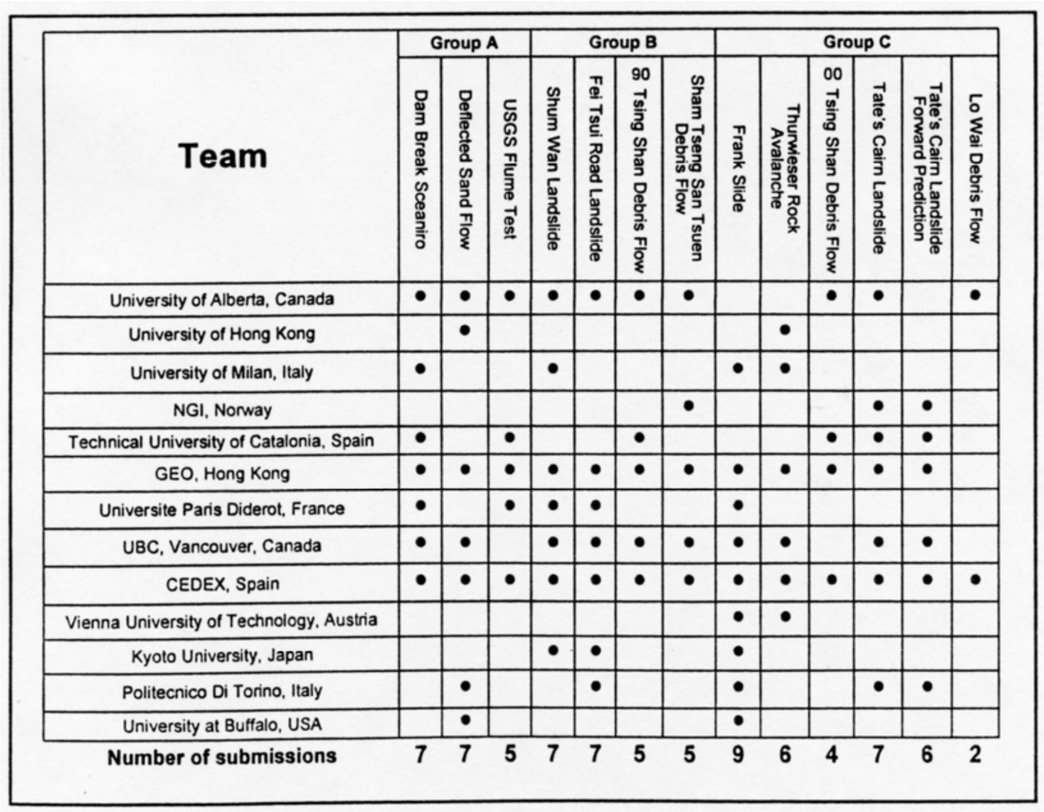

Team	**Group A**			**Group B**				**Group C**					
	Dam Break Sceaniro	**Deflected Sand Flow**	**USGS Flume Test**	**Shum Wan Landslide**	**Fei Tsui Road Landslide**	**90 Tsing Shan Debris Flow**	**Sham Tseng San Tsuen Debris Flow**	**Frank Slide**	**Thurwieser Rock Avalanche**	**00 Tsing Shan Debris Flow**	**Tate's Cairn Landslide**	**Tate's Cairn Landslide Forward Prediction**	**Lo Wai Debris Flow**
University of Alberta, Canada	●	●	●	●	●	●	●			●	●		●
University of Hong Kong		●							●				
University of Milan, Italy	●			●				●	●				
NGI, Norway							●				●	●	
Technical University of Catalonia, Spain	●		●			●				●	●	●	
GEO, Hong Kong	●	●	●	●	●	●	●	●	●	●	●	●	
Universite Paris Diderot, France	●		●	●	●			●					
UBC, Vancouver, Canada	●	●		●	●	●	●	●	●		●	●	
CEDEX, Spain	●	●	●	●	●	●	●	●	●	●	●	●	●
Vienna University of Technology, Austria								●	●				
Kyoto University, Japan				●	●			●					
Politecnico Di Torino, Italy		●			●			●			●	●	
University at Buffalo, USA		●						●					
Number of submissions	**7**	**7**	**5**	**7**	**7**	**5**	**5**	**9**	**6**	**4**	**7**	**6**	**2**

3 Particle Flow Code in 3 Dimensions (*PFC*^{3D})

The Particle Flow Code is a methodology to analyze complex systems with the help of numerical modeling on the basis of distinct element methods (DEM) (HART, 1996). With the Particle Flow Code, it is possible to calculate models both in two and three dimensions. The basics of the Particle Flow Code is detailed through PREH (2004) and ITASCA (2006), where in this work only three dimensions (*PFC*^{3D}) will be taken into account.

A rockslide which is modeled with *PFC*^{3D} has two components, namely, rigid, finite (or infinite – optional) two dimensional wall elements, and spherical particles. These sphere shaped particles can be arranged in any order or can be combined to form a large volume particle. The contacts between each particle and particles with walls detected automatically at each step of the calculation and the contacts that have been formed due to the movement of each particle are also taken into account during the steps. Also the calculation algorithm provides every possible movement each particle can make as a result of kinematic conditions, during which every possible physical condition can be removed or redefined at any step. The particles can be bonded through their contact points and these bonds can be destructed through a possible hit or impact. A very fundamental and essential advantage of this program is that all processes can be modeled and analyzed at both macro and micro levels. The clear developed and formulated calculation cycle of *PFC* helps to handle large and complex cases within personal computer competency. The geometric simplicity also assists the program to construct and calculate nonlinear situations und physical instabilities in a tolerable time scale (PREH A. , 2004).

PFC provides a particle-flow model containing the following assumptions:

1. The particles are treated as rigid bodies.
2. The contacts occur over a vanishingly small area (i.e., at a point).
3. Behavior at the contacts uses a soft-contact approach whereas the rigid particles are allowed to overlap one another at contact points.
4. The magnitude of the overlap is related to the contact force via the force displacement law, and all overlaps are small in relation to particle sizes.
5. Bonding can be introduced at particle contacts.
6. All particles are spherical. However new geometric complex elements can be created by combining spherical particles and wall elements to form new shapes. (ITASCA, User's Manual, PFC 3D, 2006)

3.1 Distinct-Element Method

The distinct-element method (DEM) was first introduced by CUNDALL (1971) for the analysis of rock mechanic problems. CUNDALL and HART (1992) have proposed that distinct-element method should be based on algorithms allowing finite displacement and rotation of discrete bodies, including complete detachment, and it recognizes new contacts automatically as the calculation processes. *PFC* can be viewed as a simplified implementation of DEM because of the restriction to rigid spherical bodies.

Essential characteristics of DEM:

- Discrete elements should be geometrically approximated to form a definite object. Sphere shape approximation can be enough to maintain a pass trough continuums mechanics to particle oriented mechanics. Material behavior could be taken either rigid or deformable, but if a motion at contact points occurs, rigid body assumption is suitable, however, if an intense deformation at the contact points is expected, than the deformation of the elements should be provided.
- To provide a block interaction, the contact character should be well formulated. Depending on the geometry of the blocks the type of contacts and block interaction differ (point, line or plane contact). The contact points and forces are taken into account with appropriate contact model (e.g. elastic force-displacement law, Coulomb friction law or viscose damping).
- A capable algorithm should be existent to determine whether the blocks are in contact or not. Newton's second law is used to determine the motion of each particle arising from the contact and body forces acting upon it, while the force-displacement law is used to update the contact forces arising from the relative motion at each contact.

To minimize the calculation time and to increase the number of analyzed particles in *PFC*, several modifications in DEM have been made. These modifications are explained in assumptions of *PFC*.

3.2 Calculation Cycle

The calculation cycle in *PFC* is a timestepping algorithm that requires the repeated application of the law of motion to each particle, a force-displacement law to each contact, and a constant updating of wall positions. Contacts, which may exist between two balls, or between a ball and a wall, are formed and broken automatically during the course of a simulation. The calculation cycle is illustrated in Figure 3.1.

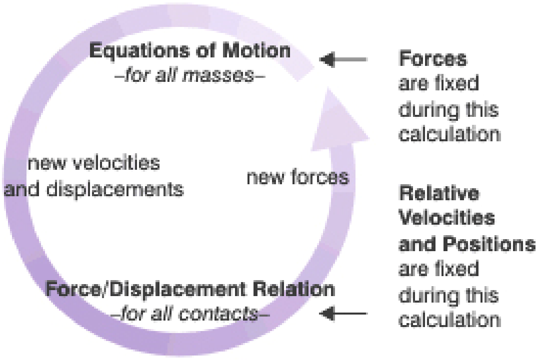

Figure 3.1 PFC calculation cycle (ITASCA, 2007)

At the start of each timestep, the set of contacts is updated from the known particle and wall positions. The force-displacement law is then applied to each contact to update the contact forces based on the relative motion between the two entities at the contact and the contact constitutive model. Next, the law of motion is applied to each particle to update its velocity and position based on the resultant force and moment arising from the contact forces and any body forces acting on the particle. Also, the wall positions are updated based on the specified wall velocities (ITASCA, 2006).

3.3 Force-Displacement Law

The force-displacement law relates the relative displacement between two entities at their contact point. For both ball-ball and ball-wall contacts, this force arises from the touch point of the entities.

The force-displacement law operates at the touch points and can be described in terms of a contact point, $x_i^{[C]}$, lying on a contact plane that is defined by a unit normal vector, n_i. The contact point is within the interpenetration volume of the two entities. For ball-ball interaction, the normal vector is directed along the line between ball centers; for ball-wall contact, the normal vector is directed along the line defining the shortest distance between the ball center and the wall. The contact force is decomposed into a normal component acting in the direction of the normal vector, and a shear component acting in the contact plane. The force-displacement law relates these two components of force to the corresponding components of the relative displacement via the normal and shear stiffnesses at the contact.

The force-displacement law is described for both ball-ball and ball-wall contacts. For ball-ball contact, the relevant equations are presented for the case of two spherical particles, labeled A and B in Figure 3.2. For ball-wall contact, the relevant equations are presented for the case of a spherical particle and a wall, labeled **b** and **w**, respectively, in Figure 3.3. In both cases, U^n denotes overlap.

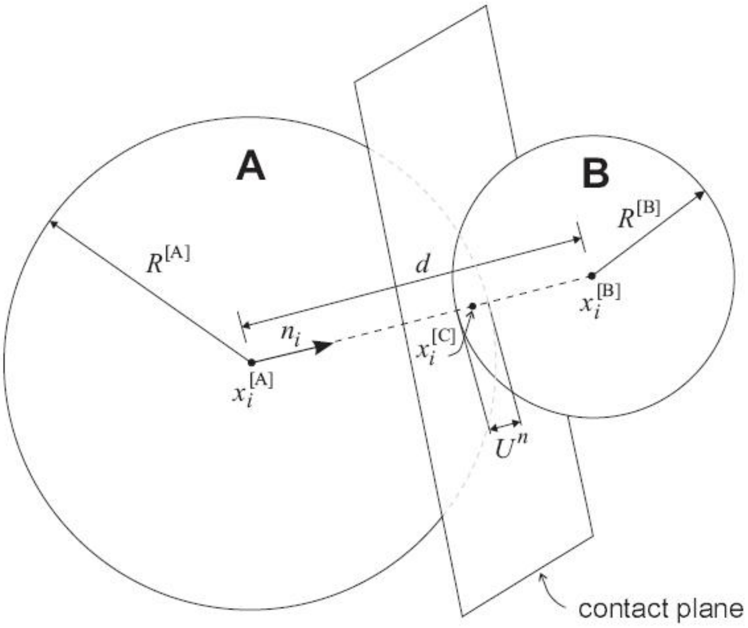

Figure 3.2 Illustration of ball-ball contact (ITASCA, 2006)

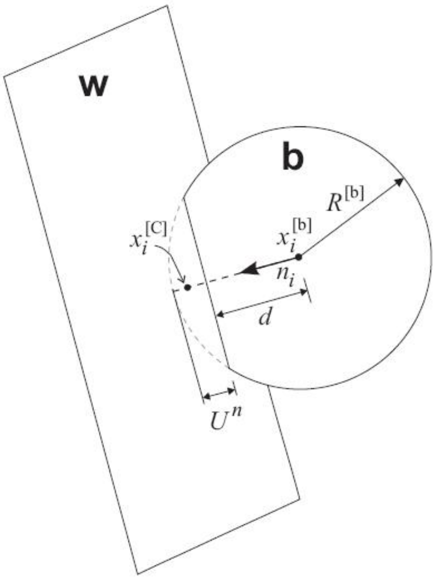

Figure 3.3 Illustration of ball-wall contact (ITASCA, 2006)

For ball-ball contact, the unit normal, n_i, that defines the contact plane is given by:

$$n_i = \frac{x_i^{[B]} - x_i^{[A]}}{d} \quad \text{(ball-ball)} \tag{3.1}$$

Where $x_i^{[A]}$ and $x_i^{[B]}$ are the position vectors of the centers of the balls A and B respectively, and d is the distance between the ball centers:

$$d = \left|x_i^{[B]} - x_i^{[A]}\right| = \sqrt{(x_i^{[B]} - x_i^{[A]}).(x_i^{[B]} - x_i^{[A]})} \quad \text{(ball-ball)} \tag{3.2}$$

For ball-wall contact, n_i is directed along the line defining the shortest distance, d, between the ball center and the wall. This direction is found by mapping the ball center into a relevant portion of space defined by the wall. This idea is illustrated in Figure 3.4 for a two-dimensional wall composed of line segments, $\overline{AB}$ and $\overline{BC}$. All space on the active of this wall can be composed into five regions by extending a line normal to each wall segment at its endpoints. If the ball center lies in regions 2 or 4, it will contact the wall along its length, and n_i will be normal to the corresponding wall segment. However, if the ball center lies in regions 1, 3, or 5, it will contact the wall at one of its endpoints, and n_i will lie along the line joining the endpoint and the ball center.

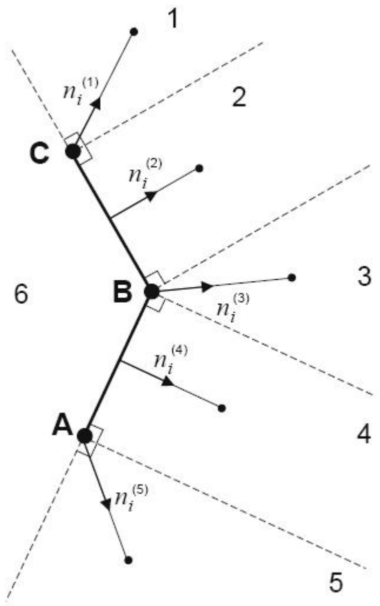

Figure 3.4 Determination of normal direction for ball-wall contact (ITASCA, 2006)

The overlap U^n, defined to be relative contact displacement in the normal direction, is given by

$$U^n = \begin{cases} R^{[A]} + R^{[B]} - d, & \text{(ball-ball)} \\ R^{[b]} - d, & \text{(ball-wall)} \end{cases} \tag{3.3}$$

where $R^{[\Phi]}$ is the radius of ball Φ.

The location of the contact point is given by

$$x_i^{[C]} = \begin{cases} x_i^{[A]} + \left(R^{[A]} - \frac{1}{2}U^n\right) n_i, & \text{(ball-ball)} \\ x_i^{[b]} + \left(R^{[b]} - \frac{1}{2}U^n\right) n_i, & \text{(ball-wall)} \end{cases} \tag{3.4}$$

The contact force vector F_i (which represents the action of ball A on ball B for ball-ball contact, and represents the action of the ball on the wall for ball-wall contact) can be resolved into normal and shear components with respect to the contact plane as

$$F_i = F_i^{\,n} + F_i^{\,s} \tag{3.5}$$

where $F_i^{\,n}$ and $F_i^{\,s}$ denote the normal and shear component vector, respectively.

The normal contact force vector is calculated by

$$F_i^{\,n} = K^n U^n n_i \tag{3.6}$$

where K^n is the normal stiffness [force/displacement] at the contact.

Note that the normal stiffness, K^n, is a secant modulus in that it relates total displacement and force. The shear stiffness, k^s, on the other hand, is a tangent modulus in that it relates incremental displacement and force. Motion of the contact is accounted for by updating n_i and $x_i^{[C]}$ every timestep.

The relative motion at the contact, or the contact velocity Vi (which is defined as the velocity of ball B relative to ball A at the contact point for ball-ball contact, and the velocity of the wall relative to the ball at the contact point for ball-wall contact), is given by

$$\begin{aligned} V_i &= \left(\dot{x}_i^{[C]}\right)_{\Phi^2} - \left(\dot{x}_i^{[C]}\right)_{\Phi^1} \\ &= \left(\dot{x}_i^{[\Phi^2]} + e_{ijk}\omega_j^{[\Phi^2]}\left(x_k^{[C]} - x_k^{[\Phi^2]}\right)\right) - \left(\dot{x}_i^{[\Phi^1]} + e_{ijk}\omega_j^{[\Phi^1]}\left(x_k^{[C]} - x_k^{[\Phi^1]}\right)\right) \end{aligned} \tag{3.7}$$

where $\dot{x}_i^{[\Phi j]}$ and $\omega_i^{[w]}$ are the translational and rotational velocities of entity Φ^j, where the following formula denotes it:

$$\{\Phi^1, \Phi^2\} = \begin{cases} \{A, B\} & \text{(ball-ball)} \\ \{b, w\} & \text{(ball-wall)} \end{cases} \tag{3.8}$$

The contact velocity can be resolved into normal and shear components with respect to the contact plane. Denoting these components by V_i^n and V_i^s for the normal and shear component, respectively, the shear component of the contact velocity can be written as

$$\begin{aligned} V_i^s &= V_i - V_i^n \\ &= V_i - V_j n_j n_i \end{aligned} \tag{3.9}$$

The shear component of the contact displacement-increment vector, occurring over a timestep of Δt, is calculated by

$$\Delta U_i^S = V_i^S \Delta t \tag{3.10}$$

and is used to calculate the shear elastic force-increment vector

$$\Delta F_i^S = -k^S \Delta U_i^S \tag{3.11}$$

where k^s is the shear stiffness at the contact. The new shear contact force is found by summing the old shear force vector existing at the start of the timestep (after it has been rotated to account for the motion of the contact plane) with the shear elastic force-increment vector

$$F_i^S = \{F_i^S\}_{rot.2} + \Delta F_i^S \tag{3.12}$$

The values of normal and shear contact force determined by Eqs. (3.6) and (3.12) are adjusted to satisfy the contact constitutive relations. After this adjustment, the contribution of the final contact force to the resultant force and moment on the two entities in contact is given by

$$\begin{aligned} F_i^{[\Phi^1]} &\leftarrow F_i^{[\Phi^1]} - F_i \\ F_i^{[\Phi^2]} &\leftarrow F_i^{[\Phi^2]} - F_i \\ M_i^{[\Phi^1]} &\leftarrow M_i^{[\Phi^1]} - e_{ijk} \cdot \left(x_j^{[C]} - x_j^{[\Phi^1]}\right) \cdot F_k \\ M_i^{[\Phi^2]} &\leftarrow M_i^{[\Phi^2]} - e_{ijk} \cdot \left(x_j^{[C]} - x_j^{[\Phi^2]}\right) \cdot F_k \end{aligned} \tag{3.13}$$

where $F_i^{[\Phi^j]}$ and $M_i^{[\Phi^j]}$ are the force and moment sums for entity Φ^j from Equ. (3.8)

3.4 Contact Constitutive Models

The overall constitutive behavior of a material is simulated in *PFC^{3D}* by associating a simple constitutive model with each contact. The constitutive model acting at a particular contact consists of three parts:

- Stiffness model: The stiffness model provides an elastic relation between the contact force and relative displacement
- Slip model: The slip model enforces a relation between shear and normal contact forces such that the two contacting balls may slip relative to one another.
- Bonding model: The bonding model serves to limit the total normal and shear forces that the contact can carry by enforcing bond-strength limits.

It is possible to modify these models by the implemented program language *FISH*.

3.4.1 Contact-Stiffness Models

The contact stiffnesses relate the contact forces and relative displacements in the normal and shear directions via Equ (3.6) and (3.11).

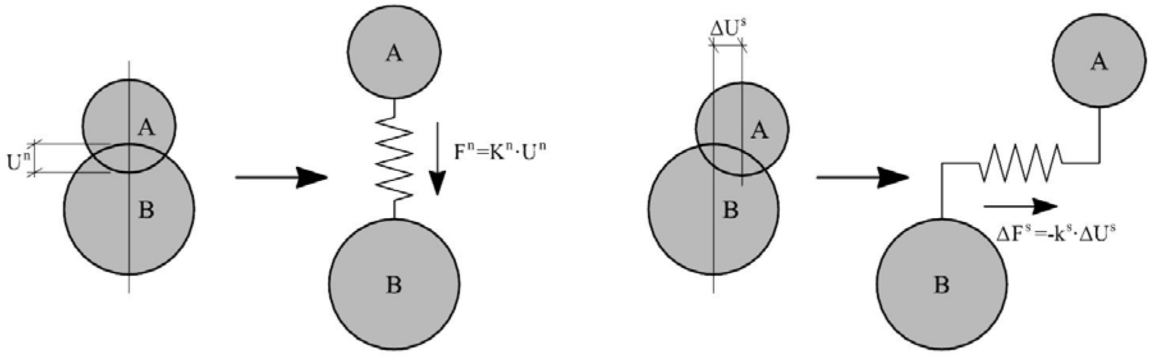

Figure 3.5 Illustration of Contact-Stiffness Model (HAINBÜCHER, 2001)

PFC^{3D} provides two contact-stiffness models: a linear model and a simplified Hertz-Mindlin model. Contact between a ball with the linear model and a ball with the Hertz model is not allowed, since the behavior is undefined.

3.4.1.1 The Linear Contact Model

The linear contact model is defined by the normal and shear stiffness k_n and k_s [force/displacement] of the two contacting entities (ball-to-ball or ball-to-wall). The contact stiffness for the linear contact model are computed assuming that the stiffness of the two contacting entities act in series. The contact normal secant stiffness is given by

$$K^n = \frac{k_n^{[A]} k_n^{[B]}}{k_n^{[A]} + k_n^{[B]}} \tag{3.14}$$

and the contact shear tangent stiffness is given by

$$k^S = \frac{k_S^{[A]} k_S^{[B]}}{k_S^{[A]} + k_S^{[B]}} \tag{3.15}$$

where the superscripts [A] and [B] denote the two entities in contact.

3.4.1.2 The Hertz-Mindlin Contact Model

The Hertz-Mindlin contact model is a nonlinear contact formulation based on an approximation of the theory of MINDLIN & DERESIEWICZ (1953). It is strictly applicable *only* to the case of spheres in contact, and does not reproduce the continuous nonlinearity in shear (rather, the initial shear modulus is used, but it depends on normal force).

The model is defined by the following two parameters: shear modulus *G* [stress] and Poisson’s ratio *v* [dimensionless] of the two contacting balls.

This model is not necessarily in detail explained, just because in this work only linear contact model has been used.

3.4.2 The Slip Model

The slip model is an intrinsic property of the two entities (ball-ball or ball-wall) in contact. It provides no normal strength in tension and allows slip to occur by limiting the shear force. This model is always active, unless a contact bond is present – in which case, the contact bond model behavior supersedes the slip model behavior.

The slip model is defined by the friction coefficient at the contact μ [dimensionless], where μ is taken to be the minimum friction coefficient of the two contacting entities. The criterion of no-normal strength is enforced by checking whether the overlap is less than or equal to zero. The contact is checked for slip conditions by calculating the maximum allowable shear contact force

$$F_{max}^S = \mu |F_i^n| \tag{3.16}$$

If $\left|F_i^S\right| > F_{max}^S$, then slip is allowed to occur (during the next calculation cycle) by setting the magnitude of F_i^S equal to F_{max}^S via

$$F_i^S \leftarrow F_i^S\left(\frac{F_{max}^S}{\left|F_i^S\right|}\right) \tag{3.17}$$

3.4.3 Bonding Models

PFC^{3D} allows particles to be bonded together at contacts. Two bonding models are supported: a contact-bond model and a parallel-bond model. Both bonds can be envisioned as a kind of glue joining the two particles. The contact-bond glue is of a vanishingly small size that acts only at the contact point, while the parallel-bond glue is of a finite size that acts over a circular cross-section lying between the particles. The contact bond can only transmit a force, while the parallel bond can transmit both a force and a moment.

Both types of bonds may be active at the same time; however, the presence of a contact bond inactivates the slip model. Once a bond is formed at a contact between two particles contact continues to exist until the bond is broken. Only particles may be bonded to one another; a particle may not be bonded to a wall.

3.4.3.1 The Contact-Bond Model

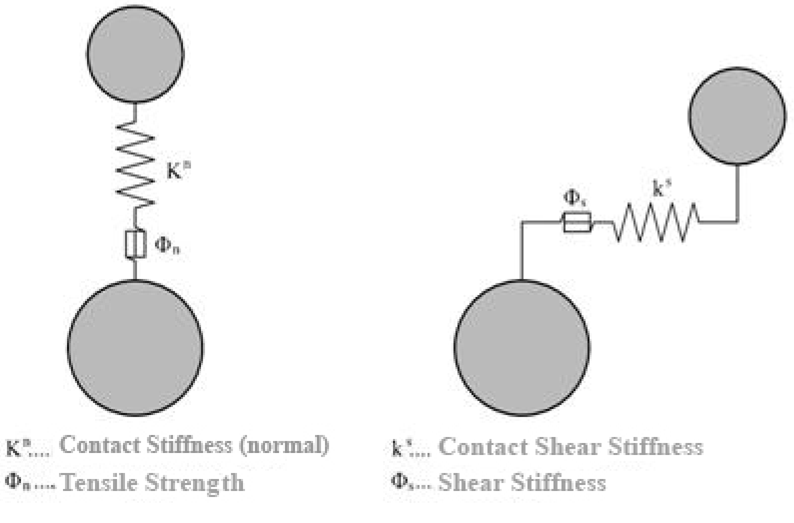

Figure 3.6 Illustration of Contact-Bond Model (PREH A. , 2004)

A contact bonding is a combination of a Hook (constant normal and shear stiffness) and a St. Venant body (constant tension and shear stiffness). If a bonding is in contact, then the bonded body can neither roll nor slide. First after the shear and tension strength is exceeded, they can split to perform a rolling or sliding motion.

If no overlapping occurs, then it is possible to determine the tensile force acting on the body, with the help of force-displacement law (see chapter 3.3). In this case, the contact bond acts to bind the balls together. The magnitude of the tensile normal contact force is limited by the normal contact bond strength.

A contact bond is defined by the following two parameters:

- Normal contact bond strength F_c^n
- Shear contact bond strength F_c^s

If the magnitude of the tensile normal contact force equals or exceeds the normal contact bond strength, the bond breaks, and both the normal and shear contact forces are set to zero. If the magnitude of the shear contact force equals or exceeds the shear contact bond strength, the bond breaks, but the contact forces are not altered, provided that the shear force does not exceed the friction limit and provided that the normal force is compressive.

The constitutive behavior relating the normal and shear components of contact force and relative displacement for particle contact occurring at a point are shown

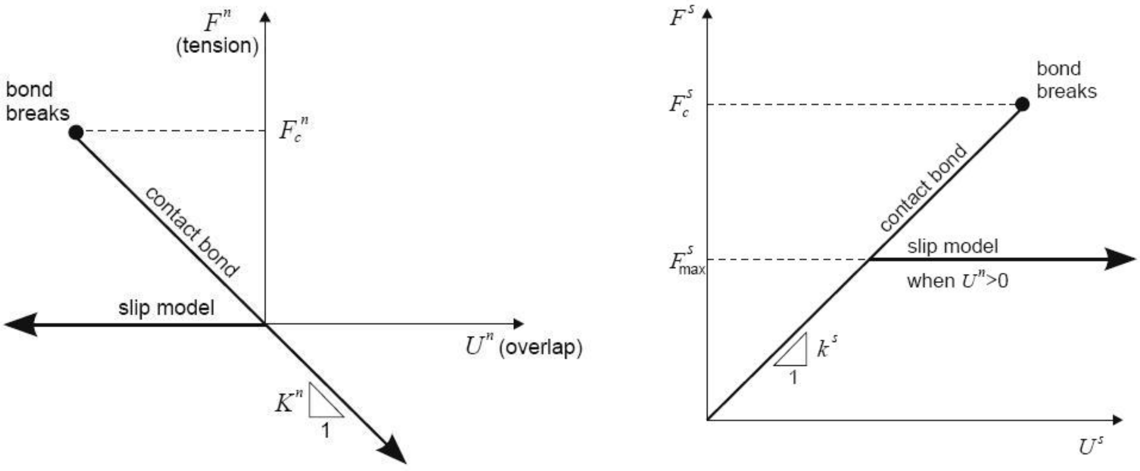

Figure 3.7 Constitutive behavior for contact occurring at a point. Left: Normal component of contact force, right: Shear component of contact force. (ITASCA, 2006)

In this figure F^n is the normal contact force and indicates tension if it is positive; U^n is the relative normal displacement and indicates overlap, if it is positive. F^s is the magnitude of the total shear contact force; and U^s is the magnitude of the total shear displacement measured relative to the location of the contact point when the contact bond was formed.

3.4.3.2 The Parallel-Bond Model

The parallel-bond model describes the constitutive behavior of a finite-sized piece of cementatious material deposited between two particles. These bonds establish an elastic interaction between particles that acts *in parallel* with the slip or contact-bond models described above. Thus, the existence of a parallel bond does not preclude the possibility of slip. Parallel bonds can transmit both forces and moments between particles, while contact bonds can only transmit forces acting at the contact point. Therefore, parallel bonds may contribute to the resultant force and moment acting on the two bonded particles.

A parallel bond can be envisioned as a set of elastic springs with constant normal and shear stiffnesses, uniformly distributed over a circular disk lying on the contact plane and centered at the contact point. These springs act in parallel with the point-contact springs that are used to model particle stiffness at a point. Relative motion at the contact (occurring after the parallel bond has been created) causes a force and a moment to develop within the bond material as a result of the parallel-bond stiffnesses. This force and moment act on the two bonded particles and can be related to maximum normal and shear stresses acting within the bond material at the bond periphery. If either of these maximum stresses exceeds the corresponding bond strength, the parallel bond breaks.

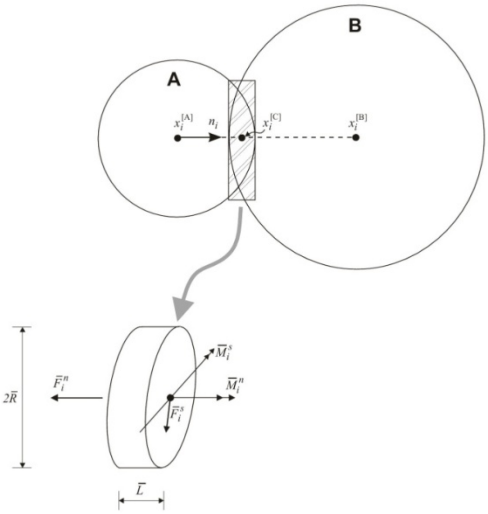

Figure 3.8 Parallel bond depicted as a cylinder of cementatious material. (ITASCA, 2006)

In Figure 3.8 parallel-bond is defined with the following parameters (MAIR am TINKHOF, 2007):

- Normal stiffness $\overline{k^n}$ [stress/displacement]
- Shear stiffness $\overline{k^s}$ [stress/displacement]
- Normal stress $\overline{\sigma_c}$ [stress]
- Shear stress $\overline{\tau_c}$ [stress]
- Bond radius $\bar{R}$

3.5 Law of Motion

The motion of a single rigid particle is determined by the resultant force and moment vectors acting upon it, and can be described in terms of the translational motion of a point in the particle and the rotational motion of the particle. The translational motion of the center of mass is described in terms of its position, x_i , velocity, $\dot{x}_i$, and acceleration, $\ddot{x}_i$; the rotational motion of the particle is described in terms of its angular velocity, ω_i , and angular acceleration, $\dot{\omega}_i$.

The equations of motion can be expressed as two vector equations, one of which relates the resultant force to the translational motion, and the other relates the resultant moment to the rotational motion. The equation for translational motion can be written in the vector form

$$F_i = m(\ddot{x}_i - g_i) \text{ (translational motion)} \tag{3.18}$$

$$M_i = \dot{H}_i \text{ (rotational motion)} \tag{3.19}$$

where F_i is the resultant force, the sum of all externally applied forces acting on the particle; m is the total mass of the particle; g_i is the body force acceleration vector (e.g., gravity loading); M_i is the resultant moment acting on the particle; and $\dot{H}_i$ is the angular momentum of the particle.

This relation is referred to a local coordinate system that is attached to the particle at its center of mass. This local system is oriented such that it lies along the principal axes of inertia of the particle, then Equ. (3.19) reduces to Euler's equation of motion:

$$\begin{aligned} M_1 &= I_1\dot{\omega}_1 + (I_3 - I_2)\omega_3\omega_2 \\ M_2 &= I_2\dot{\omega}_2 + (I_1 - I_3)\omega_1\omega_2 \\ M_3 &= I_3\dot{\omega}_3 + (I_2 - I_1)\omega_2\omega_1 \end{aligned} \tag{3.20}$$

where I_1, I_2, and I_3 are the principal moments of inertia of the particle;$\dot{\omega}_1$, $\dot{\omega}_2$, and $\dot{\omega}_3$ are the angular accelerations about the principal axes; and M_1, M_2, and M_3 are the components of the resultant moment referred to the principal axes.

For a spherical particle of radius *R*, whose mass is distributed uniformly throughout its volume, the center of mass coincides with the sphere center. Any local-axis system attached to the center of mass is a principal-axis system, and the three principal moments of inertia are equal to one another. Thus, for a spherical particle, Equ (3.20) can be simplified and referred to the global-axis system as

$$M_i = I\dot{\omega}_i = (\frac{2}{5}mR^2)\dot{\omega}_i \quad \text{(rotational motion)} \tag{3.21}$$

The equations of motion, given by (3.18), (3.21) are integrated using a centered finite-difference procedure involving a timestep of Δ*t*. The quantities $\dot{x}_i$ and ω_i are computed at the mid-intervals of *t* ± *n* Δ*t* /2, while the quantities x_i, $\ddot{x}_i$, $\dot{\omega}_i$, F_i and M_i are computed at the primary intervals of *t* ± *n* Δ*t*.

The following expressions describe the translational and rotational accelerations at time *t* in terms of the velocity values at mid-intervals. The accelerations are calculated as:

$$\ddot{x}_i^{(t)} = \frac{1}{\Delta t}\left(\dot{x}_i^{\left(t+\frac{\Delta t}{2}\right)} - \dot{x}_i^{\left(t-\frac{\Delta t}{2}\right)}\right)$$

$$\dot{\omega}_i^{(t)} = \frac{1}{\Delta t}\left(\omega_i^{\left(t+\frac{\Delta t}{2}\right)} - \omega_i^{\left(t-\frac{\Delta t}{2}\right)}\right) \tag{3.22}$$

Inserting these expressions into (3.18) and (3.21), solving for the velocities at time (*t* + Δ*t*/2), and using these equations to update the position of the particle as

$$x_i^{(t+\Delta t)} = x_i^{(t)} + \dot{x}_i^{\left(t+\frac{\Delta t}{2}\right)}\Delta t \tag{3.23}$$

The calculation cycle for the law of motion can be summarized as follows. Given the values of $\dot{x}_i^{(t-\Delta t/2)}$, $\omega_i^{(t-\Delta t/2)}$, $x_i^{(t)}$, $F_i^{(t)}$ and $M_i^{(t)}$, Equ. (3.23) is used to obtain $x_i^{(t+\Delta t)}$. The values of $F_i^{(t+\Delta t)}$ and $M_i^{(t+\Delta t)}$, to be used in the next cycle, are obtained by application of the force-displacement law.

3.6 Mechanical Timestep Determination

Choosing an appropriate timestep by motion integration is crucial to achieve an accurate solution to a rockslide case (FRÜHWIRT, 2004). Few differential equations are sensitive to rounding and hence denoted as unstable, which means, a small starting or rounding error during the calculation would grow to a mass failure and leads the user to a totally different situation. For this reason they should be handled with excess care. The equations of motion are integrated in *PFC* using a centered finite-difference equation scheme as expressed by Equ. (3.22). The computed solution produced by these equations will remain stable only if the timestep value does not exceed a critical timestep that is related to the minimum eigenperiod of the total system. However, global eigenvalue analyses are impractical to apply to the large and constantly changing systems typically encountered in a *PFC* simulation. Therefore, a simplified procedure is implemented in *PFC* to estimate the critical timestep at the start of each cycle. The actual timestep used in any cycle is taken as a fraction of this estimated critical value.

The estimation procedure for solution stability will be taken into account with the conception of a one-dimensional mass spring system described by a point mass, m, and string stiffness, k, with the coordinate system shown in Figure 3.9. The motion of the point mass is governed by the differential equation,

$$-kx = m\ddot{x} \tag{3.24}$$

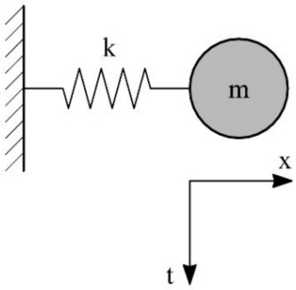

Figure 3.9 Single mass-spring system. (ITASCA, 2006)

The critical timestep corresponding to a second order finite-difference scheme for this equation is given by Bathe & Wilson (1976):

$$t_{crit} = \frac{T}{\pi};\ T = 2\pi\sqrt{\frac{m}{k}} \tag{3.25}$$

where T is the period of the system.

If infinite series of point masses and springs are considered, then the smallest period of this system will occur when the masses are moving in synchronized opposing motion such that there is no motion at the center of each spring. The motion of a single point mass can be described by the two equivalent systems shown in Figure 3.10. The critical timestep for this system is found using Equ. (3.25), to be

$$t_{crit} = 2\sqrt{\frac{m}{4k}} = \sqrt{\frac{m}{k}} \tag{3.26}$$

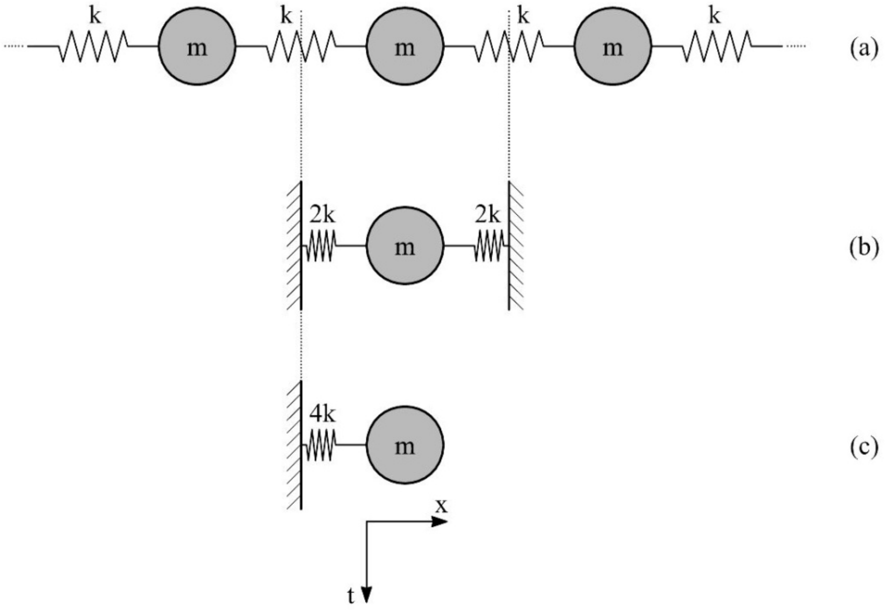

Figure 3.10 Multiple mass-spring system. (ITASCA, 2006)

The above two systems (Figure 3.9 and 3.10) characterize translational motion. Rotational motion is characterized by the same two systems in which mass, m, is replaced by moment of inertia, I, of a finite-sized particle, and the stiffness is replaced by the rotational stiffness. Thus, the critical timestep for the generalized multiple mass-spring system can be expressed as

$$t_{crit} = \begin{cases} \sqrt{m/k^{tran}}, & \text{(translational motion)} \\ \sqrt{I/k^{rot}}, & \text{(rotational motion)} \end{cases} \tag{3.27}$$

where k^{tran} and k^{rot} are the translational and rotational stiffnesses, respectively, and I is the moment of inertia of the particle.

The system modeled in *PFC* is a three-dimensional collection of particles and springs, each of which may have a different mass and stiffness. A critical timestep is found for each particle by applying equation (3.27) separately to each degree of freedom and assuming that the degrees of freedom are uncoupled. The stiffnesses are estimated by summing the contribution from all contacts, as described below. The final critical timestep is taken to be the minimum of all critical timesteps computed for all degrees of freedom of all particles.

3.7 Mechanical Damping

Energy supplied to the particle system is dissipated through frictional sliding. However, frictional sliding may not be active in a given model or, even if active, may not be sufficient to arrive at a steady-state solution in a reasonable number of cycles. For this reason in *PFC* three different damping models are introduced: a local non-viscous damping, a combined damping and a viscous damping.

3.7.1 Local Damping

The local damping used in *PFC* is similar to that described in CUNDALL (1987). A damping-force term is added to the equations of motion, given by equations (3.18) and (3.21), such that the damped equations of motion can be written as

$$\mathcal{F}_{(i)} + F^{d}_{(i)} = \mathcal{M}_{(i)}\mathcal{A}_{(i)};\ \ i = 1 \dots 6$$

$$\mathcal{M}_{(i)}\mathcal{A}_{(i)} = \begin{cases} m\ddot{x}_{(i)}, & \text{for } i = 1 \dots 3; \\ I\dot{\omega}_{(i-3)}, & \text{for } i = 4 \dots 6 \end{cases} \tag{3.28}$$

where $\mathcal{F}_{(i)}$, $\mathcal{M}_{(i)}$, and $\mathcal{A}_{(i)}$ are the generalized force, mass, and acceleration components, respectively; $\mathcal{F}_{(i)}$includes the contribution from the gravity force; and $F^{d}_{(i)}$ is the damping force:

$$F^{d}_{(i)} = -\alpha\left|\mathcal{F}_{(i)}\right| \operatorname{sign}\left(\mathcal{V}_{(i)}\right);\ \ \ i = 1 \dots 6$$

$$\operatorname{sign}(y) = \begin{cases} +1, & \text{if } y > 0; \\ -1, & \text{if } y < 0; \\ 0, & \text{if } y = 0 \end{cases} \tag{3.29}$$

expressed in terms of the generalized velocity

$$\mathcal{V}_{(i)} = \begin{cases} \dot{x}_{(i)}, & \text{for } i = 1 \dots 3; \\ \omega_{(i-3)}, & \text{for } i = 4 \dots 6 \end{cases} \tag{3.30}$$

The damping force is controlled by the damping constant α, whose default value is 0.7 and which can be specified separately for each particle.

This form of damping has the following advantages:

- Only accelerating motion is damped; therefore, no erroneous damping forces arise from steady-state motion.
- The damping constant, α, is non-dimensional.
- Since damping is frequency-independent, regions of the assembly with different natural periods are damped equally, using the same damping constant.

3.7.2 Combined Damping

The damping formulation described by equation (3.29) is only activated when the velocity component changes sign. In situations where there is significant uniform motion (in comparison to the magnitude of oscillations that are to be damped), there may be no “zero crossings” and, hence, no energy dissipation. An alternative (but less efficient) formulation is derived by noting that, for a single degree-of-freedom system executing harmonic motion, the derivative of the unbalanced force is proportional to negative value of the velocity. This alternative form of damping is called “combined damping”.

This form of damping should be used if there is significant rigid-body motion of a system in addition to oscillatory motion to be dissipated. However, combined damping is found to dissipate energy at a slower rate compared to local damping based on velocity, and therefore local damping is preferred in most cases.

3.7.3 Viscous Damping

In viscous damping the damping force is proportional to the velocity of the elements. When the viscous damping is active, normal and shear dashpots are added at each contact. These dashpots act in parallel with the existing contact model – for example, the linear contact model shown in Figure 3.11. A damping force, D_i ($i = n$: normal, s: shear) is added to the contact force, of which the normal and shear components are given by

$$D_i = C_i |V_i| \tag{3.31}$$

where C_i $(i = n\text{: normal}, s\text{: shear})$ is the damping constant, V_i $(i = n\text{: normal}, s\text{: shear})$ is the relative velocity at the contact, and the damping force acts to oppose motion. The damping constant is not specified directly; instead, the critical damping ratio β_i $(i = n\text{: normal}, s\text{: shear})$ is specified, and the damping constant satisfies

$$C_i = \beta_i C_i^{crit} \tag{3.32}$$

where C_i^{crit} is the critical damping constant, which is given by

$$C_i^{crit} = 2m\omega_i = 2\sqrt{mk_i} \tag{3.33}$$

where ω_i $(i = n\text{: normal}, s\text{: shear})$ is the natural frequency of the undamped system, k_i $(i = n\text{: normal}, s\text{: shear})$ is the contact tangent stiffness, and *m* is the effective system mass. In the case of ball-wall contact, *m* is taken as the ball mass, whereas in the case of ball-ball contact, *m* is given by

$$m = \frac{m_1 m_2}{m_1 + m_2} \tag{3.34}$$

where m_1 and m_2 are mass of the ball 1 and ball 2, respectively.

Viscous damping is characterized by the critical damping ratio *β* (GINSBERG & GENIN, 1984). When *β* = 1, the system is said to be critically damped, meaning that the response diminishes to zero at the most rapid rate. Also, *β* =1 represents the transition from an oscillatory response, when *β* < 1, to an exponentially decaying response when *β* > 1. When *β* < 1, the system is said to be underdamped, or lightly damped, and when *β* > 1, the system is said to be overdamped, or heavily damped.

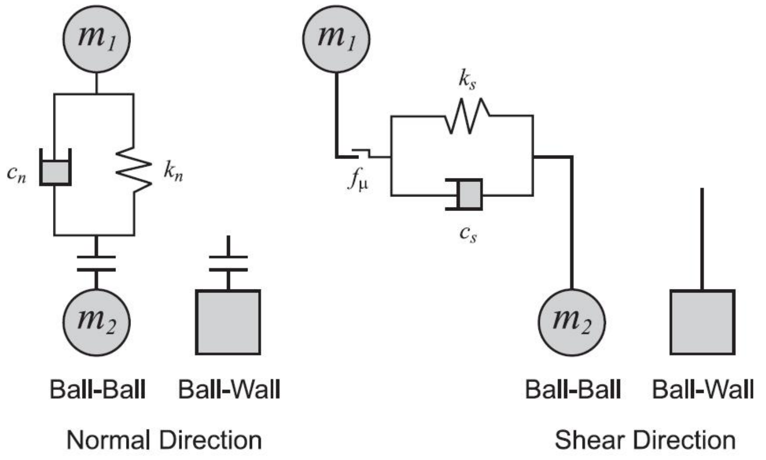

Figure 3.11 Viscous damping activated at a contact with the linear contact (ITASCA, 2006)

In *PFC*, the timestep is reduced (critical timestep with stiffness proportional damping) for stability when viscous damping is active. The reduced timestep with viscous damping is calculated as the minimum of critical timesteps computed for normal and shear directions using a different stiffnesses, k_n', k_s', where *n* indicates normal and *s* shear direction.

In rock fall programs, the rebound height of blocks touching the bedrock is calculated using restitution coefficients. The restitution coefficient R_i $(i = n\text{: normal}, s\text{: shear})$ is defined as the ratio of the contact velocity before and after the impact and can be defined as

$$R_i = \frac{v_i^f}{v_i^i} \tag{3.35}$$

where v_i^f $(i = n\text{: normal}, s\text{: shear})$ is the velocity of the block after the impact and v_i^i $(i = n\text{: normal}, s\text{: shear})$ is the velocity of the object before impact. The relation between the restitution coefficient R_i and the critical damping ration β_i can be estimated by simulation drop tests (see Figure 3.12) (PREH & POISEL, 2007).

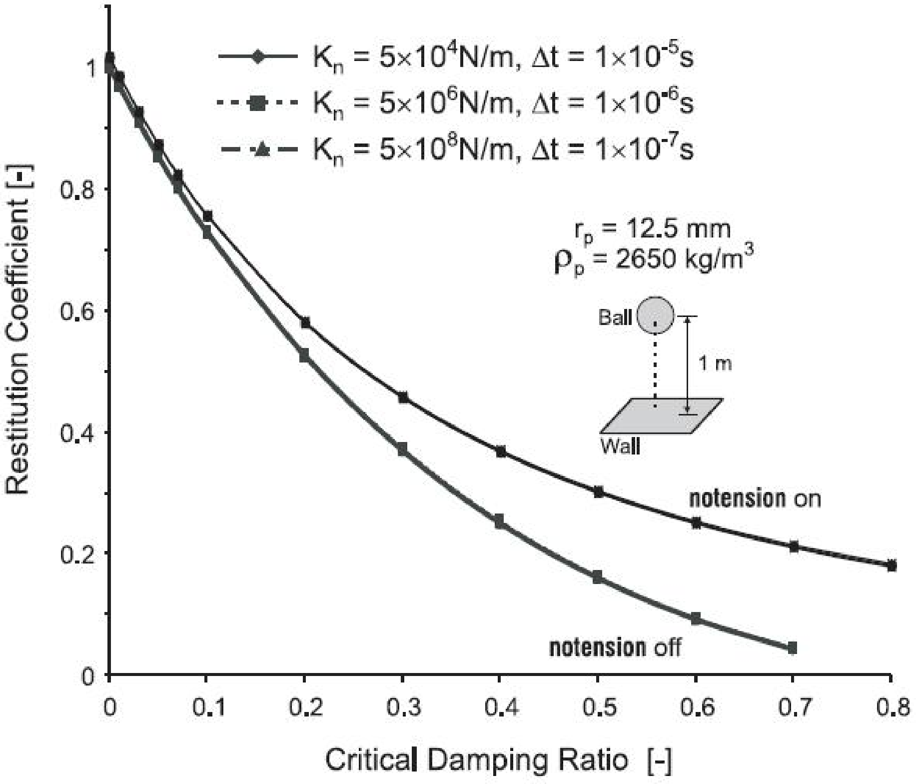

Figure 3.12 Relation between restitution coefficient and critical damping ratio (ITASCA, 2006)

4 Adjustment of *PFC*^{3D} for Modeling of a Rock Fall

4.1 Motion Mechanisms

According to observations in nature, several kinds of movements of the rock fall process have to be distinguished during the computation (BOZZOLO, 1987):

- free falling,
- bouncing,
- rolling and
- sliding

In order to achieve an appropriate simulation of these different kinds of movements by *PFC*, some modifications have been necessary using the implemented programming language *FISH* (PREH & POISEL, 2007)

4.1.1 Free Falling

In order to model the free falling of blocks, neither the acceleration nor the velocity (ignoring the air resistance) is to be reduced during fall as a consequence of mechanical damping.

As already explained in chapter 3.7.1 *PFC* applies a local, non-viscous damping proportional to acceleration, to the movement of every single particle as a default. This damping model best suits for a quick calculation equilibrium. There arises, however, a disadvantage of movement of particles being damped as well. Therefore, the local damping has been deactivated for all kinds of particle movements. (PREH & POISEL, 2007)

4.1.2 Bouncing

Elastic and plastic deformations occur in the contact zone during the impact of a block. Both the kinetic energy of the bouncing block and rebound height are reduced by the deformation work. The reduction of the velocity caused by the impact is modeled with the help of a viscous damping model integrated in *PFC* (PREH & POISEL, 2007), which is also explained formerly in chapter 3.7.3.

By modeling rock mass falls, it was shown to be necessary to distinguish between ball-ball contact and ball-wall contacts. This was done by using the programming language *FISH* (PREH & POISEL, 2007)

4.1.3 Rolling

For a realistic modeling of rock mass falls besides viscous damping, the rolling resistance should also be taken into account. If the rolling resistance is neglected, then the conceptual model would drift away from what is observed in nature.

The rolling resistance is caused by the deformation of the rolling body and/or the deformation of the ground (see Figure 4.1) and depends mostly on the ground and the block material.

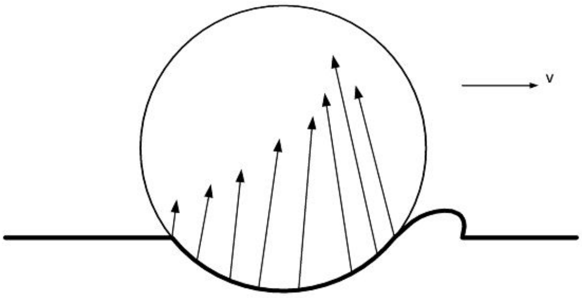

Figure 4.1 Deformation of the surface and distribution of contact stresses (PREH & POISEL, 2007)

Due to these deformations, the distribution of contact stresses between the ground and the block is asymmetric (see Figure 4.2). Replacing the contact stresses by equivalent static contact forces results in normal force *N*, which is shifted forward by the distance of c_{rr}, and a friction force F_{rr}, opposing the direction of the movement.

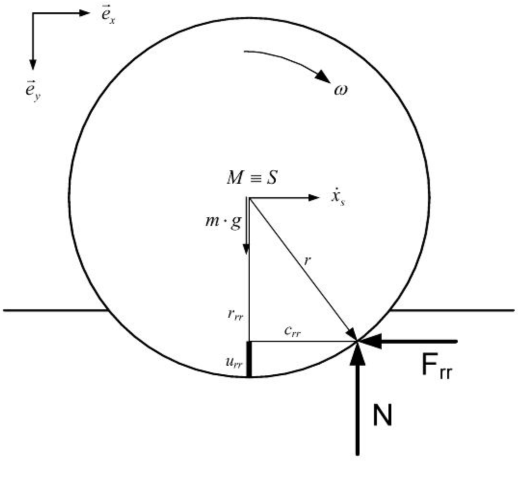

Figure 4.2 Calculation of the rolling resistance (PREH & POISEL, 2007)

The declaration of the angular velocity caused by the rolling resistance is calculated using the conservation of translational momentum (equ. 4.1) and angular momentum (equ 4.2)

$$m.\ddot{x}_s = -F_{rr} \tag{4.1}$$

$$-I.\dot{\omega}_{rr} = M_{rr}, I_{sphere} = \frac{2}{5}.m.r^2 \tag{4.2}$$

where M_{rr} is the resulting moment caused by the rolling resistance, I is the principal moment of inertia and ω_{rr} is the angular deceleration.

The kinematic link is established by the condition of pure rolling (equ 4.3)

$$\ddot{x}_s = \dot{\omega}.r \tag{4.3}$$

The angular acceleration is defined by a finite difference relation in order to express the increment of the angular velocity per time increment (equ 4.4). Thus, the friction force F_{rr} is defined by the conservation of momentum.

$$F_{rr} = -m.\frac{\Delta\omega_{rr}}{\Delta t}.r \tag{4.4}$$

Equation (4.2) and (4.4) yield to

$$-\frac{2}{5}.m.r^2.\frac{\Delta\omega_{rr}}{\Delta t} = F_{rr}.r_{rr} - N.c_{rr} \tag{4.5}$$

$$-\frac{2}{5}.m.r^2.\frac{\Delta\omega_{rr}}{\Delta t} = -m.\frac{\Delta\omega_{rr}}{\Delta t}.r.r_{rr} - m.g.c_{rr} \tag{4.6}$$

Therefore, the angular deceleration is

$$\Delta\omega_{rr} = \frac{-g.c_{rr}}{r.(r_{rr}-\frac{2}{5}.r)}.\Delta t\,; \qquad r_{rr} = \sqrt{r^2 - c_{rr}^2} \tag{4.7}$$

The rolling resistance is implemented by adding the calculated increment of the angular velocity, to the angular velocity calculated by *PFC* at every timestep. (Equ. 4.7).

$$\omega_i^{(t)} = \omega_i^{(t)} + \Delta\omega_{rr,j} \tag{4.8}$$

According to these considerations, the rolling resistance is an eccentricity c_{rr} or sag function u_{rr}. The deeper the block sags, the greater the rolling resistance, $\Delta\omega_{rr}$.

This means that spherical blocks of different sizes have the same run out for the same rolling resistance coefficient. In nature, however, it can be observed that large blocks generally have a longer run out than smaller ones. Therefore, according to the damping model described, the run out is calibrated by the sag u_{rr}.

There has been several model calculations carried out by *PFC*, using the model of rolling resistance just described. When the detached rock mass was modeled as an irregular assembly of two different sized particles, it became apparent that the larger particles have a longer run out than smaller ones (PREH & POISEL, 2007). Below Figure 4.3 demonstrates an inverse grading of a deposit mass simulated by *PFC*.

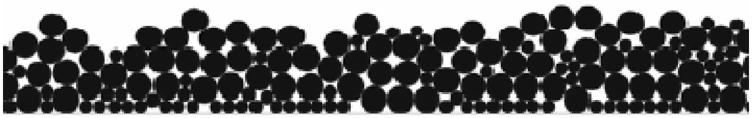

Figure 4.3 Inverse grading of a deposit mass simulated by *PFC* (PREH & POISEL, 2007)

4.1.4 Sliding

Sliding is calculated by the slip model implemented in *PFC* (see chapter 3.4.2). No further adjustments are necessary. Various friction coefficients are introduced to the areas with different character (e.g. glacial, outcropping rock, etc.), thus it could be possible to get contrasting sliding behaviors of a ball, which has a trajectory lying on several areas. For a ball-ball interaction another friction coefficient is also introduced. The calculation selects the smallest value of friction coefficient, when it comes for a ball to contact with several elements, belonging to different characters.

4.2 Damping Factors and Micro Parameters

The damping factors and micro parameters that are introduced to achieve a realistic model can be categorized into two parts:

1. Parameters to model the interaction between ball and wall elements:
   - Normal stiffness of wall elements [force/displacement]
   - Shear stiffness of wall elements [force/displacement]
   - Friction coefficient, ball-wall [-]
   - Rolling resistance [length, sinking depth]
   - Critical normal damping behavior, ball-wall [-]
   - Critical shear damping behavior, ball-wall [-]
2. Parameters to model ball properties and the interaction between ball elements:
   - Normal stiffness of ball elements [force/displacement]
   - Shear stiffness of ball elements [force/displacement]

- Contact bonding (Normal direction) [force]
- Contact bonding (Shear direction) [force]
- Friction coefficient, ball-ball [-]
- Critical normal damping behavior, ball-ball [-]
- Critical shear damping behavior, ball-ball [-]

4.3 The Kinetic Energy and Velocity Lines

In order to have an idea about the motion behavior of rock mass falls, it is necessary to record physical properties of the mass like velocity and kinetic energy during the rock fall process. A *FISH* routine is developed manually to store the desired velocity and kinetic energy diagrams of the rock fall.

The following parameters are introduced using the implemented *FISH* language to obtain the desired information about the velocity and energy situations of the total mass:

- Average scalar and angular velocities of total mass,
- Maximum velocity of the fastest ball in each case,
- Kinetic energy, translational and rotational energy,
- Maximum kinetic energy of a selected ball from total mass

during the calculation of the parameters over the total collapse time of the mass is used (MAIR am TINKHOF, 2007).

PFC has the capability of calculating the x, y and z coordinates and the scalar/angular velocities of any ball at each timestep. By implementing the developed *FISH* routine it is possible to calculate the translational and angular velocities of a selected ball or total mass by using the following equations:

$$|\vec{v}_{ball}| = \sqrt{v_x^2 + v_y^2 + v_z^2} \tag{4.9}$$

$$|\vec{\omega}_{ball}| = \sqrt{\omega_x^2 + \omega_y^2 + \omega_z^2} \tag{4.10}$$

The maximal angular velocity (ω_{max}) and translational velocity (v_{max}) of the total mass is also calculated and written in a diagram showing the velocity lines and the elapsed time. The vectors of the total velocity unfold generally a little about the direction and the instantaneous situation of the falling mass, for that reason they are not included in this work.

The equations used in the calculation of the average scalar and angular velocities are shown below as:

$$v_{ave} = \frac{\sqrt{\left(\sum_{i=1}^{n} v_{x,j}\right)^2 + \left(\sum_{i=1}^{n} v_{y,j}\right)^2 + \left(\sum_{i=1}^{n} v_{z,j}\right)^2}}{n}; \text{ n...number of balls} \quad (4.11)$$

$$\omega_{ave} = \frac{\sqrt{\left(\sum_{i=1}^{n} \omega_{x,j}\right)^2 + \left(\sum_{i=1}^{n} \omega_{y,j}\right)^2 + \left(\sum_{i=1}^{n} \omega_{z,j}\right)^2}}{n}; \text{ n...number of balls} \quad (4.12)$$

Unlike the total velocity diagram, the average velocity diagrams show a good agreement with the detached mass behavior.

PFC provides a possibility of calculating the kinetic energy of the total mass without further implementation of any routine. This possibility is used to cross-check the manually calculated energy histories.

The translational energy of a falling mass is calculated by

$$E_{tran} = \frac{1}{2}.m.|\vec{v}_{ball}|^2 \quad (4.13)$$

and the rotational energy by

$$E_{rot} = \frac{1}{2}.I.|\vec{\omega}_{ball}|^2 \quad (4.14)$$

where *I* is the mass moment of inertia of the block and calculated as follows

$$I_{sphere} = \frac{2}{5}.m.r^2 \quad (4.15)$$

So the kinetic energy of a particle is calculated by

$$E_{kin} = E_{tran} + E_{rot} \quad (4.16)$$

The total kinetic energy, translational kinetic energy and rotational kinetic energy are a summation of the relevant particle energy calculations and given as follows

$$E_{kin,tot} = \sum_{i=1}^{n} E_{kin,j} \; ; \text{ n...number of balls} \quad (4.17)$$

$$E_{tran,tot} = \sum_{i=1}^{n} E_{tran,j} \; ; \text{ n...number of balls} \quad (4.18)$$

$$E_{rot,tot} = \sum_{i=1}^{n} E_{rot,j} \; ; \text{ n...number of balls} \quad (4.19)$$

During a simulation it is probable that a single block can fall outside the monitored rockslide area to start an endless free fall. This situation will certainly disturb/falsify the velocity and energy diagrams, for that reason a *FISH* routine is written to delete these balls to prevent the falsification of the diagrams. Because the balls, which fell out of raster, are not that much (generally in magnitude ~5%) compared to the total generated ball-mass, it could be assumed without any hesitation that the deletion of these particles would not disturb the simulation.

4.4 Abort Criterion

Any abort criterion is not predefined in *PFC*. As a result of this, an abort criterion should be assigned to stop the simulation after a satisfied solution is gathered. This stoppage could be done by introducing a certain number of calculation steps or a tolerance criterion. Introducing a certain number of calculation steps requires the knowledge of the development of the rock fall process in advance, but this information is in general not available (FRÜHWIRT, 2004).

For that reason a tolerance criterion is introduced as an abort criterion. A small “if-loop” is introduced by a *FISH* routine, that if the maximal velocity of the total mass falls under 0.1 m/s, then it is assumed that the falling process has come to an end, so the program aborts the process. The calculation is limited also with a certain number of calculation steps, so if the calculation does not yield an equilibrium state, then it indicates that the selected parameters, which were defined in chapter 4.2, do not reflex a suitable solution and should be rearranged.

.

5 Case 1: Punta Thurwieser Rock Avalanche (Italy)

5.1 Introduction

The first case investigated was the rock avalanche that took place on September 18th, 2004 on the southern flank of the Punta Thurwieser (Italian designation for Peak Thurwieser) with peak elevation of 3,641 m above the sea level, located at the closing of the Zebrù Valley, in the Central Italian Alps (SOSSIO & CROSTA, 2007).

The Zebrù Valley is a part of the Ortler Alps (in Italian Ortles) in the central Alps of Italy. They are considered to be a part of Central-Eastern Alps or the Southern Limestone Alps (WIKIPEDIA, 2007). The table below shows the main peaks that belong to the Ortler Alps.

Table 5.1 The Main Peaks of the Ortler Alps (WIKIPEDIA, 2007)

Peak (*Italian*)	**(*German*)**	**metres**	**feet**
Ortles	Ortler	3,905	12,811
Gran Zebrù	Königsspitze	3,857	12,655
Monte Cevedale	Zufallspitze	3,774	12,382
Monte Zebrù		3,735	12,254
Palón della Mare		3,705	12,156
Punta San Matteo		3,692	12,113
Punta Thurwieser	Thurwieserspitze	3,641	11,946
Pizzo Tresero		3,602	11,818
Cima Vertana	Vertainspitze	3,541	11,618
Punta delle Bàite	Tuckettspitze	3,458	11,346
Cima Venezia	Veneziaspitze	3,384	11,103
Croda di Cengles	Tschenglser Hochwand	3,378	11,083
Monte Confinale		3,370	11,057
Monte Sobretta		3,296	10,814

5.2 Geological Conditions, Morphological Characteristics and Geomechanical Interpretations

The Zebrù valley is a 10 km long valley of glacial origin, with a NE-SW trend. The morphology of the valley has been sculpted by glacial and hydraulic processes. The valley traces the tectonic Zebrù line, separating the Palaeozoic Campo Alps, to the south, and the

Mesozoic Ortler Alps, to the north. The lithology of the Campo Alps mainly consists of phyllite and paragneiss, with intercalations of marble, amphibolite and porphyry, whereas lithology of the Ortler Alps consists of dolostone with intercalations of limestone.

The detachment area is located at an approximate elevation of 3600 m a.s.l. on the east face of Punta Thurwieser, just below its peak. The estimated overall volume of the landslide is $2.5 \times 10^6 m^3$. The rock avalanche dropped and partly moved on the surface of the underlying Zebrù Glacier; after crossing a high rock step (named as “outcropping rock” below), the rock mass flew along the narrow Rin Mare valley stopping at an elevation of about 2235 m a.s.l. The overall run out length was about 3000 m. (PIRULLI, et al., 2006). The detachment area (in green dots) and the flowing region of the detached rock (in white dots) are shown in Figure 5.1.

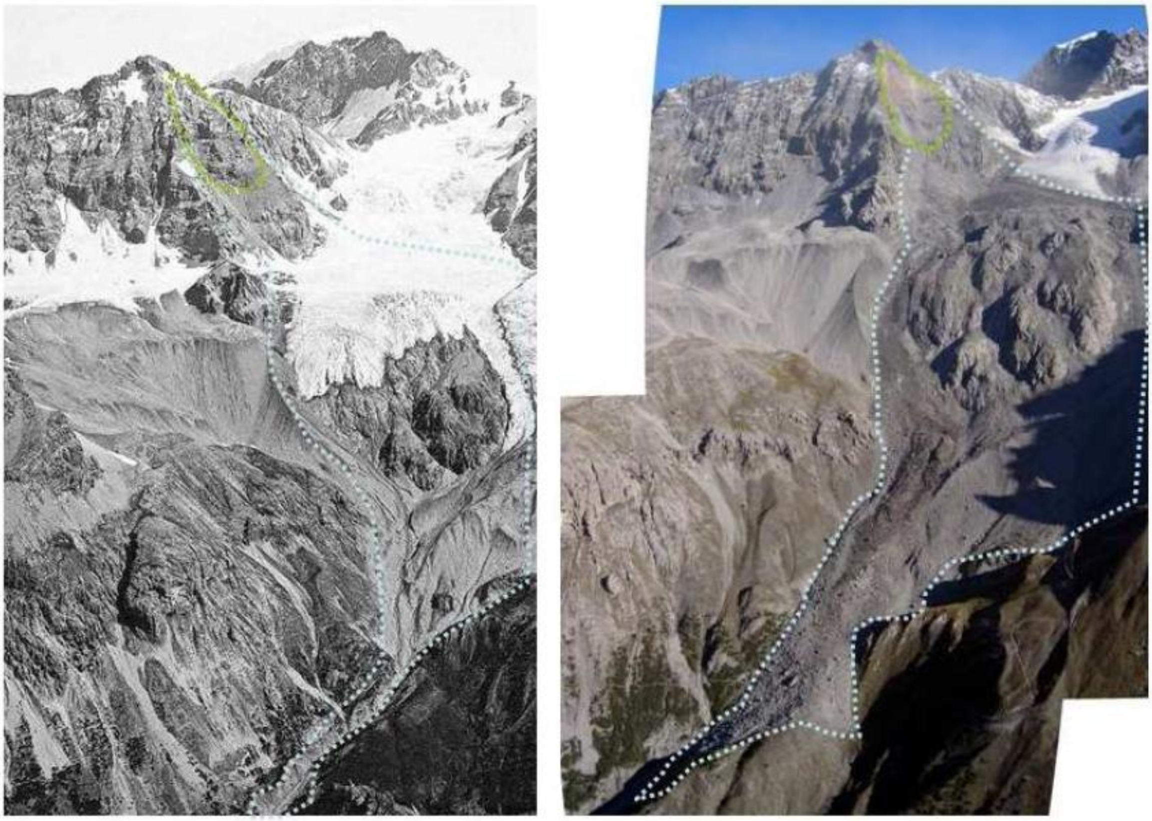

Figure 5.1 Thurwieser Peak, before (left) and after (right) the rock avalanche (SOSSIO & CROSTA, 2007)

As seen in Figure 5.1, the upper part of the glacial floor is covered with ice (i.e. Zebrù Glacier), and then glacial deposits and exposed rock (outcropping rock). In particular, the lateral moraines due to the ancient glaciers and the outcropping rocks confined the landslide spreading.

The detachment of the rock avalanche exposes a reddish surface due to the weathering processes undergone by the fissured rock. This fracturing system and the action of tectonization processes throwing over cataclastic and mylonitic rock contributed to the weakening of the mass. (SOSSIO & CROSTA, 2007)

The permafrost degradation is supposed to be the most probable triggering factor. Similar phenomena, even with lower volumes, have been occurring since summer 2003 in the Alps (Bernina, Matterhorn, Mont Blanc) following periods of exceptionally high temperatures (PIRULLI, et al., 2006)

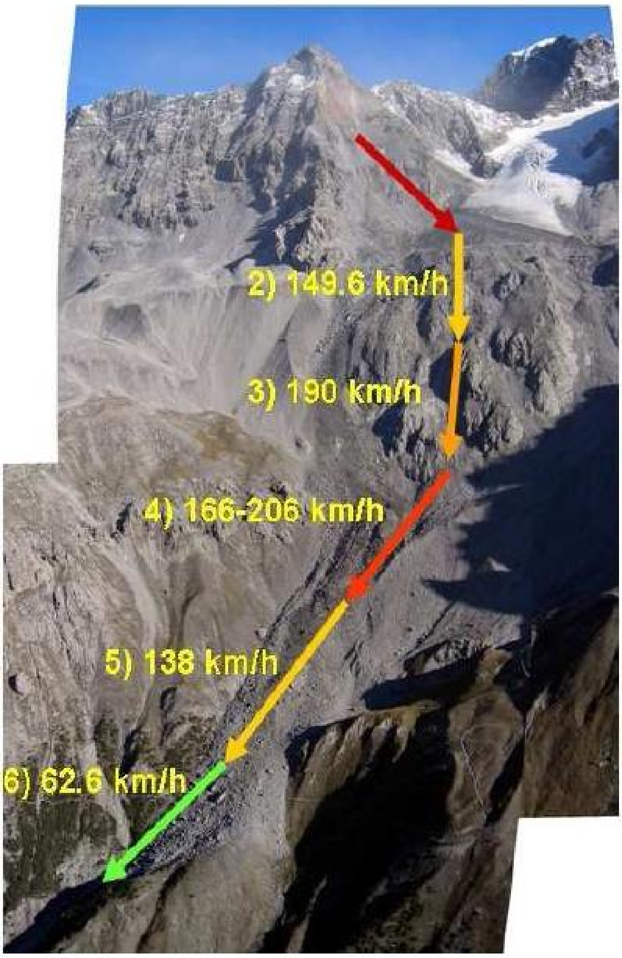

Figure 5.2 The velocities of the detached mass at several regions acquired from the movie shot on actual event (SOSSIO & CROSTA, 2007)

The rock avalanche is the first video recorded rock avalanche ever. The recorded movie revealed the timing and the evolution of the landslide. The measurements from the available movie indicated the relevant velocities at particular regions of the slope (see Figure 5.2).

The landslide propagation lasted less than *75-80 seconds*, while the mean front velocity was about *40 m/s*, with the highest velocities reached along the glacier and down the outcropping rock (Figure 5.2). The main deposit stopped few hundreds meters far from the Zebrù main valley, but the dust cloud extended up to 4 km far from the source area (SOSSIO & CROSTA, 2007).

5.3 Model Setup

Two steps have to be fulfilled for an adequate model build-up with PFC^{3D}, namely:

1. The modeling of the non-moved bed rock surface
2. The modeling of the detached rock mass

5.3.1 Modeling of the Surface

Generating a digitalized model of a surface requires a digital elevation model (DEM) or a digital terrain model (DTM) of the surface. A DEM is a digital representation of the ground, it is also widely known as DTM. DEM's can be represented as a raster (a grid of squares) or a triangular irregular network. They are commonly built using remote sensing techniques; however, they may also be built from land surveying.

Assessing a DEM requires a digitalized measurement of the region, which needs to be modeled. *The committee of International Landslide Forum* provided such data. The data folder consisted of mainly three spreadsheets:

1. DEM path Thurwieser Surface
2. DEM source Thurwieser Solid Rock
3. DEM source Thurwieser Expanded

The surface data was used to generate the non-moved bed rock surface in general, whereas the solid rock file represents the surface of the detached mass. The Thurwieser Expanded file represents the surface of the detached loose rock (h' = h x 1.5). All three files consisted of three dimensional coordinates (*x, y and z*) of a field in 10 m raster. Based on these raster coordinates a digitalized field was constructed using AUTODESK LAND DESKTOP 3 (See Figure 5.3).

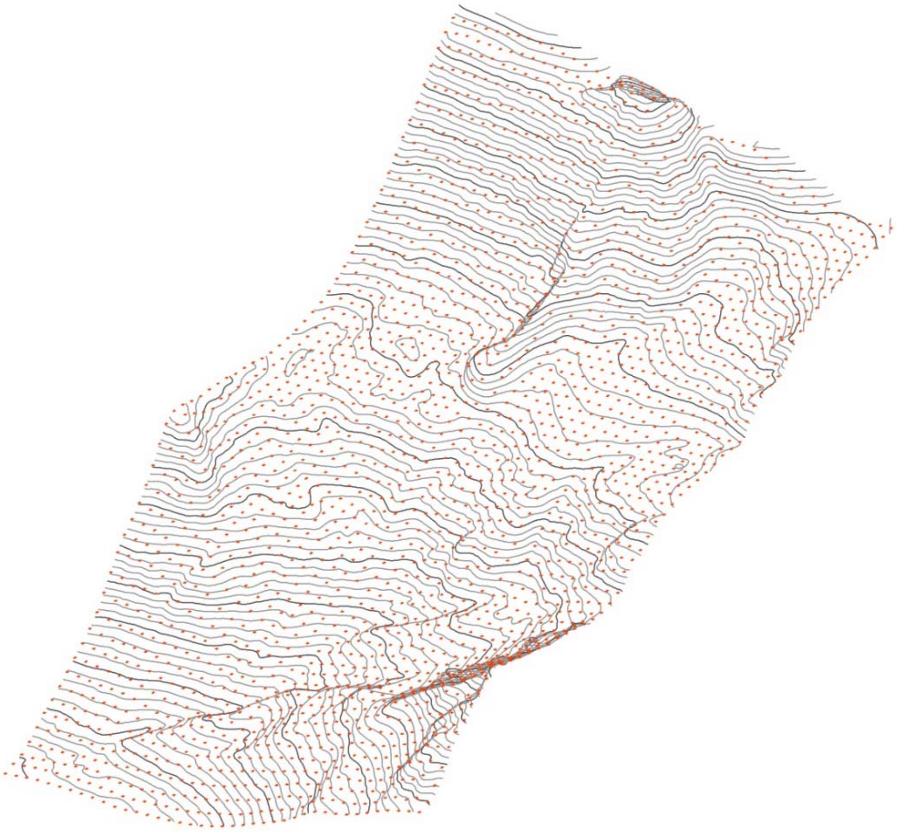

Figure 5.3 Axonometric view of the rockslide area with 10 m contour lines and the red marked raster points (50 x 50 m)

Although a smaller raster field could be generated, a 50 x 50 m raster was selected, because a smaller raster would have caused extremely long *PFC* simulations.

In the next step, separate regions with different frictional coefficients were defined using the ground plans provided by Landslide Forum. Figure 5.4 illustrates the position of *the glacier*, and of *the detachment area* and *the final depth (thickness) of the rockslide material* at its end position.

In order to simulate a rock mass fall coinciding with the actual behavior of the detached mass, different parameters had to be introduced which would be relevant for a real rockslide run out (e.g. small friction coefficient for glacial areas, whereas higher value for rocky, rough areas). These different areas in terrain surface are as follows:

1. The detachment area
2. Glacier
3. Outcropping rock
4. Surface (Normal terrain – Glacial deposits)

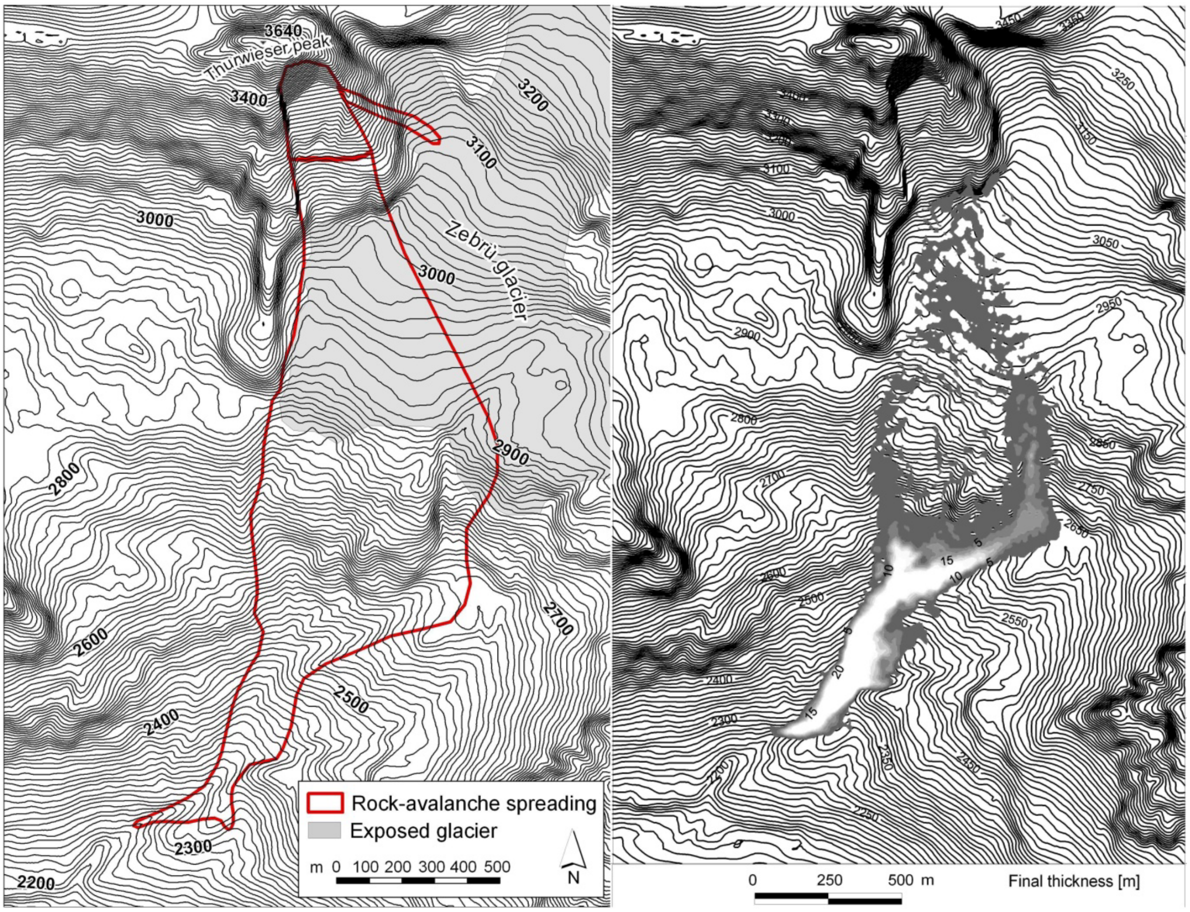

Figure 5.4 The ground plans provided from Landslide Forum, left: the initial position and the run out path of the detached mass; right: the position and final thickness of the deposit.

Finally, the raster points from the digitalized model were written in a text document, so that it could be possible for *PFC* to generate a terrain model based on these raster points later. The terrain model generated by *PFC* is demonstrated in Figure 5.5 and 5.6, where blue indicates the glacier, brown the outcropping rock, red the detachment area, and black regions the glacial deposits.

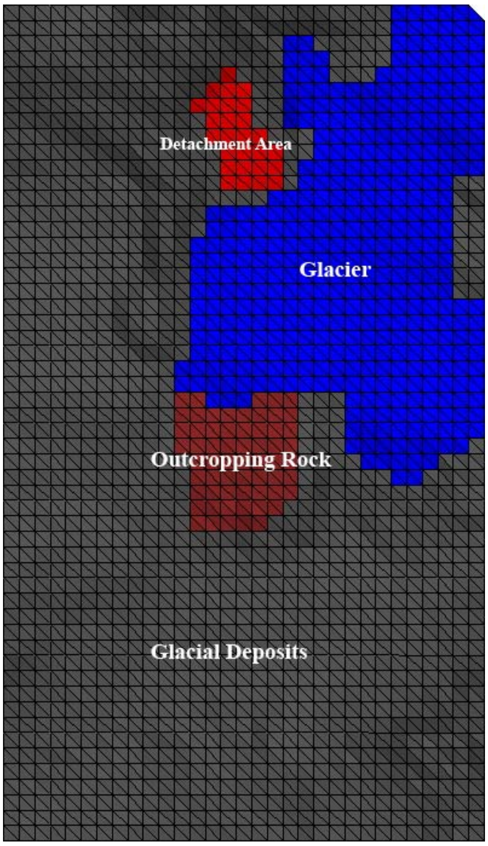

Figure 5.5 Different homogeneous regions of the constructed model by *PFC*

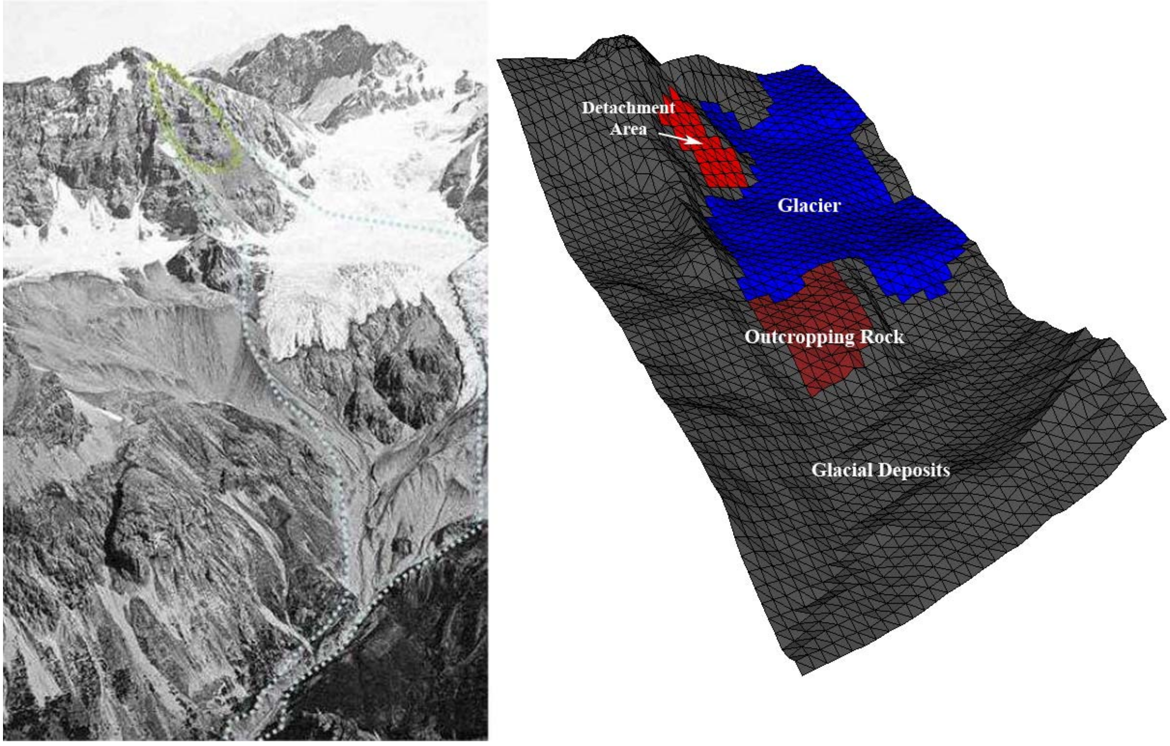

Figure 5.6 The surface model (right) and the actual photo shot (left) (SOSSIO & CROSTA, 2007)

5.3.2 Modeling of the Detached Rock Mass

The generation of the detached particles as well as the build up of the wall elements defining the surface were simulated by *PFC*. First the surface points were read from the DEM file and rearranged as a 50 m raster as an input file for the *PFC* program. After the reading of these points by *PFC*, the program constructed triangulated wall elements (See Figure 5.5 and 5.6). The triangulation was done by a *FISH* routine designed by PREH (2004). The allocation of the run out relevant parameters (e.g. rolling resistance, friction and damping coefficients) were carried out after the particle generation of the detached rock volume.

The initial positions of the particles were modeled in a form such that the generated balls would be placed in a closed cap form, which was sealed with a cover element. Consequently the detached rock mass that should stay at rest at the beginning could be modeled. This cover was designed as a cap-like structure of wall elements which were also created by *PFC* to hold the particles in their initial position. The generated balls were randomly placed between the cover and the predefined detachment area. The definition of the detachment area was carried out according to the provided ground plans (Figure 5.7).

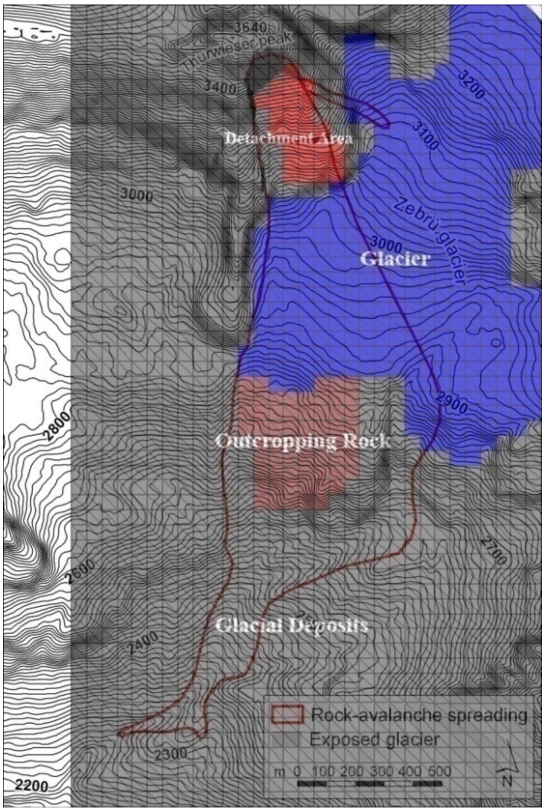

Figure 5.7 The determination of the different areas in *PFC*

The modeling of the detachment and the start of the run out were initiated by the deletion of the cover wall elements to release the particles. At the initial position, the particles must have zero velocity, thus zero kinetic energy. However, after the random radius expansion of the particles during their generation between the detachment surface and cover surface and after the deletion of the cover surface, the particles hurled in different directions due to the initial energy they possess. Thus 500 steps were conducted at the beginning of the run out, so that a better distribution of particles was achieved without having any initial velocity.

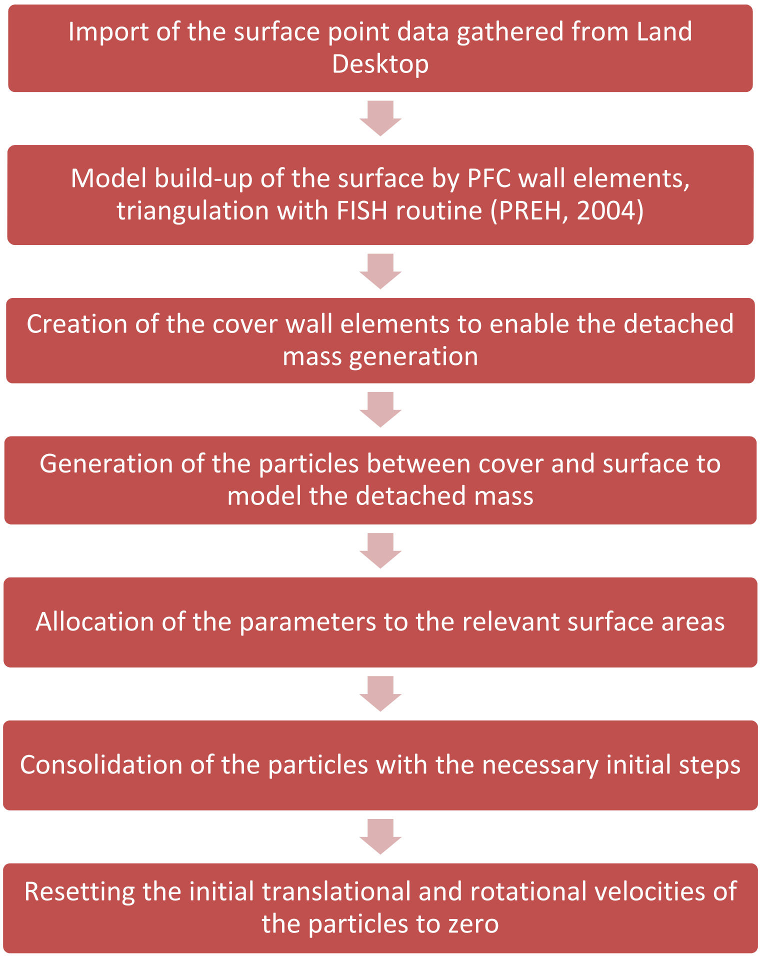

Figure 5.8 Flowchart of particle generation and construction of the surface model

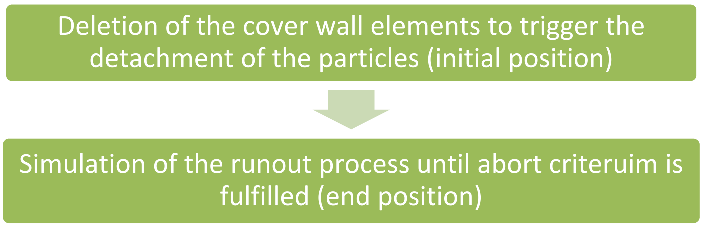

Figure 5.9 Flowchart of the run out simulation

5.4 Run out Modeling

The digital elevation model provided by the Int. Landslide Forum in Hong Kong was used to generate the terrain surface model by wall elements, explained already in chapter 5.3. The terrain was generated by 3,348 wall elements, simulating both the detachment and the surface terrain itself. The detached, mostly dolomite, rock was modeled by 2,632 particles (balls) with random generated balls, radius length ranging between $r_{min} = 6\ m$ and $r_{max} = 11\ m$. After starting the run out process by deleting the wall elements above the detached rock volume, 250.000 timesteps were calculated (POISEL, PREH, & KOÇ, 2007).

5.4.1 Initial Position

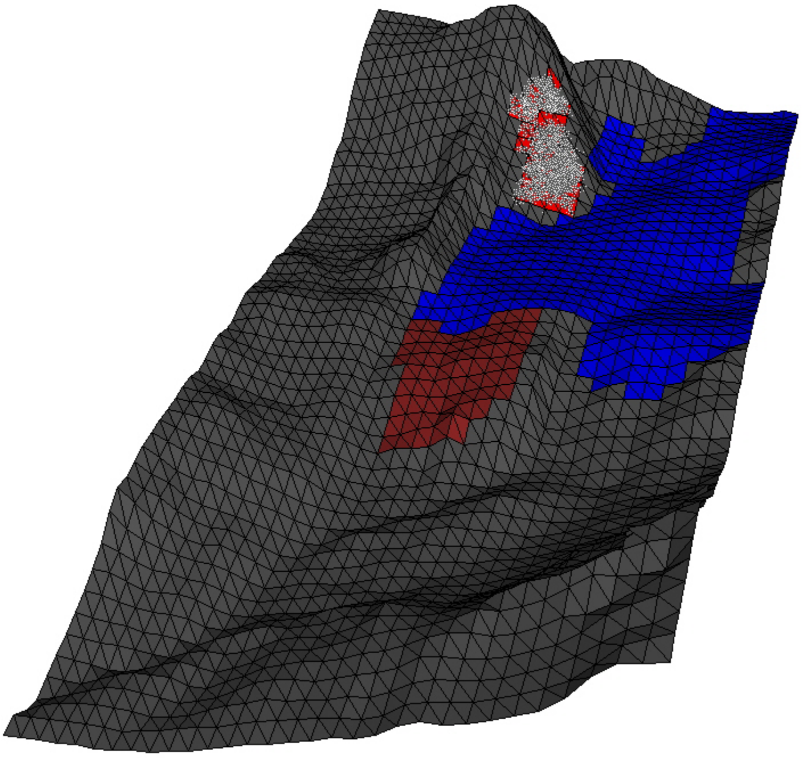

Figure 5.10 Punta Thurwieser, three dimensional view of the initial position of the particles

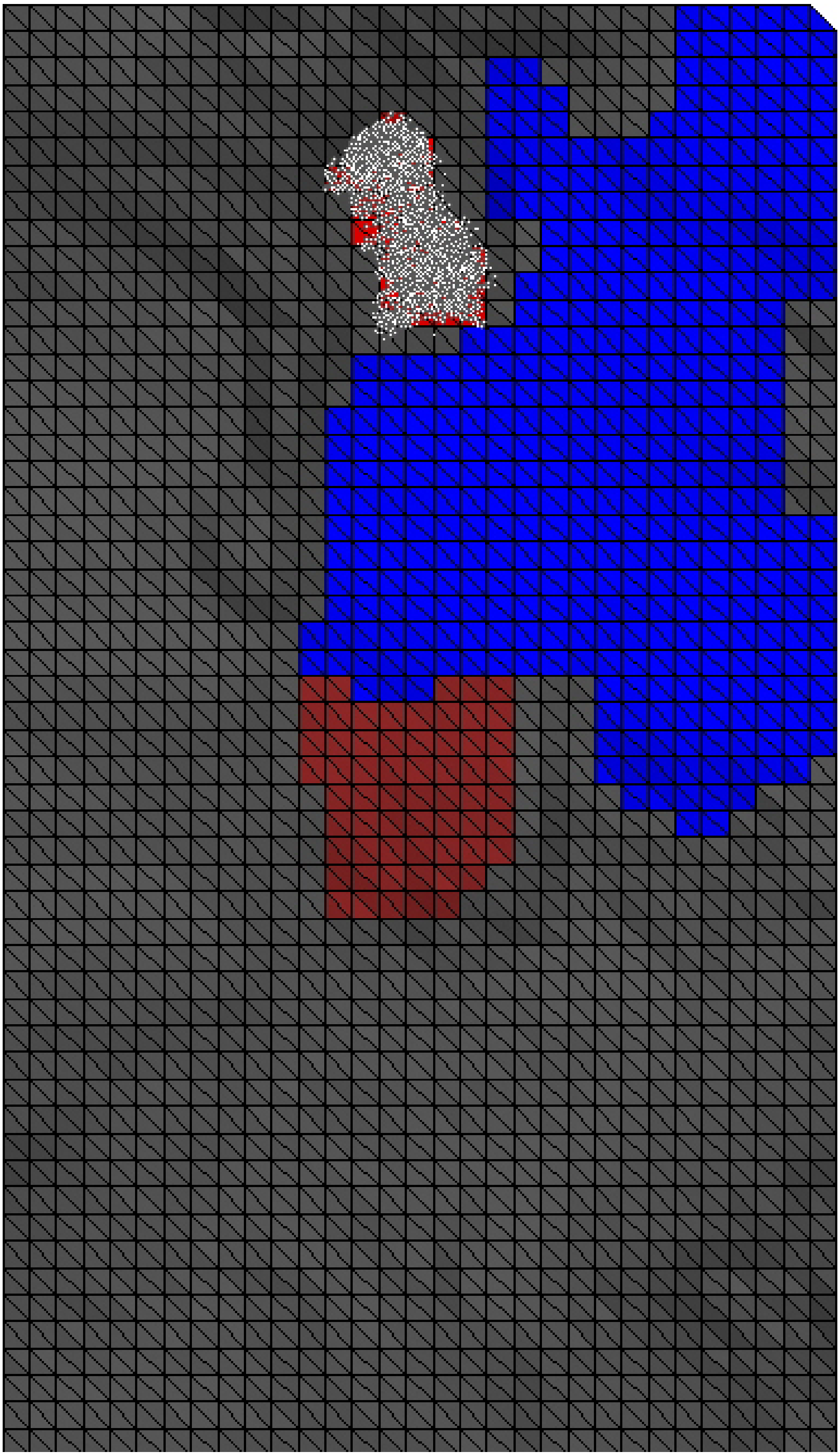

Figure 5.11 Punta Thurwieser, initial position, plan view

5.4.2 Parameter Study

A parameter study was carried out in order to evaluate the best fit parameters for simulation of the Punta Thurwieser rock avalanche corresponding with reality. Achieving the best fit parameters could only be managed by conducting several run out experiments, in which the parameters were redefined each time depending on the simulation results.

The experiments were planned generally in two branches: the detached rock volume as loose material (Expanded Rock) and as solid material (Solid Rock) (See chapter 5.3.1). The experiments carried out on loose material (expanded rock) certainly provide more particles and consequently a run out simulation closer to the observations (height and depth distribution of the deposit) than the solid material would do, but it would eventually lead to a higher calculation time. On the other hand, experiments which were conducted on solid material (solid rock) would generate fewer particles but ensure a favorable computational time. The experiments were also categorized by their friction angle. The chart below shows the experiment branches in detail with the relevant experiment numbers beneath.

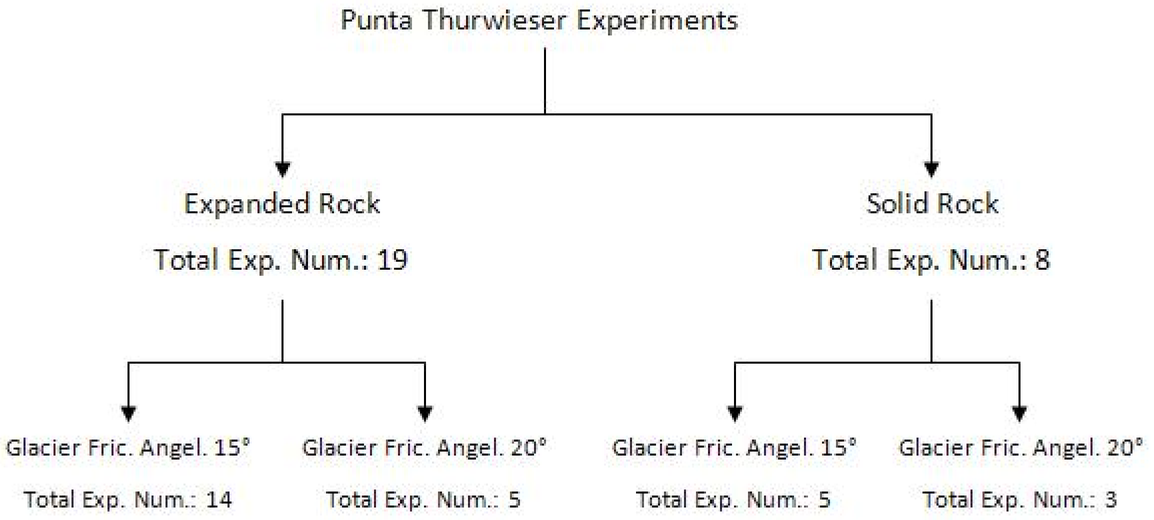

Figure 5.12 Types of experiments and the total number conducted

Table 5.2 shows all parameters used. As seen in this table, the critical damping ratios (See chapter 3.7.3) for all regions were taken as 0.8. This was due to the excessive bouncing motion of the balls over the region “Outcropping Rock”. To prevent this action, the damping ratios were taken at their limits, so that the excessive bouncing movement of the particles was clearly decreased (See Figure 3.12).

Table 5.2 Best fit parameters for simulating Punta Thurwieser Rock Avalanche

Thurwieser Experiment for Expanded Rock (Glacier 15 Grad)	**Best Fit - Exp. 9**
Common Parameters for all Regions	
Number of Timesteps [-]	250.000
Volume [m^3]	$2,2*10^6$
Number of Wall Elements (Surface)	3.348
Number of Wall Elements (Cover)	122
Number of Particles (Balls)	2.632
Range of Ball Radius [m]	6,0 - 11,0
Porosity [%]	35
Parameters for Region "**Detachment Area**"	
Normal Stiffness [kN/m^2]	$1*10^6$
Shear Stiffness [kN/m^2]	$1*10^6$
Friction Coeff. (ball-wall) [-]	tan 40° = 0,839
Rolling Resistance [m]	0,5
Critical Damping Ratio (Normal Direction) (ball-wall) [-]	0,8
Critical Damping Ratio (Shear Direction) (ball-wall) [-]	0,8
Parameters for Region "**Glacier**"	
Normal Stiffness [kN/m^2]	$1*10^6$
Shear Stiffness [kN/m^2]	$1*10^6$
Friction Coeff. (ball-wall) [-]	tan 15° = 0,268
Rolling Resistance [m]	0,6
Critical Damping Ratio (Normal Direction) (ball-wall) [-]	0,8
Critical Damping Ratio (Shear Direction) (ball-wall) [-]	0,8
Parameters for Region "**Outcropping Rock**"	
Normal Stiffness [kN/m^2]	$1*10^6$
Shear Stiffness [kN/m^2]	$1*10^6$
Friction Coeff. (ball-wall) [-]	tan 45° = 1
Rolling Resistance [m]	0,4
Critical Damping Ratio (Normal Direction) (ball-wall) [-]	0,8
Critical Damping Ratio (Shear Direction) (ball-wall) [-]	0,8
Parameters for Region "**Glacial Deposits**"	
Normal Stiffness [kN/m^2]	$1*10^6$
Shear Stiffness [kN/m^2]	$1*10^6$
Friction Coeff. (ball-wall) [-]	tan 60° = 1,732
Rolling Resistance [m]	0,4
Critical Damping Ratio (Normal Direction) (ball-wall) [-]	0,8
Critical Damping Ratio (Shear Direction) (ball-wall) [-]	0,8
Parameters for **Particles** (Balls)	
Normal Stiffness [kN/m^2]	$1*10^6$
Shear Stiffness [kN/m^2]	$1*10^6$
Contact Bond (Normal Direction) [kN]	-
Contact Bond (Shear Direction) [kN]	-
Material Density [kg/m^3]	2700
Friction Coeff. (ball-ball) [-]	tan 60° = 1,732
Critical Damping Ratio (Normal Direction) (ball-ball) [-]	0,5
Critical Damping Ratio (Shear Direction) (ball-ball) [-]	0,5

An overview of the best fit parameters is also presented below in Table 5.3.

Table 5.3 Overview of the best fit parameters (POISEL, PREH, & KOÇ, 2007)

Parameter	Description	Detachment Area	Glacial deposits	Glacier	Outcropping Rock	Particle interaction
φ [°]	friction angle	40	60	15	45	60
u_{rr} [m]	rolling resistance	0,5	0,4	0,6	0,4	-
β_n[-]	critical damping ratio, normal direction	0,8	0,8	0,8	0,8	0,5
β_s[-]	critical damping ratio, shear direction	0,8	0,8	0,8	0,8	0,5

5.4.3 Results and Interpretations

The position of the particles after 25.000 and 50.000 computation steps and their final position agree with the documented rock avalanche spreading. (See Figure 5.13 and 5.14)

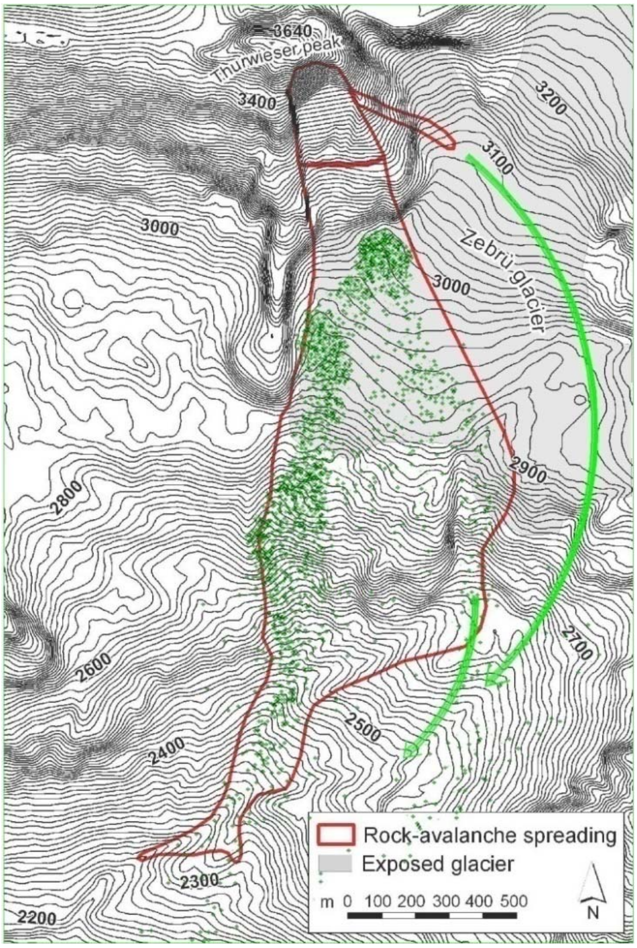

Figure 5.13 Particle postions after 63 secs (25.000 steps)

The numerical analyses showed that a small rock portion fell in east direction, which coincides with the actual rockslide. The run out distance of this portion was much too large than the actual situation, which is indicated with the long green arrow in Figure 5.13. Presumably the roughness of the glacier in this area due to crevasses caused the blocks to stop at 3.100 m above see level (POISEL, PREH, & KOÇ, 2007).

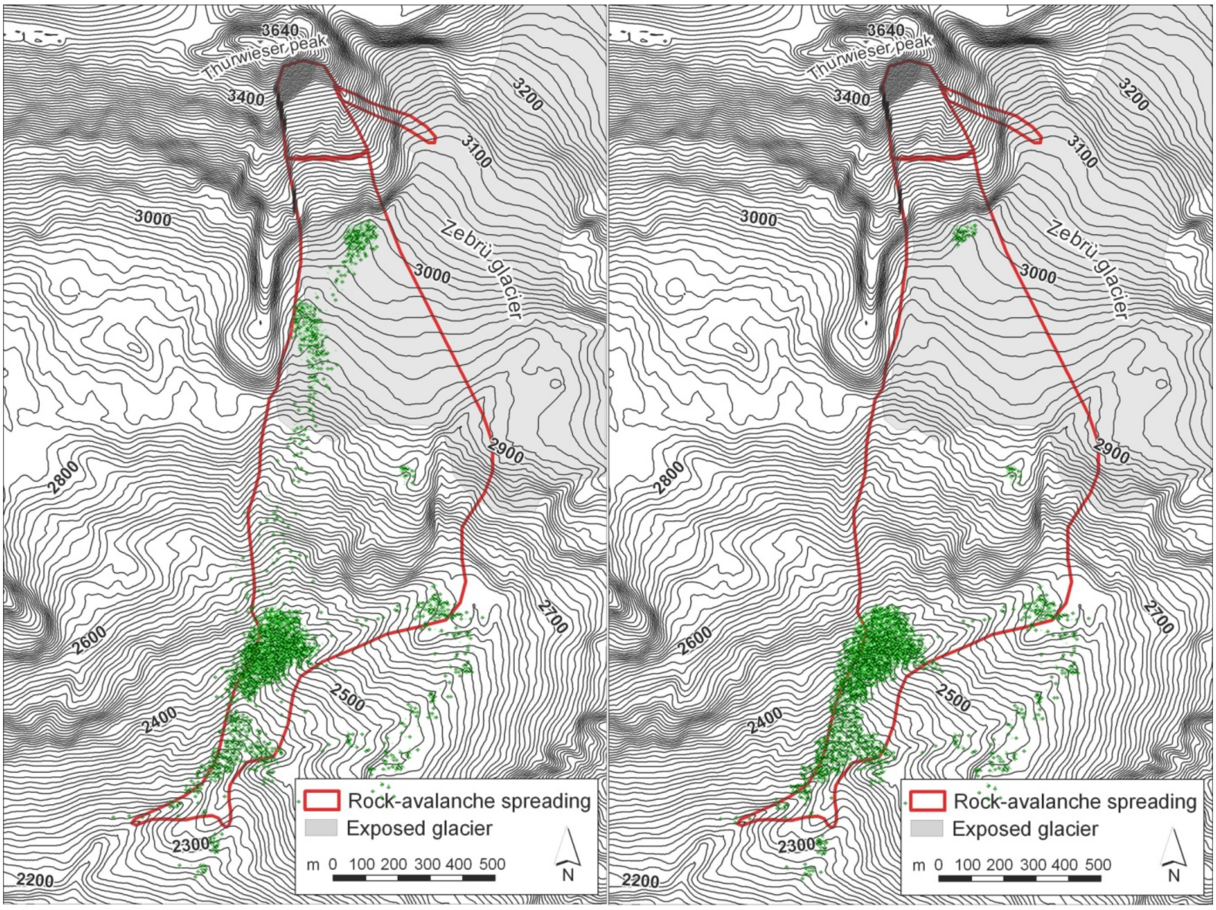

Figure 5.14 Particle positions after 124 seconds (50.000 timesteps, left) and after complete stoppage at 555 seconds (225.000 timesteps, right)

The final particle position and also deposit thickness agree fairly well with the real values (See Figure 5.15). Nevertheless an exact terrain surface model, which means a finer grid of wall elements, would have brought an even better coincidence with the observed rock avalanche. This is also true for the particles running out of the chute in the south-east of outcropping rock area (short arrow in Figure 5.13) (POISEL, PREH, & KOÇ, 2007).

Figure 5.16 and 5.17 show the particle positions at the relevant simulated timesteps.

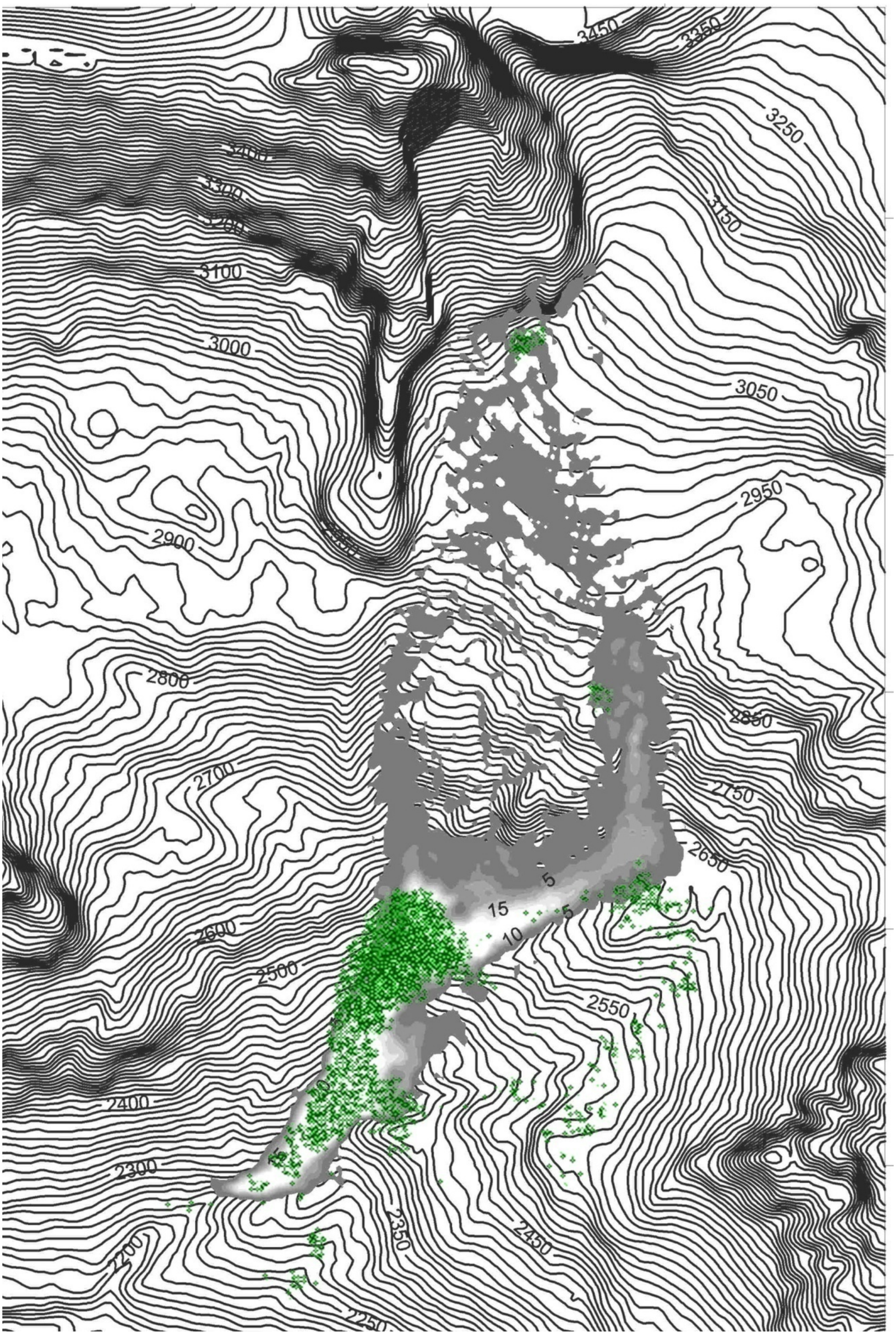

Figure 5.15 Particle positions after stoppage and thickness of the deposit in reality

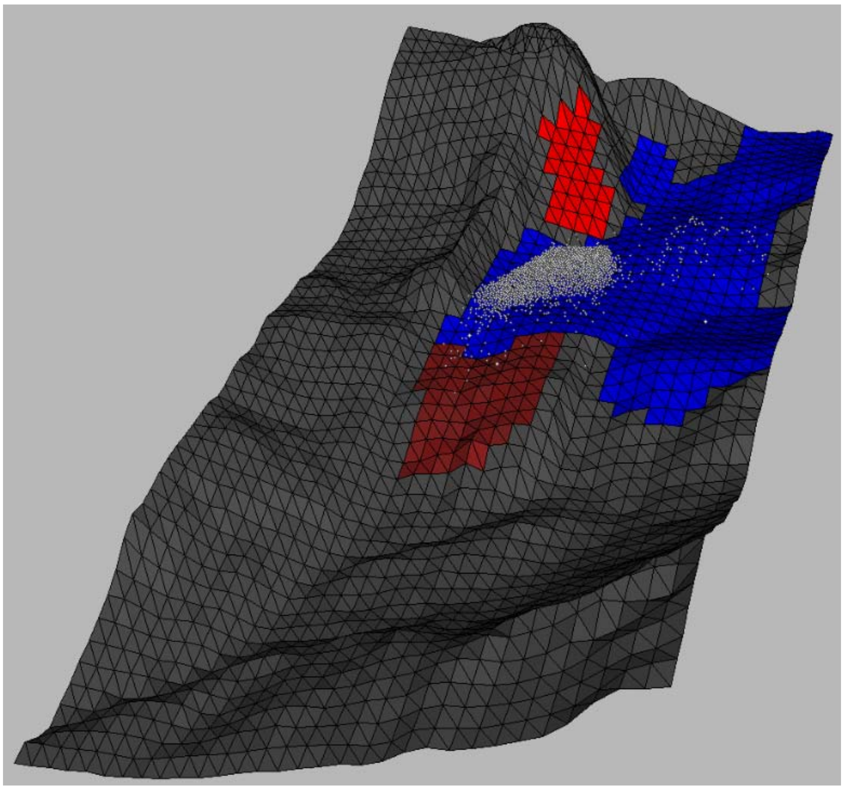

Figure 5.16 Particle positions after 30 seconds

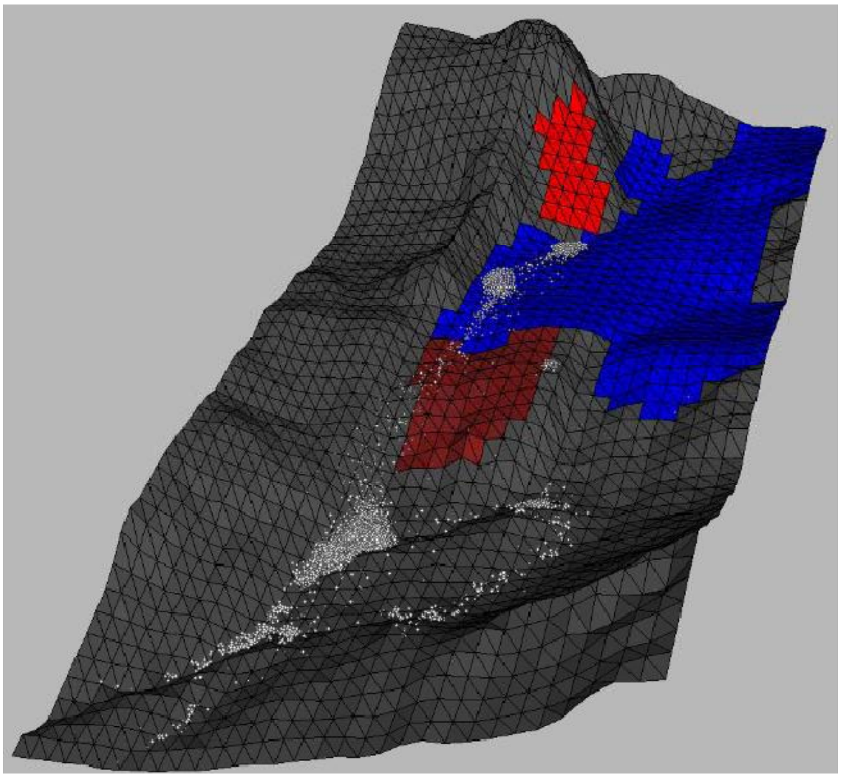

Figure 5.17 Particle positions after 100 seconds

5.4.3.1 Velocity and Kinetic Energy Diagrams

As mentioned above the velocity (Figure 5.18) and energy (Figure 5.19) diagrams reveal the actual behavior of the detached rock mass (See chapter 4.3).

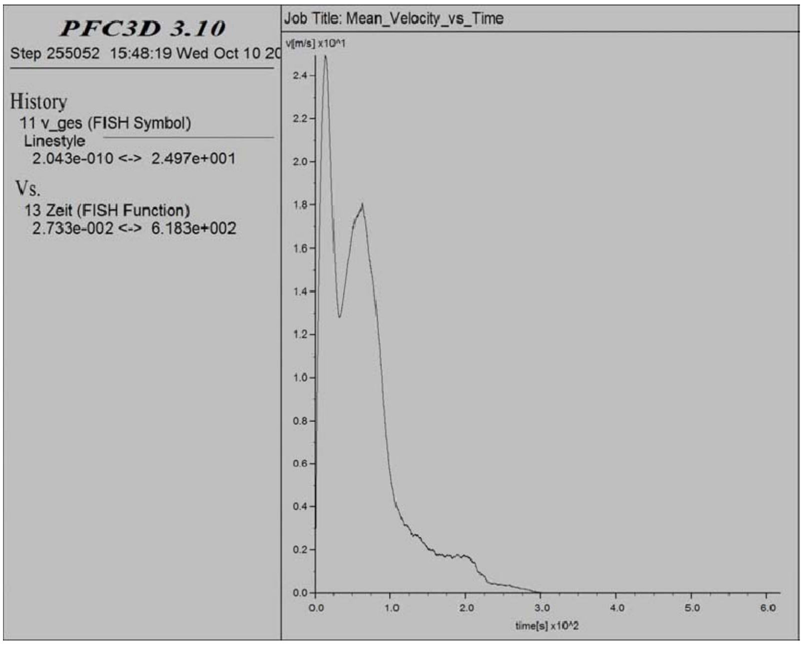

Figure 5.18 Mean particle velocity [m/s] over time [s]

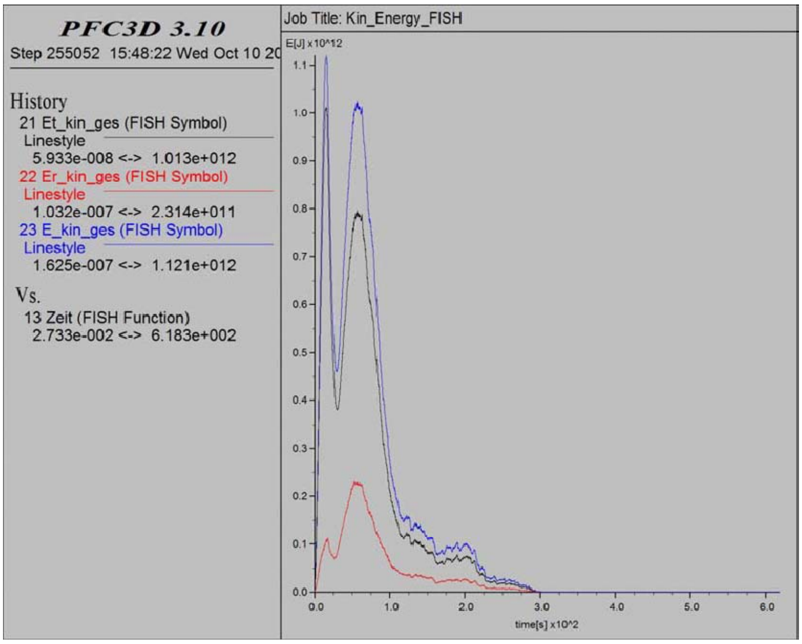

Figure 5.19 Rotational kinetic energy (red line), translational kinetic energy (black line), total kinetic energy (blue line) [J] over time [s]

After 30 seconds (Figure 5.16) the particle velocity and kinetic energy reach a minimum value just after all the particles leave the detachment area and move along the glacier. After 100 seconds the maximum travel distance of the rock avalanche is reached and after that only internal movements occur before the mass comes to final rest (See Figure 5.17) (POISEL, PREH, & KOÇ, 2007).

The kinetic energy diagram indicates that the motion of the Thurwieser Rock Avalanche is a pure rolling motion. As in chapter 1.2.1.3, equation 1.6 shown, pure rolling motions are comprised of a certain percentage of rotational (2/7) and translational (5/7) kinetic energy. This phenomenon can be observed in the Thurwieser case. Figure 5.20 show that the kinetic energy of the particles at different timesteps (15, 30, 63 and 125 sec) has a ratio of translational to rotational energy as in pure rolling phenomenon.

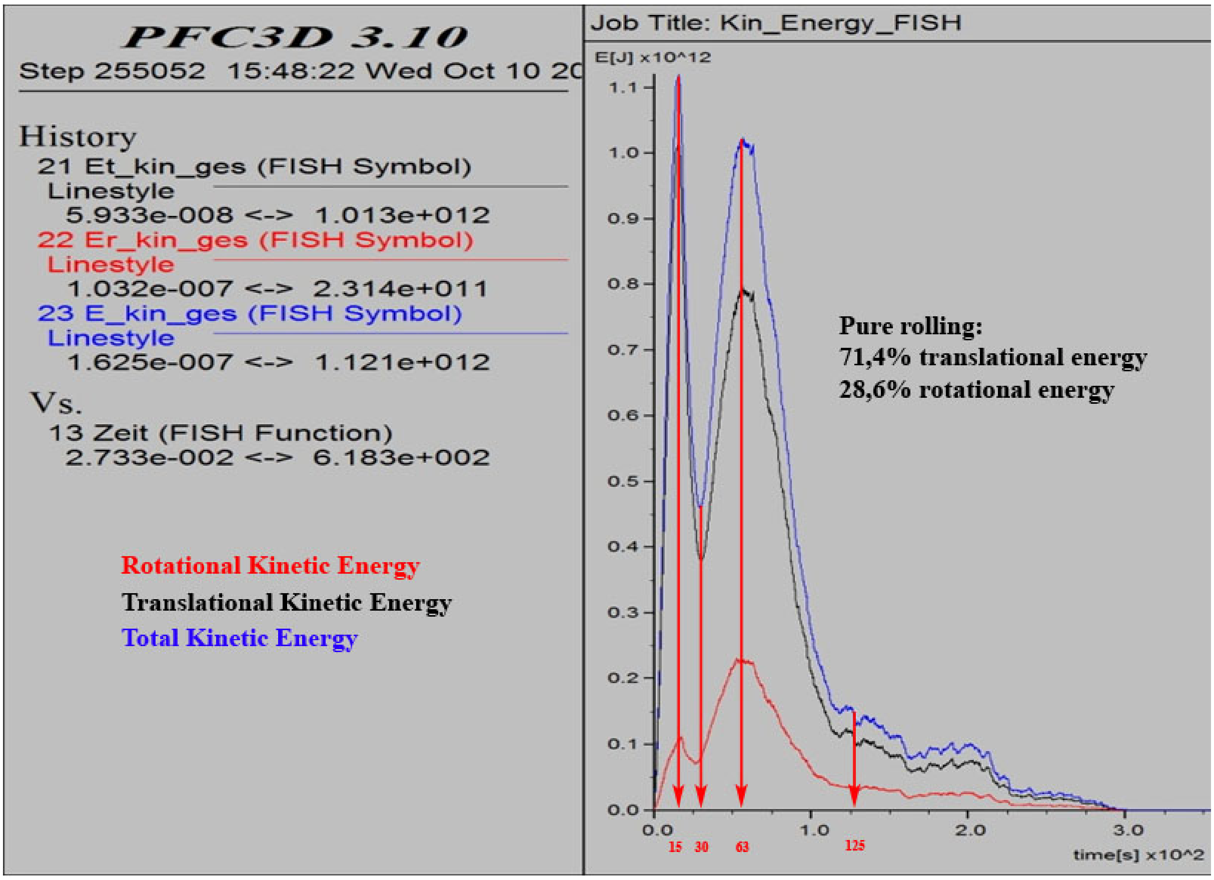

Figure 5.20 Kinetic energy at several simulation timesteps (15, 30, 63 and 125 sec), red line showing the rotational kinetic energy, black the translational kinetic energy and blue the total kinetic energy

The following figures (5.21 – 5.24) show the position of particles at the relevant timestep. These figures indicate the extreme kinetic energy values at the given timesteps (15, 30, 63 and 125 seconds) showing maxima und minima.

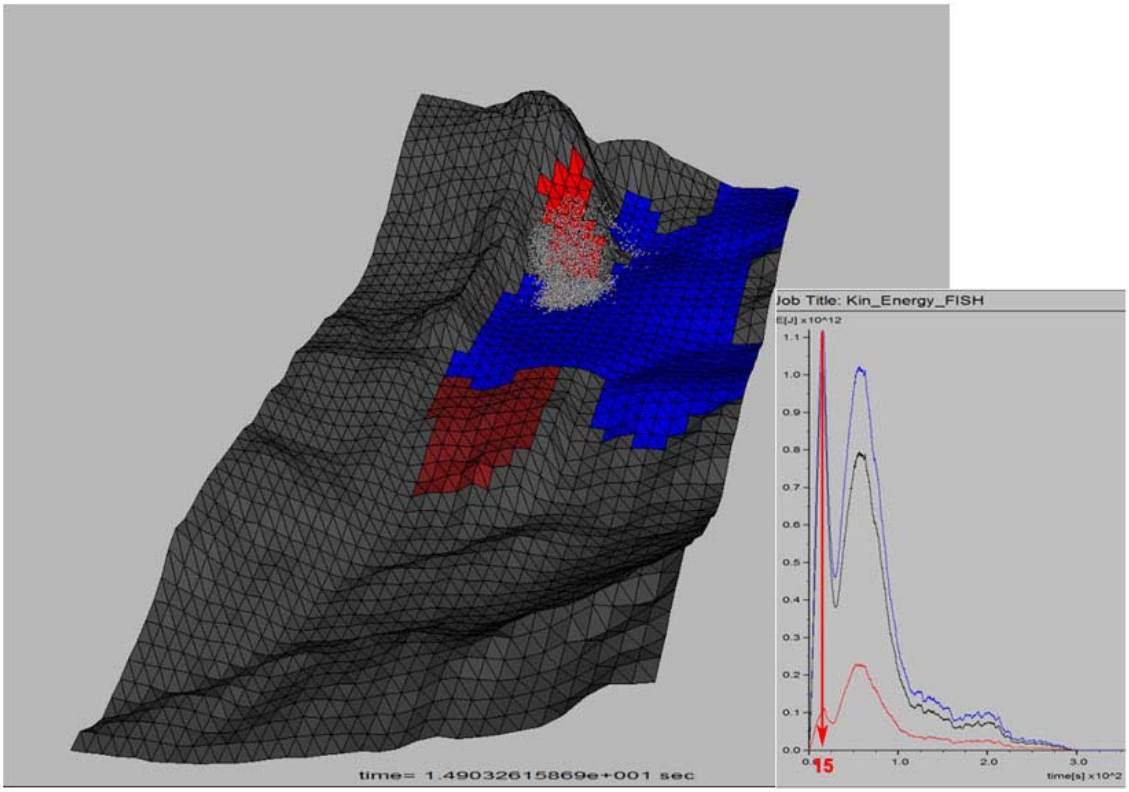

Figure 5.21 Particle position after 15 seconds (Complete detachment of the rock mass)

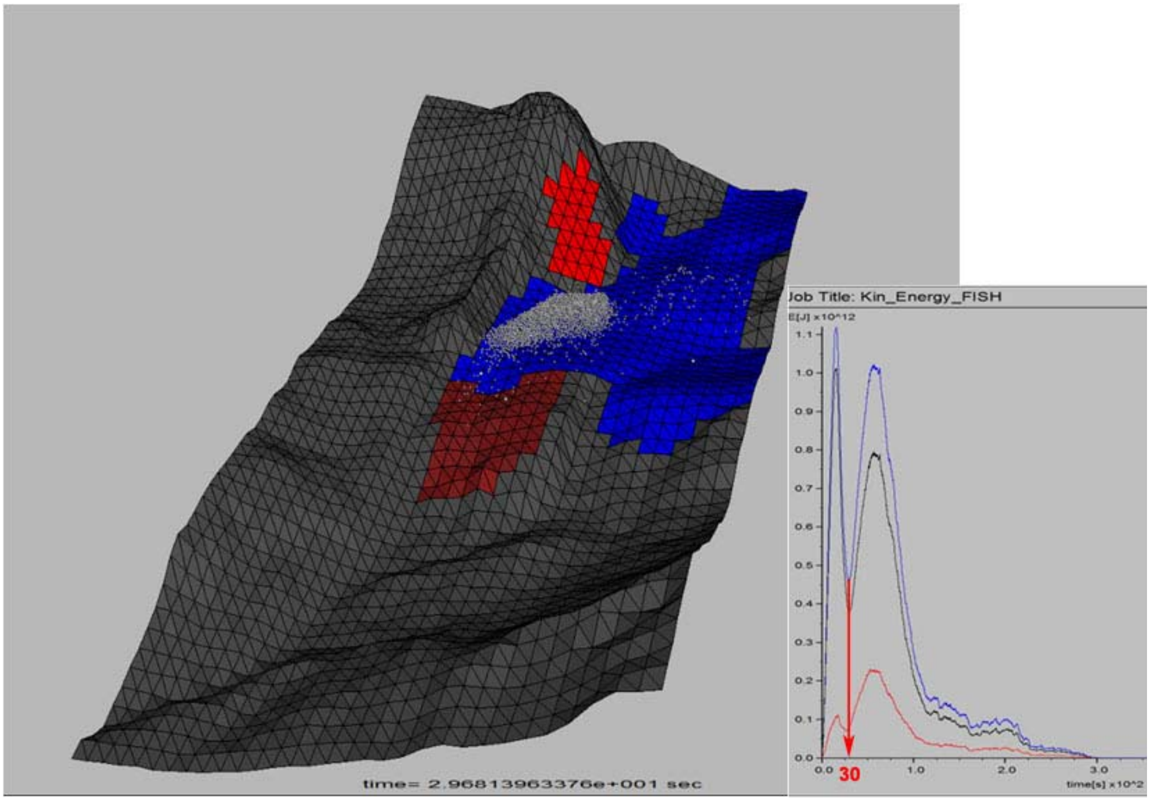

Figure 5.22 Particle position after 30 seconds (Rock mass over the glacier)

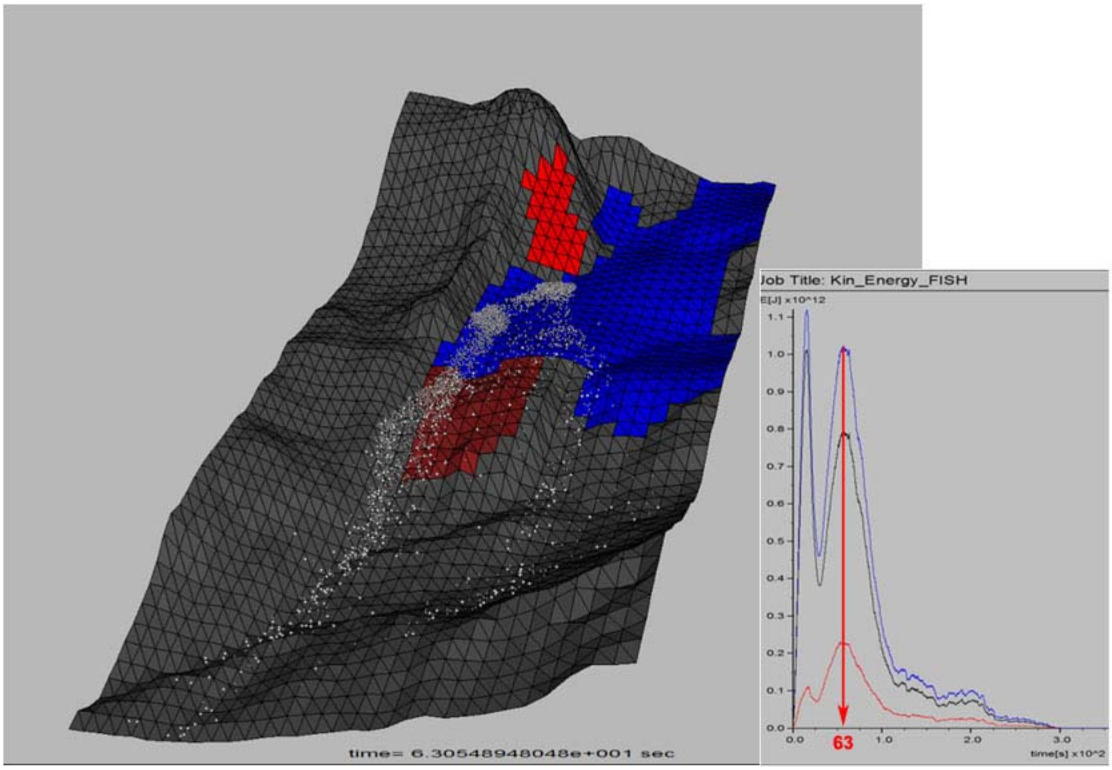

Figure 5.23 Particle position after 63 seconds

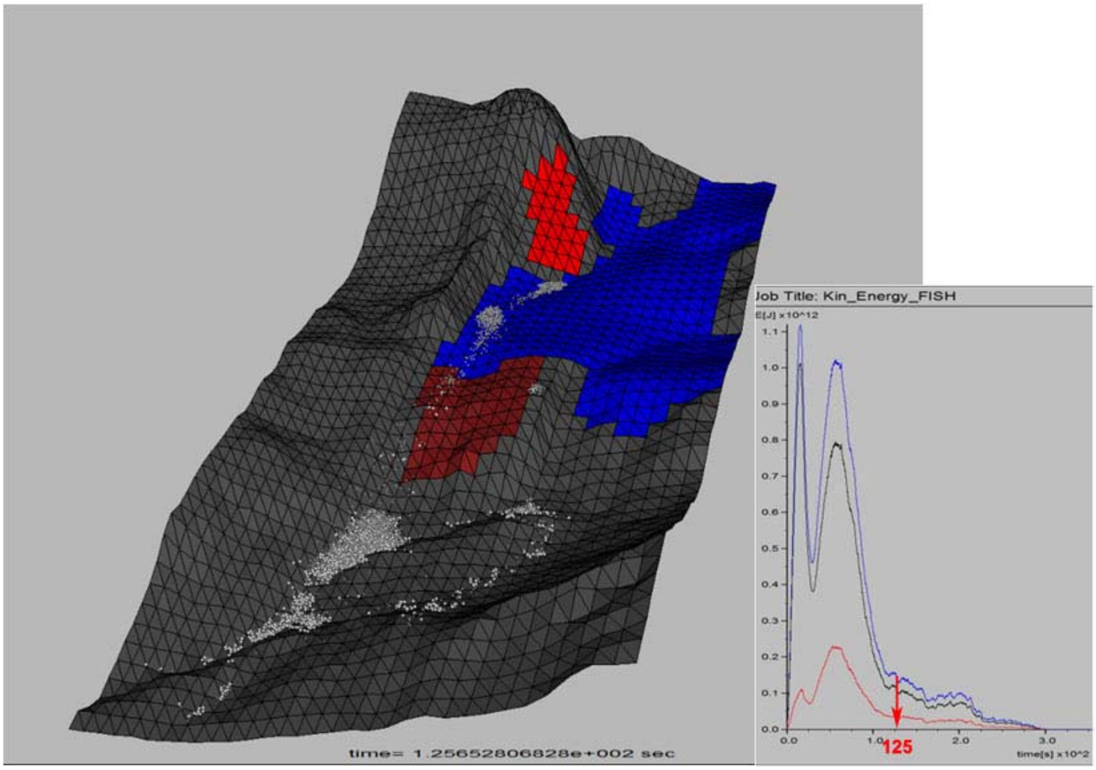

Figure 5.24 Particle position after 125 seconds

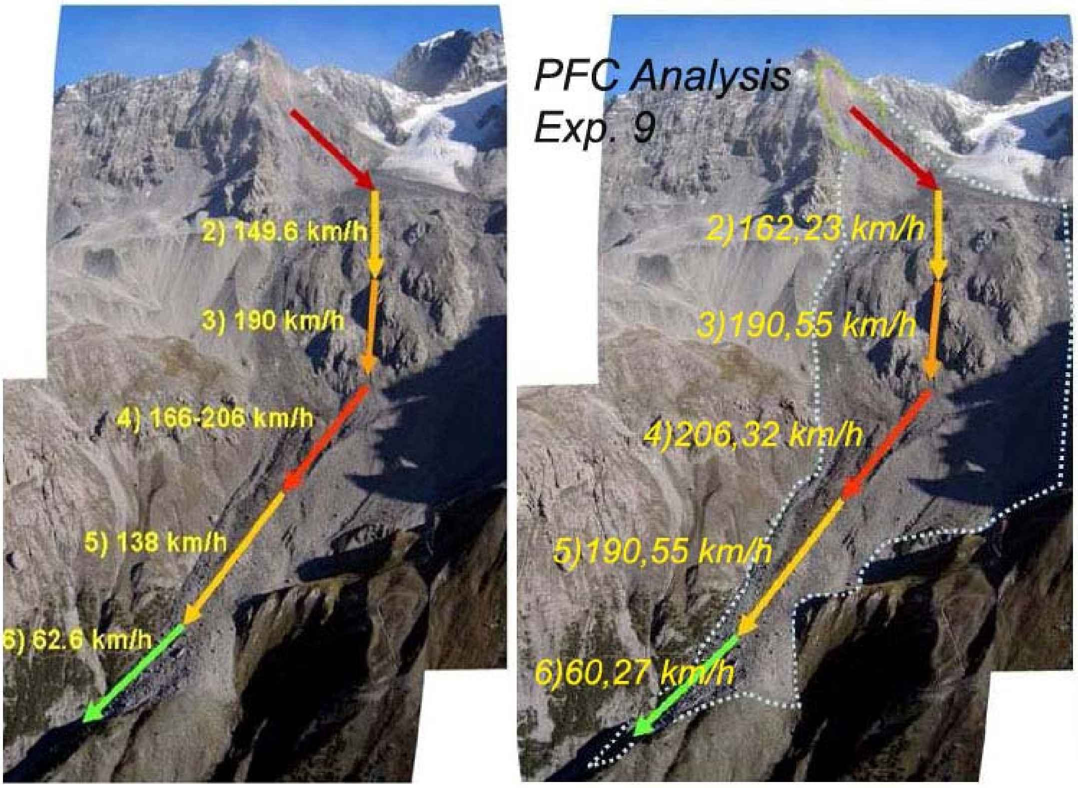

Figure 5.25 Front velocities; (left, observed velocities) (SOSSIO & CROSTA, 2007), (right, result of the simulation)

As seen in Figure 5.25, the calculated velocity vectors coincide with the observed velocity vectors digitally analyzed from the movie taken on the actual scene, fairly well.

6 Case 2: Frank Slide (Canada)

6.1 Introduction

The landslide from the east face of Turtle Mountain that destroyed the southern end of the town of Frank in the Crow's-nest Pass area of southwestern Alberta, Canada, has become a classic example of a mass movement because it is one of the largest landslides for which eyewitness accounts and a contemporary scientific examination exists (CRUDEN & KRAHN, 1978).

With a rock mass volume of $36.5 \times 10^6\ m^3$, Frank Slide was the deadliest landslide disaster of Canadian history, having destroyed not only a portion of the town of Frank, but also took the lives of 70 people with it (McCONNELL & BROCK, 1904). The landslide occurred on April 29, 1903, at 4:10 a.m. Frank, a coal mining town, was 21 km east of the border with British Columbia and 56 km north of the United States border in the Front Ranges of the Canadian Rockies. The present town of Frank is about 2 km north of the old town site.

Figure 6.1 Aerial view of the Frank Slide from northeast

6.2 Geological Conditions, Morphological Characteristics and Geomechanical Interpretations

The structure of Turtle Mountain was described as a monocline of Paleozoic *limestones* dipping to the west at about 50°. The limestone which formed the north-trending ridge of the Blairmore Range, of which Turtle Mountain is a part, had been thrust eastwards over vertical Mesozoic sandstones, shales, and coals on the Turtle Mountain fault. The slide mass was reported to have moved eastwards down the dip of a set of strike joints perpendicular to bedding (CRUDEN & KRAHN, 1978).

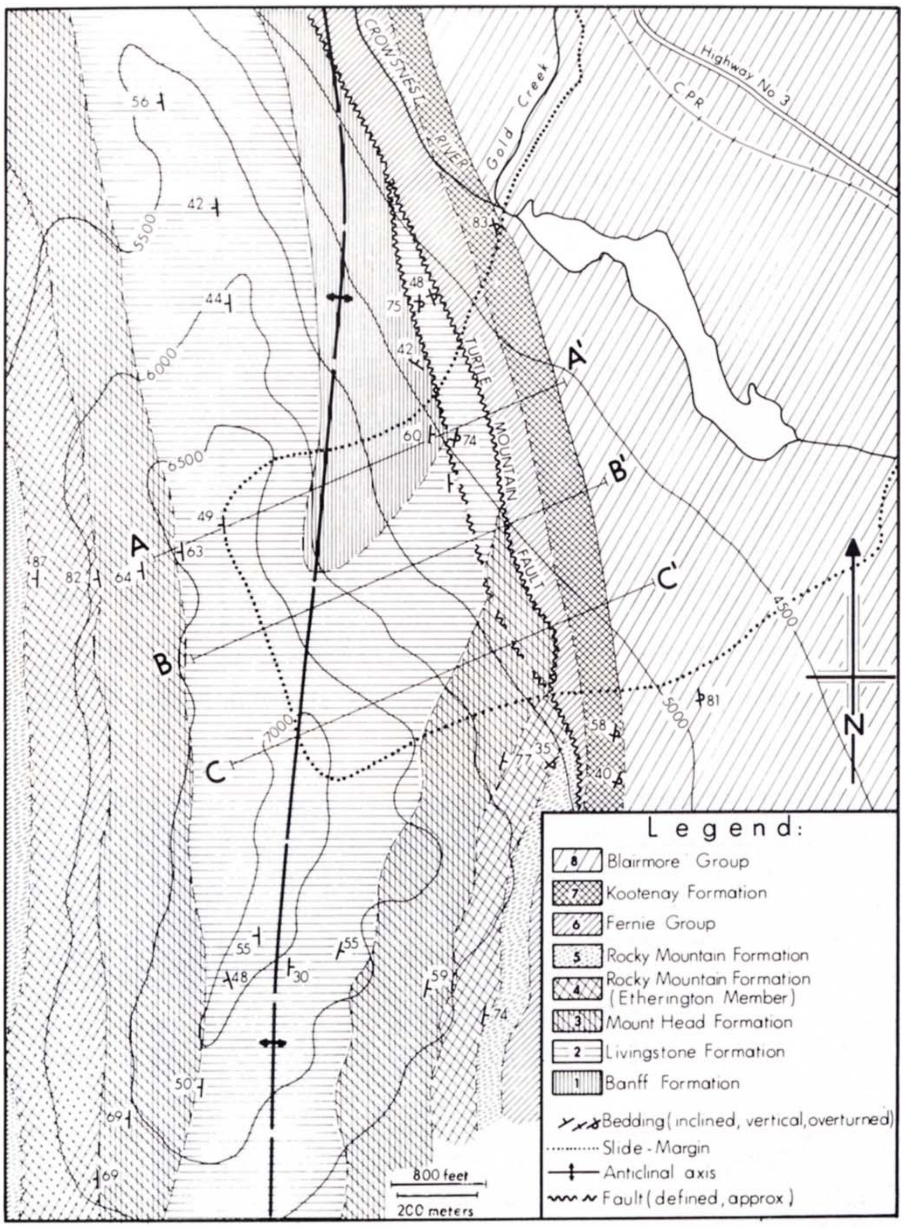

Figure 6.2 Bedrock geological map of the Turtle Mountain Area (CRUDEN & KRAHN, 1978)

The oldest rocks exposed on Turtle Mountain are Mississippian and belong to the Banff Formation. The uppermost 120 m of this formation crop out and are medium, crystalline, and shaly limestones containing many dark grey, pale brown weathering chert stringers. The basal bed of the overlying *Livingstone Formation* is 7.5 m thick, and consists of coarse-grained medium to dark grey limestone with a little chert. Above this are about 92 m of massive, grey, crystalline limestones with interbeds of argillaceous and cherty limestone. The uppermost beds of the *Livingstone Formation*, which is about 336 m thick here, are dark grey crystalline dolomitic limestones (CRUDEN & KRAHN, 1978).

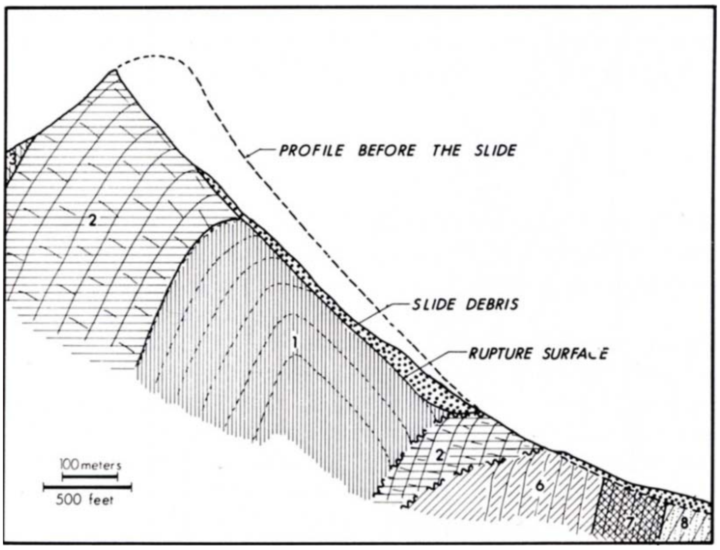

Figure 6.3 Cross-section through Turtle Mountain along line A-A' shown in Figure 6.2 (CRUDEN & KRAHN, 1978)

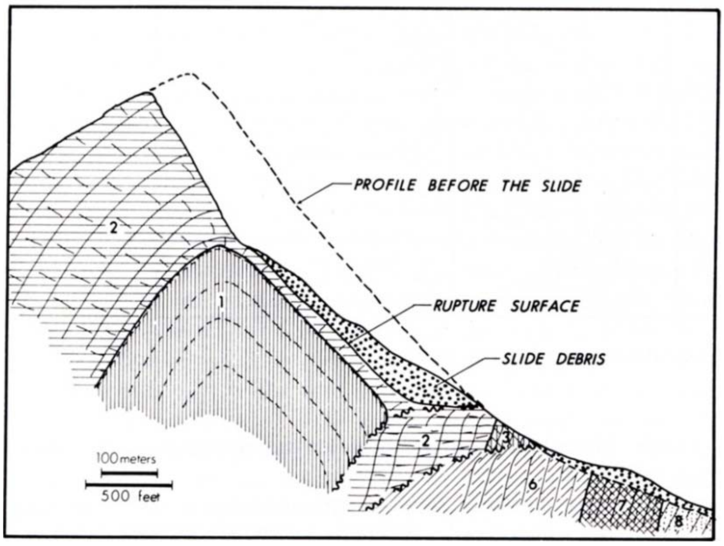

Figure 6.4 Cross-section along line B-B' shown in Figure 6.2 (CRUDEN & KRAHN, 1978)

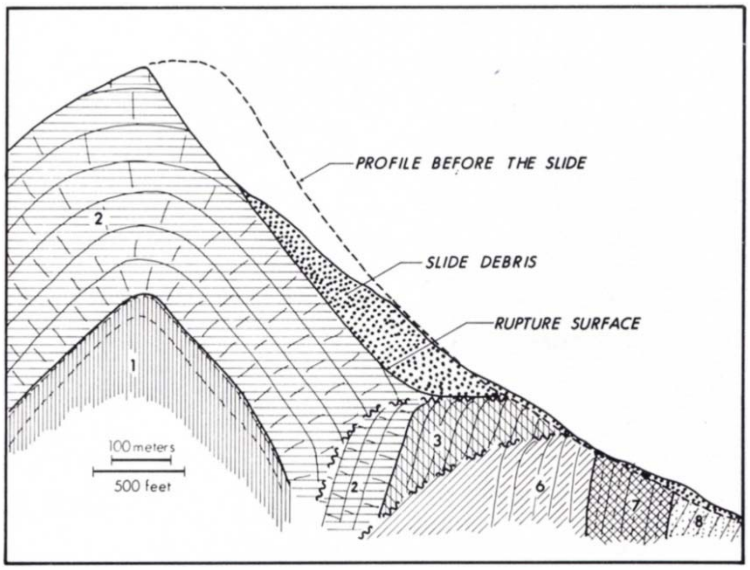

Figure 6.5 Cross-section along line C-C’ shown in Figure 6.2 (CRUDEN & KRAHN, 1978)

Figure 6.2 is a geological map of the vicinity of the slide based on CRUDEN &KRAHN (1978) detailed mapping in the summers of 1971 and 1972. Figures 6.3 – 6.5 show the relevant cross-sectional details on Figure 6.2. As clearly interpreted from the above plan view of the vicinity, the detached area lies mainly on *Livingstone Formation*, which consists of limestone. (For legends of Figures 6.3 – 6.5 see Figure 6.2)

The disturbed rock mass at the top of Turtle Mountain is not suitable for a detailed survey of the rock fabric, but according to CRUDEN &KRAHN (1978) the main elements of the fabric are obvious; two joint sets, both perpendicular to bedding, are developed, one parallel to the strike of the beds and the other parallel to their dip.

6.3 Model Setup

As explained in Case 1 (Thurwieser), the Frank Slide case included also two phases of simulation modeling, namely:

1. The modeling of the non-moved bed rock surfaces
2. The modeling of the detached rock mass

6.3.1 Modeling of the Surface

As in the Thurwieser Case, the committee of International Landslide Forum provided three digitalized elevation data files, namely: DEM path Frank Slide Surface (Surface elevation data without detached mass elevations), DEM source Frank Slide Solid Rock (Surface elevation plus detached rock mass elevations), DEM source Frank Slide Expanded Rock (Surface elevation plus detached rock mass elevation in fragmented and loose condition, for details see chapter 5.3.1)

Based on these raster coordinates a digitalized field was constructed using AUTODESK LAND DESKTOP 3 (See Figure 6.6).

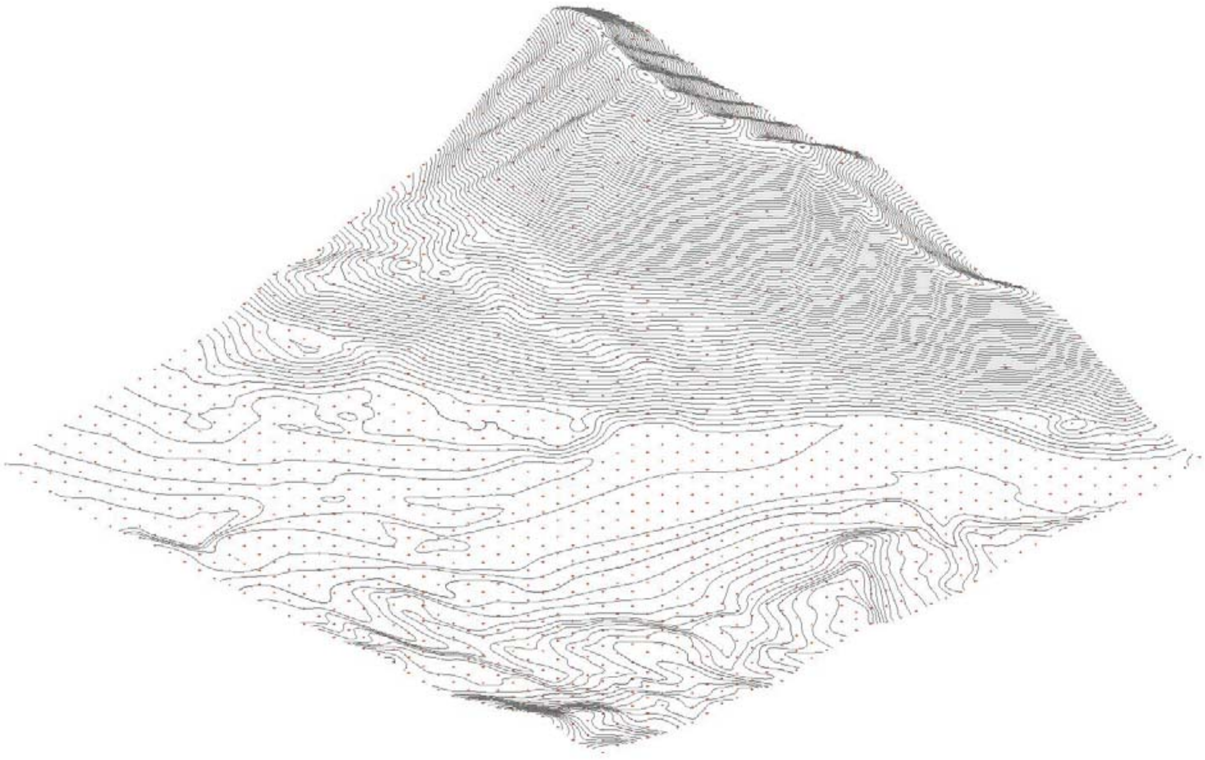

Figure 6.6 Axonometric view of the rockslide area with 10 m contour lines and the red marked raster points (100 x 100 m)

Unlike Thurwieser case, in Frank Slide a *100 x 100 m* raster had been chosen. Due to the *4000 x 4000 m* model area of the Frank Slide, it was aimed to reduce the time span of the total simulation run out. The probable reason for a slow simulation speed was the huge.

In Frank Slide only two regions had to be introduced (Figure 6.7 and 6.8):

1. The detachment area
2. Normal terrain (Non moved bed rock surface)

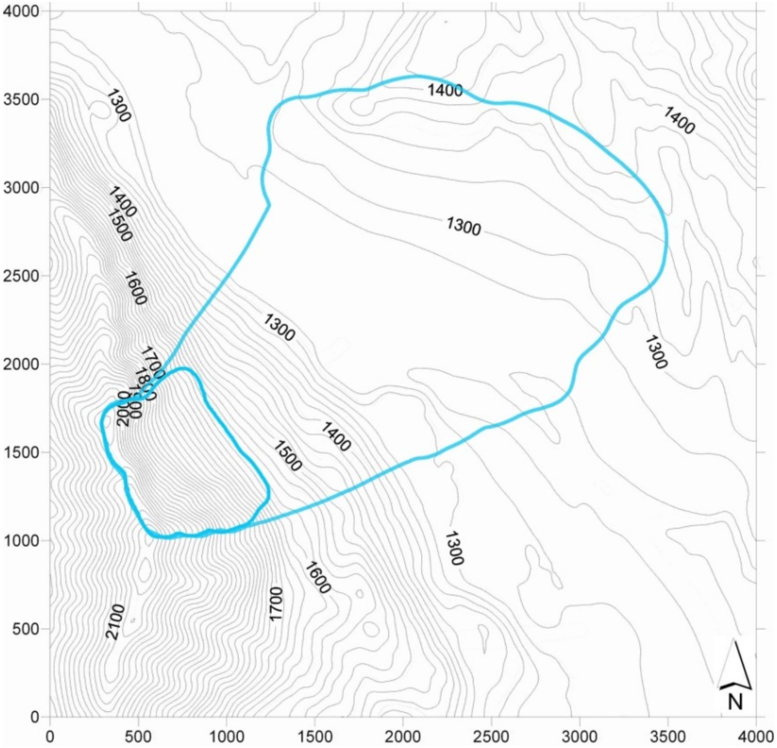

Figure 6.7 The outline of the run out path and source area of the detached rock mass (LANDSLIDE FORUM, 2007)

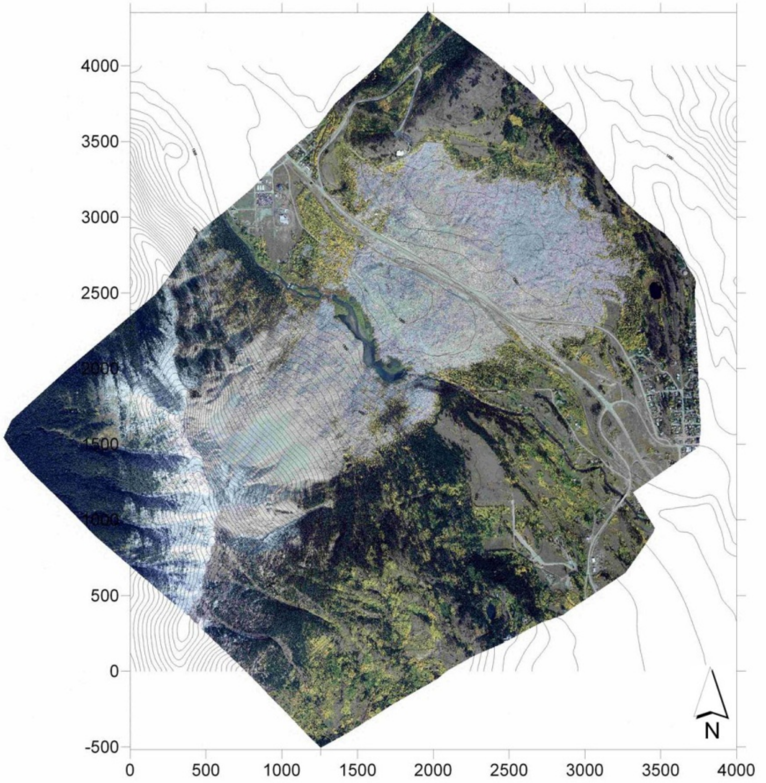

Figure 6.8 Aerial photo of the Frank Slide and the run out area (LANDSLIDE FORUM, 2007)

As a conclusion in surface modeling, the raster points from digitalized model was written in a text document, so that it could be possible later for *PFC* to generate a terrain model based on these raster points. The terrain model generated by *PFC* is demonstrated in Figure 6.9, where blue indicates normal terrain area (surface) and red, the detachment area.

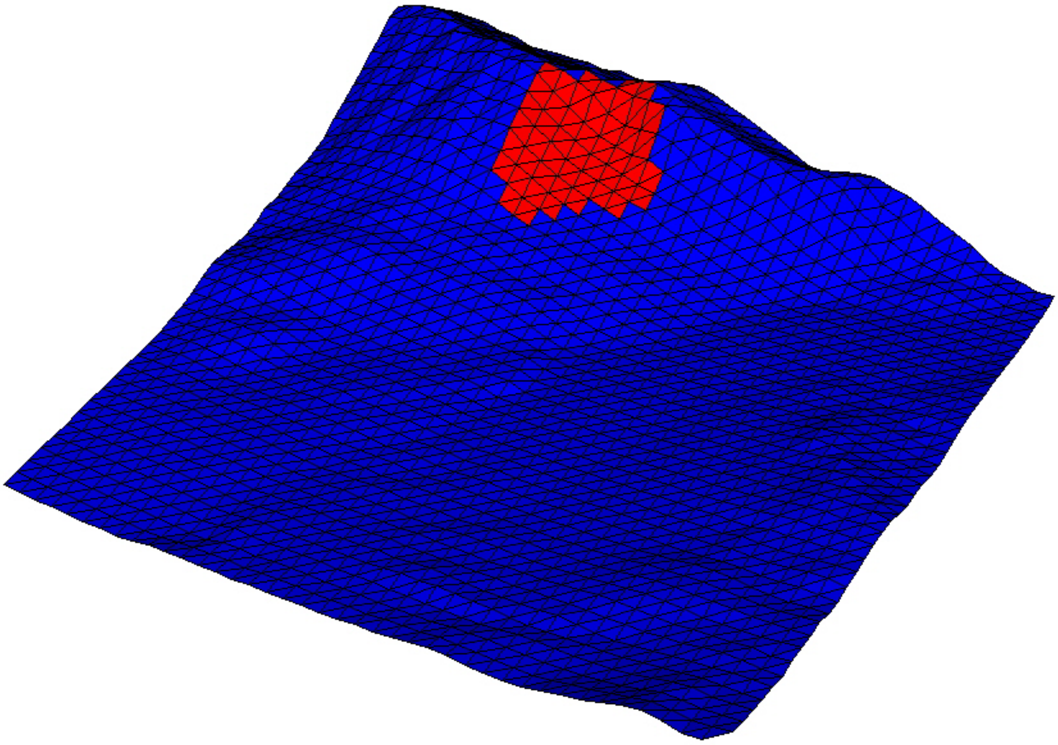

Figure 6.9 Southwest view of the *PFC* model, red indicating the detachment area and blue the normal terrain (surface)

6.3.2 Modeling of the Detached Rock Mass

The generation of the detached particles and also the build up of the surface model were carried out by *PFC*, as in the Thurwieser case. Firstly the points which were read from DEM file and rearranged as a 100 m raster, were prepared as an input file for *PFC* program. After the reading of these points by *PFC*, the program built up triangulated wall elements. The triangulation was done by a *FISH* routine, which was previously designed by PREH (2004). The allocation of the rockslide and surface parameters (e.g. rolling resistance, friction and damping coefficients) were carried out after the particle generation of the detached area.

The generation of the particles to simulate the detached rock mass was carried out just as in the Thurwieser case, so a lid-like cover element was introduced to the model in order to enable the particle generation.

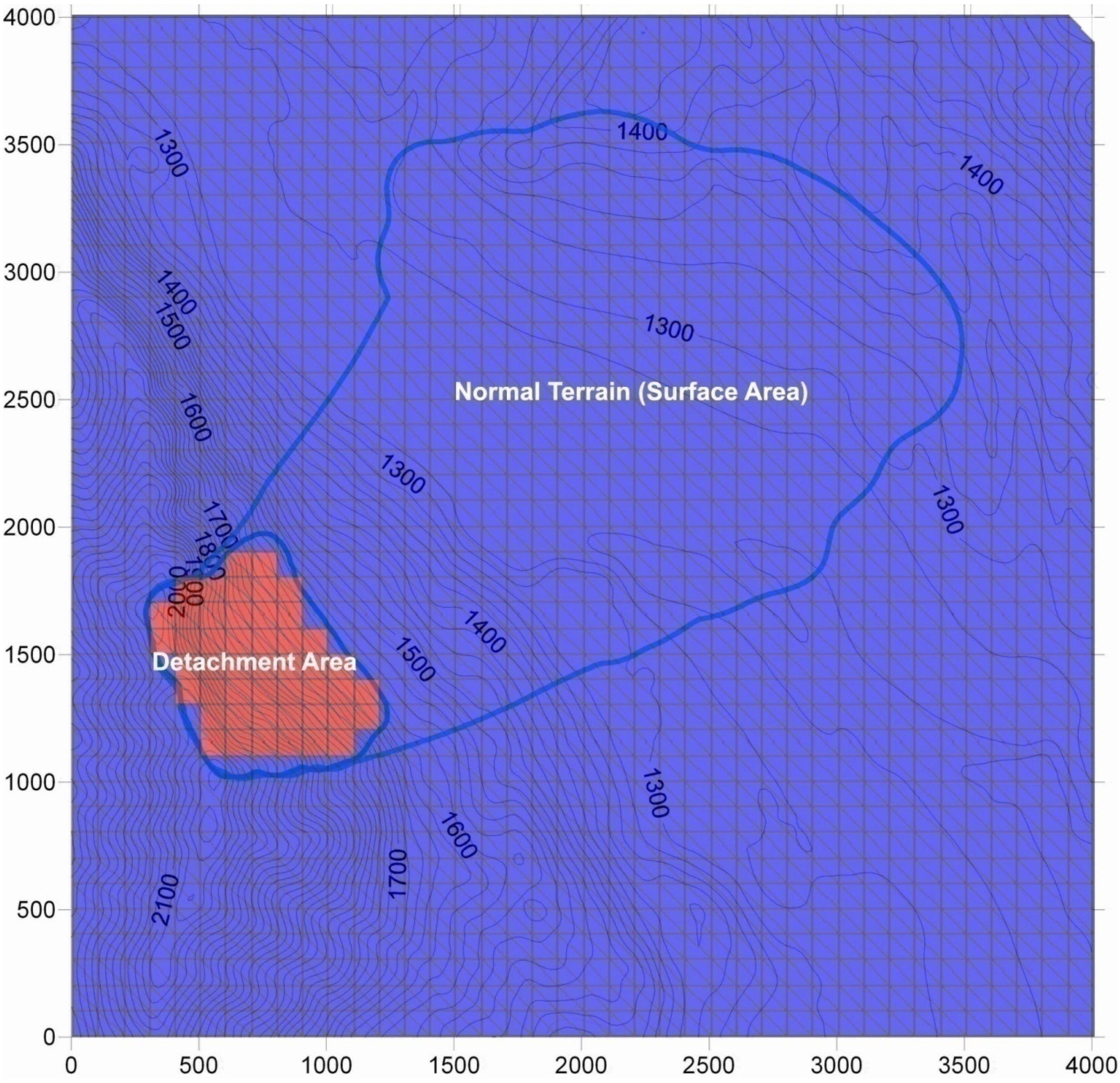

Figure 6.10 The different Frank Slide regions rendered over the path map of the rockslide provided by the Landslide Committee

Further details were carried out just as in the Thurwieser case (see chapter 5.3.2). Figure 5.8 and 5.9 show the flowchart of the particle generation, the construction of the surface model and the simulation of the run out.

6.4 Run out Modeling

The terrain was generated by 3,372 wall elements, simulating both the detachment area and the terrain itself. The detached limestone rock was modeled by 19,691 particles (balls) with random generated balls radius length ranging between $r_{min} = 10\ m$ and $r_{max} = 15\ m$. After starting the run out process by deleting the wall elements above the detached rock volume, 30,000 timesteps were calculated (POISEL, PREH, & KOÇ, 2007).

6.4.1 Initial Position

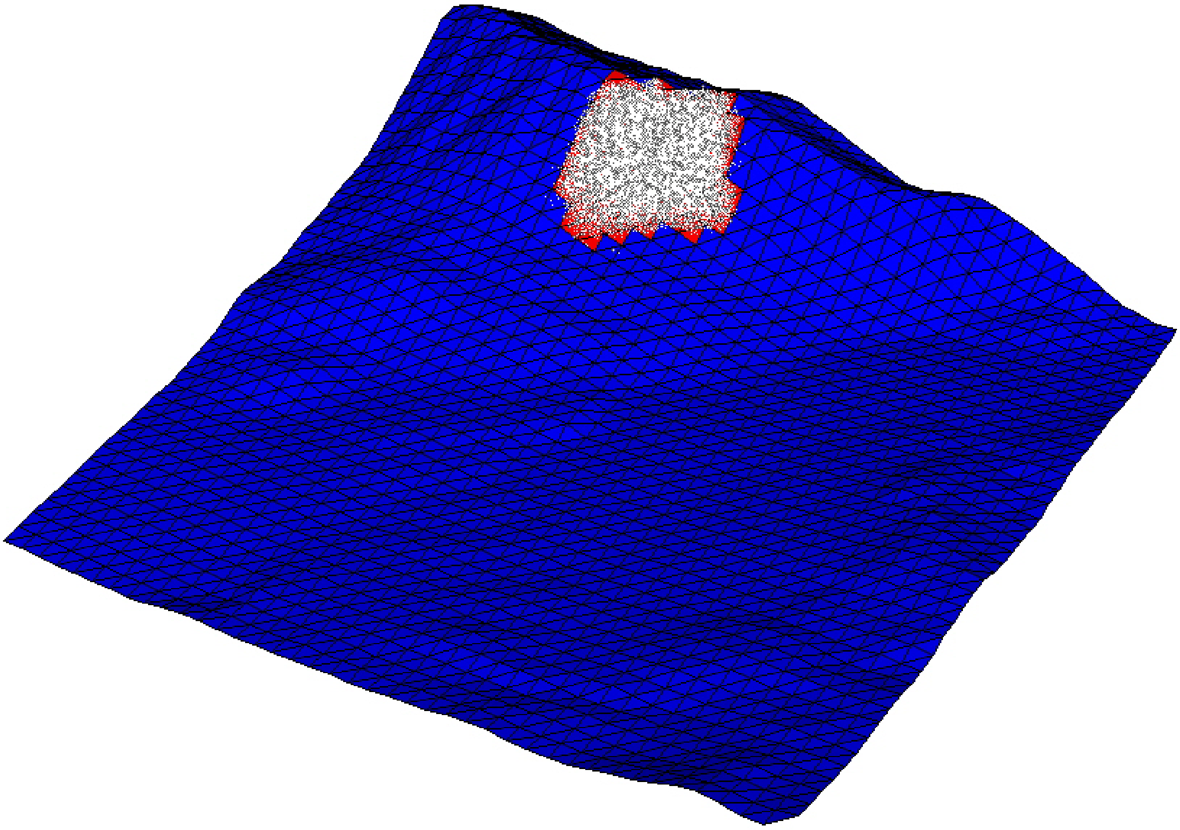

Figure 6.11 Frank Slide, three dimensional view of the initial position of the particles

Figure 6.11 illustrates the initial position of the generated particles over the detachment area.

6.4.2 Parameter Study

After the generation of the triangulated mesh a parameter study was conducted in order to achieve the assembly of the best fit variables of surface and particle interaction which would in turn reflect a reasonable run out of a rockslide. Achieving the best fit variables could only be managed by conducting several run out experiments, in which the parameters were redefined each time depending on the simulation results.

As in the Thurwieser case, the experiments were planned generally in two branches: the detached rock volume as loose material (Expanded Rock) and as solid material (Solid Rock) (See chapter 5.3.1). The experiments carried out on loose material (expanded rock) certainly provide more particles and consequently a run out simulation closer to the observations (height and depth distribution of the deposit) than the solid material would do, but it would eventually lead to a higher calculation time. On the other hand, experiments which were conducted on solid material (solid rock) would generate fewer particles but ensure a favorable computational time. Unlike Thurwieser case, in Frank Slide an additional branching in experiment chart was introduced to see whether it was necessary to generate fewer balls or a higher number of balls for an exact rockslide behavior. Therefore two kinds of detachment area were introduced to the program, namely: a small detachment area and a large detachment area. The chart below shows the experiment branches in detail with the relevant experiment numbers beneath.

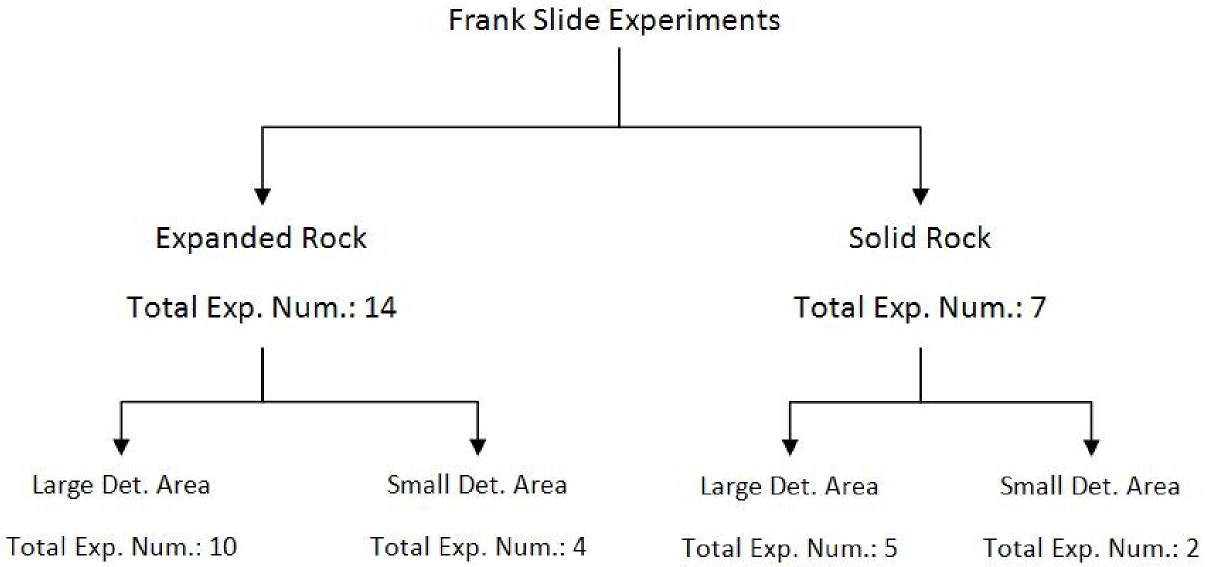

Figure 6.12 Types of experiments and the total number conducted

The simulation experiment conducted on Frank Slide with fragmented material (Expanded Rock) on large detachment area produced the best particle end positions within the given path region. The best fit parameters are stated in Table 6.1. A quick overview could be found in Table 6.2. Unlike Thurwieser, in Frank case the critical damping ratios were set to a normal value (0.5), because the results of the experiments did not show any anomalies of extreme bouncing motion like in the Thurwieser case.

Table 6.1 Best fit parameters for simulating Frank Slide

Frank Slide Exp. for Expanded Rock (Large Det. Area)	**Parameter**
Common Parameters for all Regions	
Number of Timesteps [-]	30.000
Volume [m^3]	$35*10^6$
Number of Wall Elements (Surface)	3.372
Number of Wall Elements (Cover)	172
Number of Particles (Balls)	19.691
Range of Ball Radius [m]	10,0 - 15,0
Porosity [%]	35
Parameters for Region "**Detachment Area**"	
Normal Stiffness [kN/m^2]	$1*10^6$
Shear Stiffness [kN/m^2]	$1*10^6$
Friction Coeff. (ball-wall) [-]	tan 15° = 0,268
Rolling Resistance [m]	0,05
Critical Damping Ratio (Normal Direction) (ball-wall) [-]	0,5
Critical Damping Ratio (Shear Direction) (ball-wall) [-]	0,5
Parameters for Region "**Normal Terrain (Surface)**"	
Normal Stiffness [kN/m^2]	$1*10^6$
Shear Stiffness [kN/m^2]	$1*10^6$
Friction Coeff. (ball-wall) [-]	tan 8° = 0,141
Rolling Resistance [m]	0,1
Critical Damping Ratio (Normal Direction) (ball-wall) [-]	0,5
Critical Damping Ratio (Shear Direction) (ball-wall) [-]	0,5
Parameters for **Particles (Balls)**	
Normal Stiffness [kN/m^2]	$1*10^6$
Shear Stiffness [kN/m^2]	$1*10^6$
Contact Bond (Normal Direction) [kN]	-
Contact Bond (Shear Direction) [kN]	-
Material Density [kg/m^3]	2700
Friction Coeff. (ball-ball) [-]	tan 30° = 0,577
Critical Damping Ratio (Normal Direction) (ball-ball) [-]	0,5
Critical Damping Ratio (Shear Direction) (ball-ball) [-]	0,5

Table 6.2 Overview of the best fit parameters (POISEL, PREH, & KOÇ, 2007)

Parameter	Description	Detachment Area	Normal Terrain (Surface)	Particle interaction
φ [°]	friction angle	15	8	30
u_{rr} [m]	rolling resistance	0,05	0,1	-
β_n[-]	critical damping ratio, normal direction	0,5	0,5	0,3
β_s[-]	critical damping ratio, shear direction	0,5	0,5	0,3

6.4.3 Results and Interpretations

The particle positions of the simulation showed clearly that the simulation coincided with the documented path and rockslide deposit. Picture shots from the numerical analysis were rendered over the aerial photo to demonstrate the simulation accuracy. Figure 6.13 shows the particle position after 25 seconds (5.800 timesteps), where the particles were colored in red to emphasize them on the rendered picture.

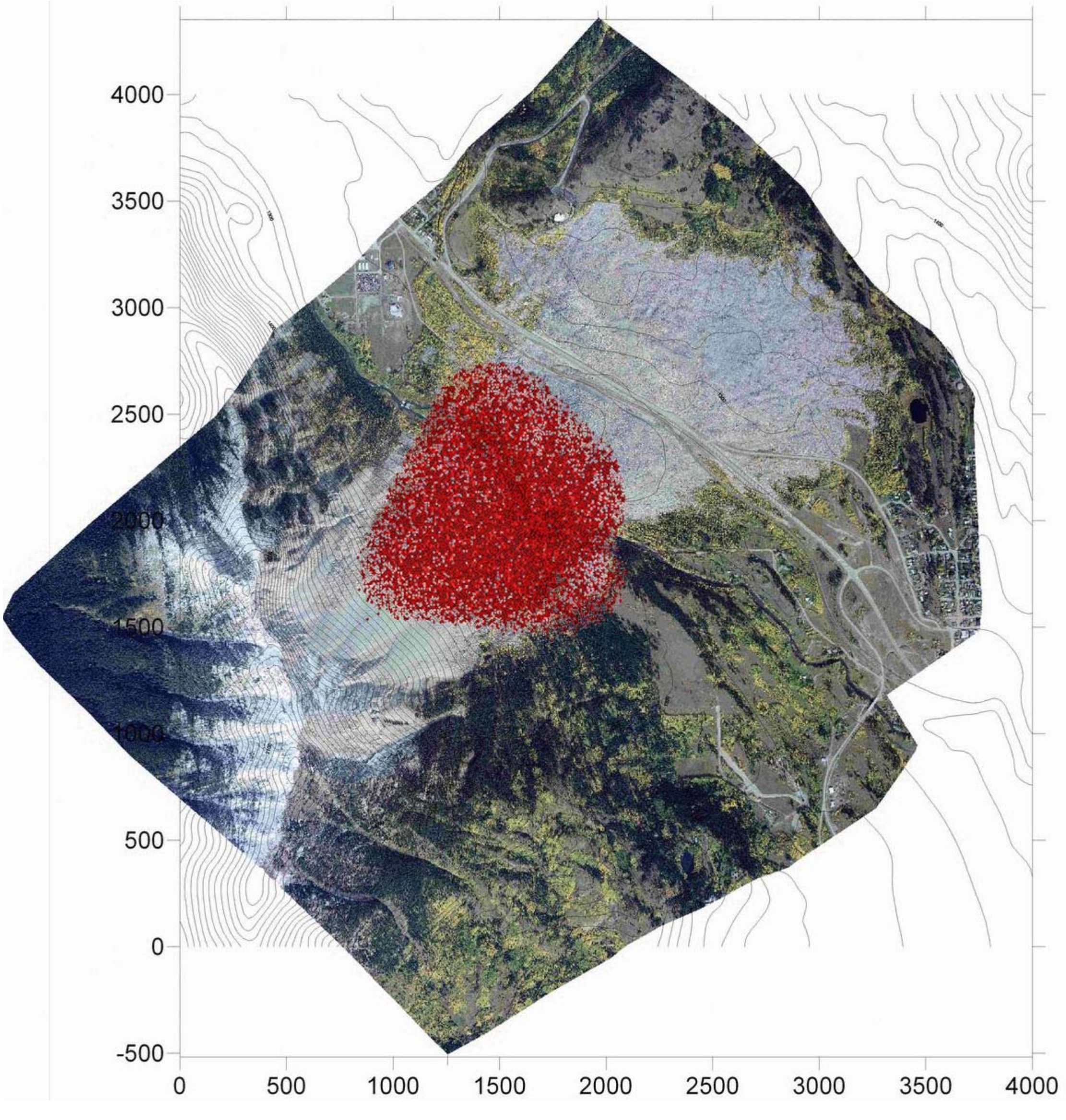

Figure 6.13 Particle positions after 25 seconds (5.800 steps)

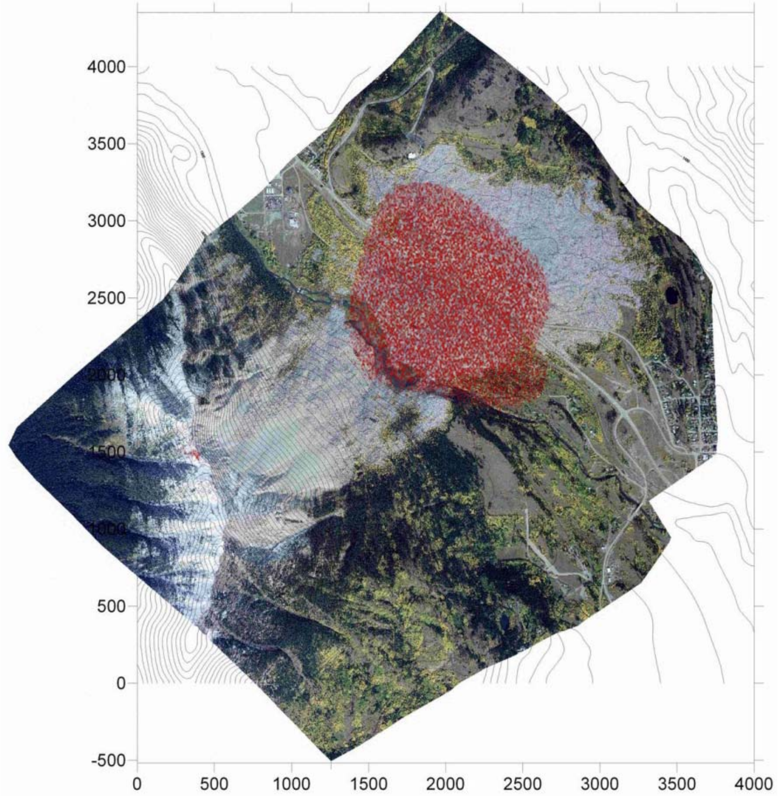

Figure 6.14 Particle positions after 36 seconds (10.000 steps)

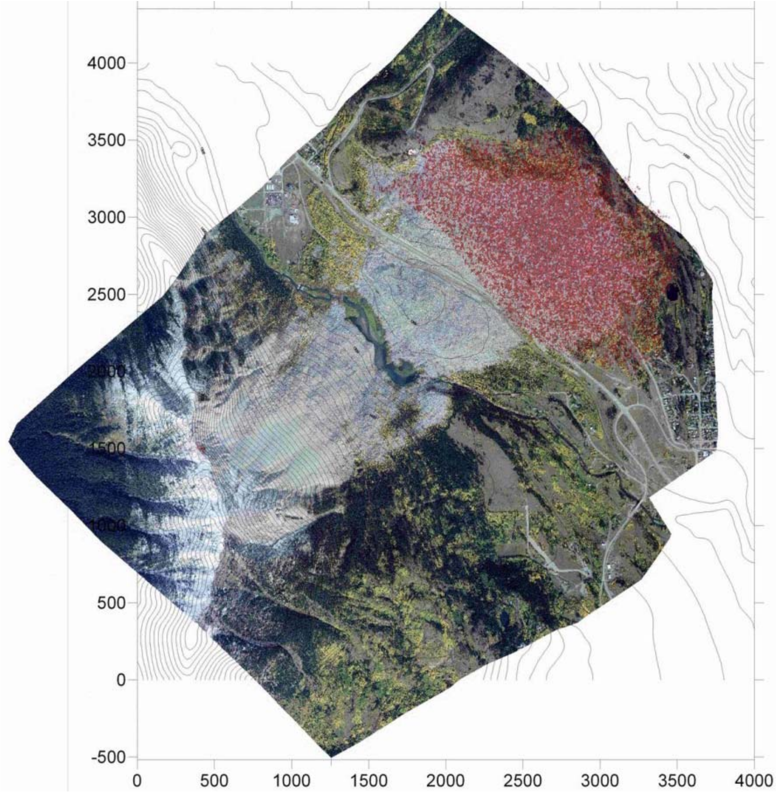

Figure 6.15 Particle positions after 65 seconds (15.000 steps)

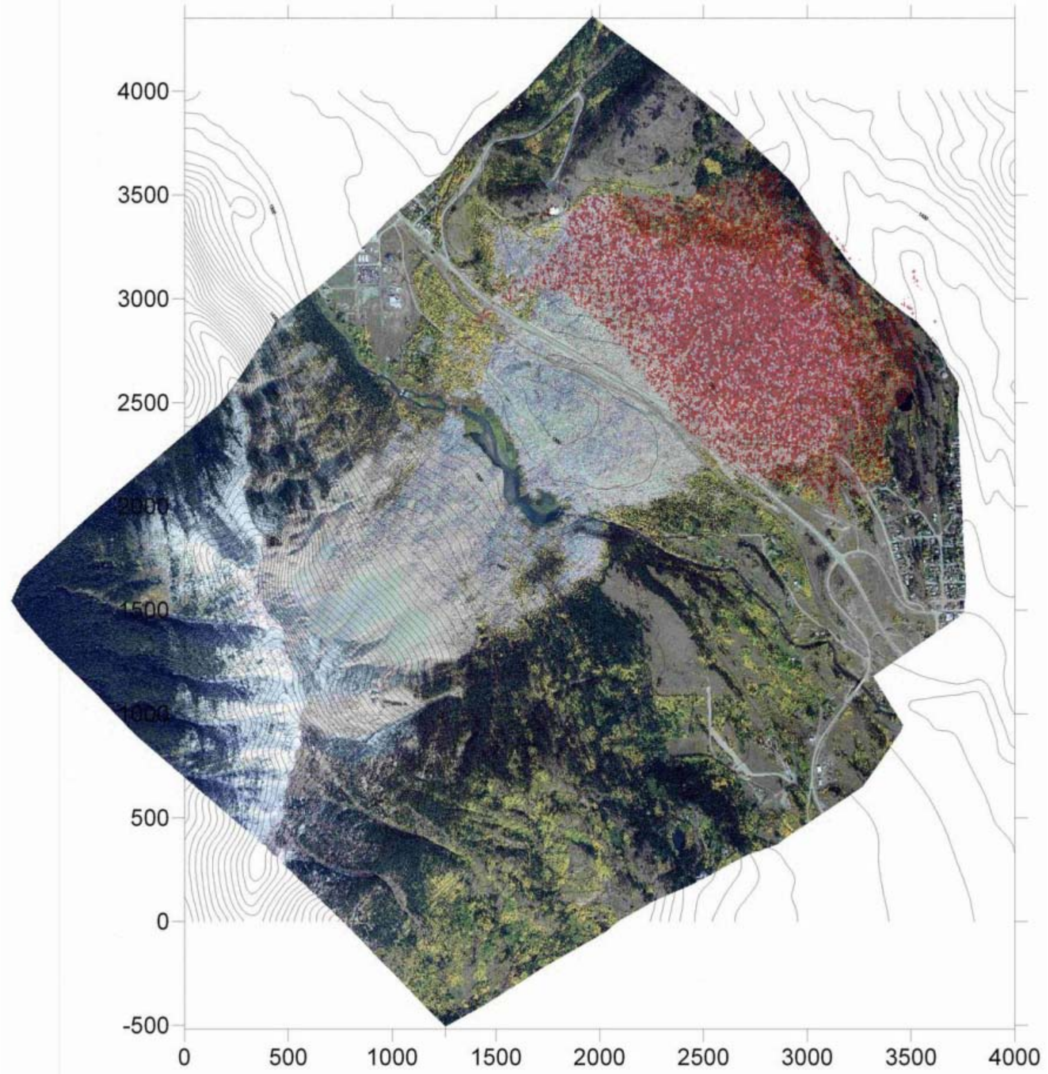

Figure 6.16 Final distribution of the particles

Figure 6.14 and 6.15 show the particle positions after 36 and 65 seconds. It was observed that after approximately 70 seconds the main particle motion came to an end. This coincided well with reality. After that time a backwards motion at the north side of the deposit occurred. It was assumed that this motion could be a cause of a ridge formation, which came originally from the DEM terrain but could not be noticed from the aerial photo. Therefore a slight deviation from the given deposit path occurred (POISEL, PREH, & KOÇ, 2007)

The final positions (Figure 6.16 and 6.17) of the particles in the PFC model show no particles at rest in the floodplain. This corresponds well with the observation in reality that only minor damming of the Crowsnest River (indicating that the landslide eroded some material from the floodplain) was observed after the landslide.

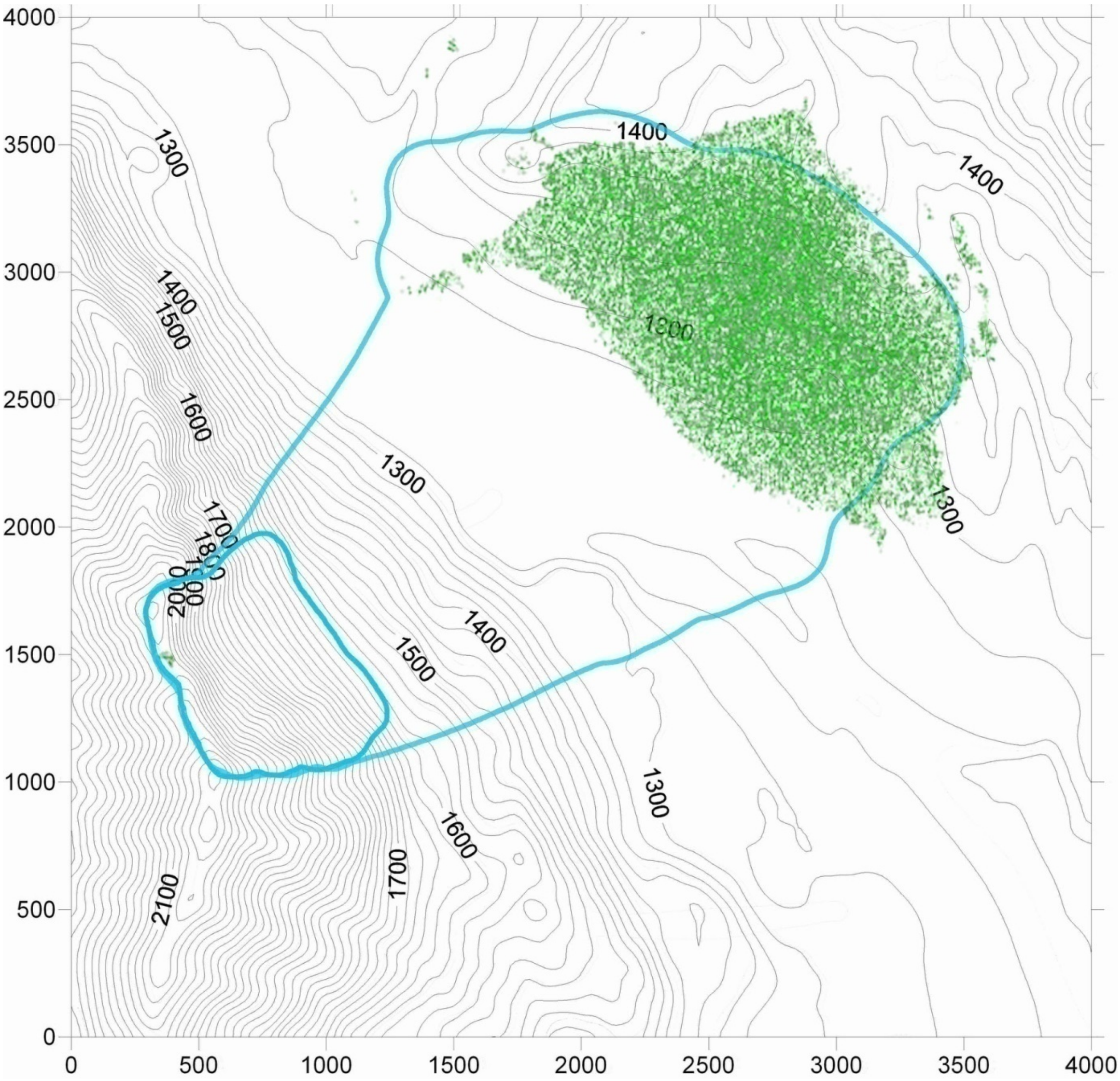

Figure 6.17 Final distribution of the particles rendered over the given run out path

6.4.3.1 Velocity and Energy Diagrams

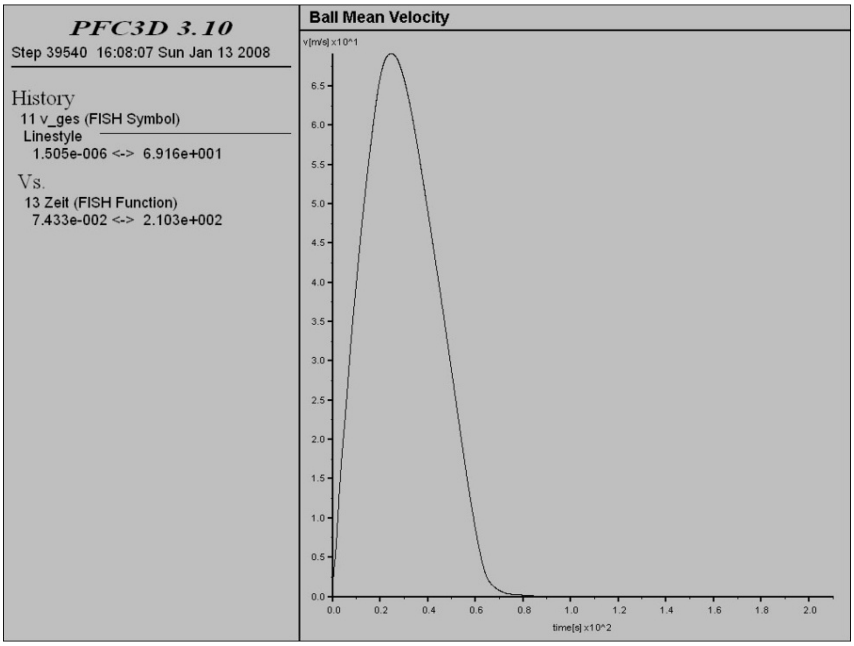

Figure 6.18 Mean particle velocity [m/s] over time [s]

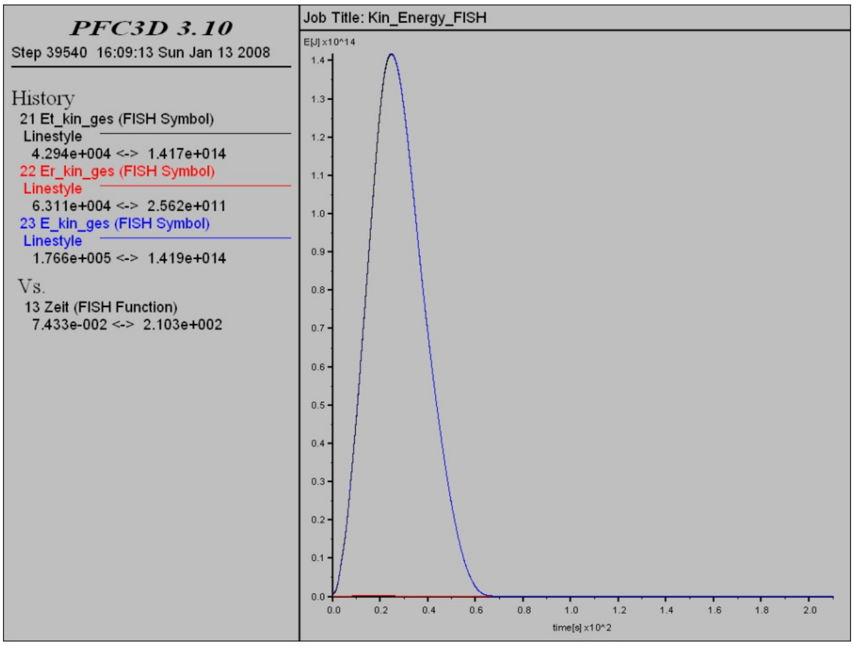

Figure 6.19 Rotational kinetic energy (red line), translational kinetic energy (black line), total kinetic energy (blue line) [J] over time [s]

The development of the mean particle velocity over time (Figure 6.18) and of kinetic energy over time (Figure 6.19) reveals that both reach a maximum value after 25 seconds. As in Figure 7.20 shown, the centre of gravity of the rockslide mass is passing through the river at that time. The small amount of rotational energy in kinetic energy figure also reveals that a coherent mass is sliding downslope (POISEL, PREH, & KOÇ, 2007)

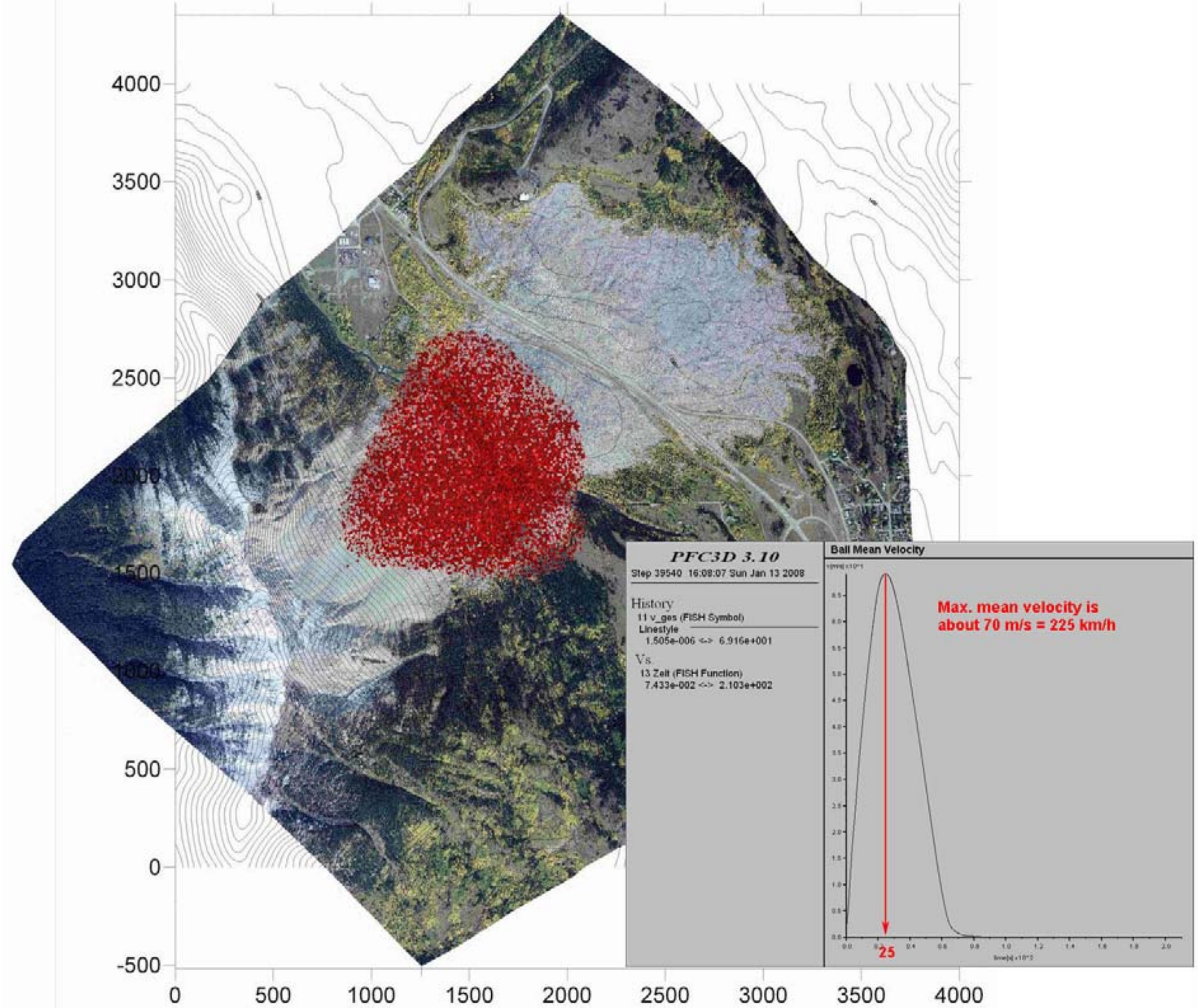

Figure 6.20 The position of particles at their maximum velocity

Happened due to the height of 18 m deposit and the particle size varying between 10 to 15 m, an inverse grading of the deposit observed in reality could not be identified from the *PFC* simulation (CRUDEN & KRAHN, 1978). But from the theoretical background and necessary adaptations, it is possible to deduce that *PFC* can produce an inverse grading as a natural outcome.

7 Comparison of the Cases

A comparison between the cases Thurwieser and Frank reveals:

1. The parameters necessary to achieve the best run out results are completely different (see Table 5.3 and Table 6.2). In the Thurwieser case the viscous damping parameters should have to be set to highest values (see Figure 3.12) to achieve a better run out behavior coinciding with natural rock avalanche phenomenon. On the other hand, in the Frank case a normal value of 0.5 meet the appropriate rockslide motion conditions. The other parameters are also set far away from each other for an appropriate solution.
2. The developments of the mean particle velocities as well as of kinetic energy are completely different (See Figure 5.19 and Figure 5.20). In the Thurwieser case there is an internal movement of particles, where in the Frank case there is no sign of any internal movement.
3. The kinetic energy histograms illustrate clearly that some 30 percent of kinetic energy goes to rotational energy in the Thurwieser case, whereas in Frank there is no indication of rotational energy.

From the above stated factors it can be deduced that the Frank Slide is a real “slide” of a coherent mass (CRUDEN & KRAHN, 1978) whilst Punta Thurwieser run out is a rock mass fall with much internal movement. Therefore the parameters for a run out simulation have to be adjusted in such a way that the simulation gives a rock mass fall in one particular case and a slide of a coherent mass in the corresponding to the real conditions (POISEL, PREH, & KOÇ, 2007).

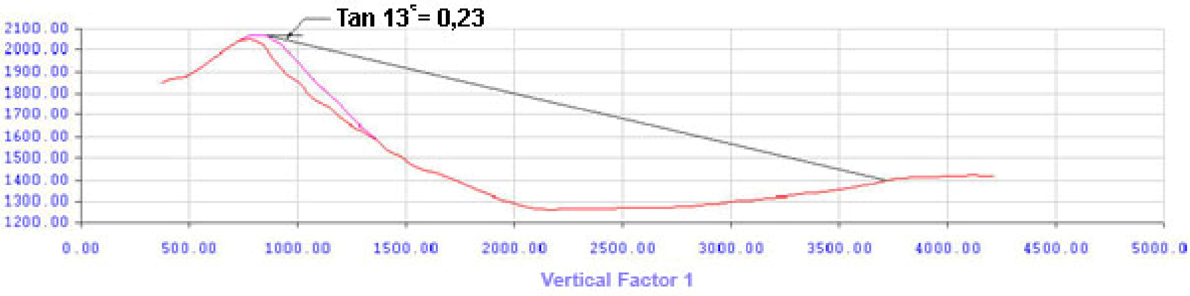

Figure 7.1 The Fahrböschung angle (13°) in Frank case

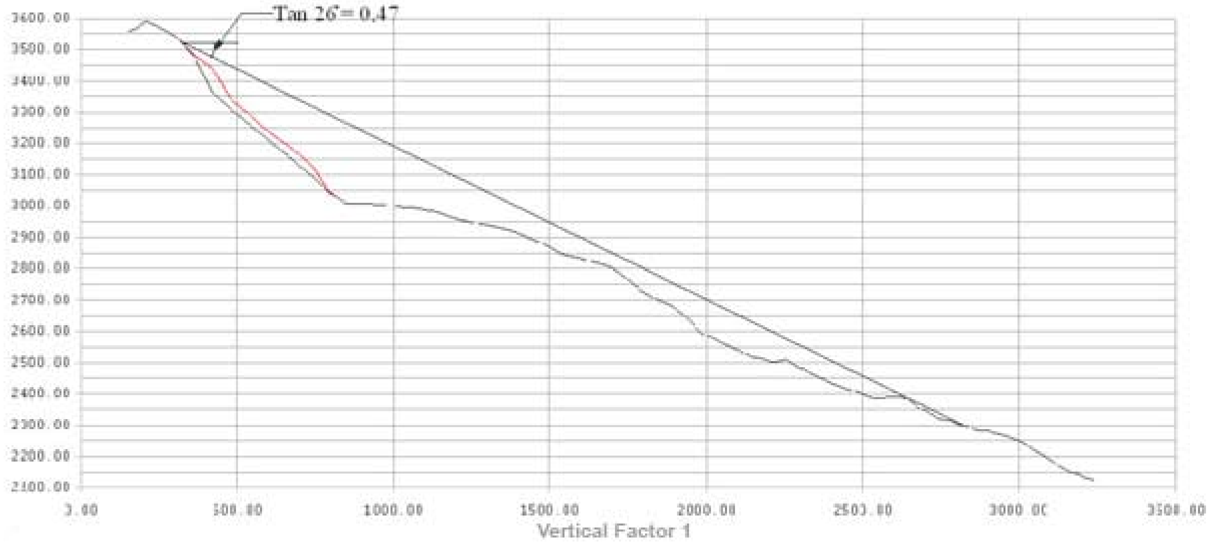

Figure 7.2 The Fahrböschung angle (26°) in Thurwieser case

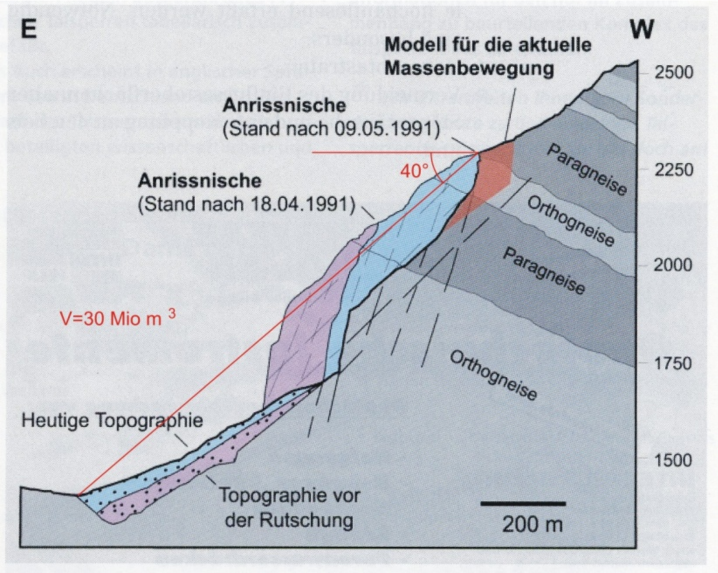

Figure 7.3 The Fahrböschung angle (40°) in Randa Rock Fall case (WAGNER, 1991)

It is known that smaller volumes reach steeper "Fahrböschungen" and vice versa (SCHEIDEGGER, 1973). Punta Thurwieser rock avalanche as well as Frank slide fit well into the data of this kind of mass movements (See Figure 7.1 and Figure 7.2). However, it cannot be assumed that the volume is the only influencing parameter for run out kinematics. Frank Slide and Randa Rock Fall had both approximately the same volume, but very different "Fahrböschungen". The detachment mechanisms (sliding, toppling, etc.; See Figure 1.2 and Figure 1.3), the morphology of the detachment surface (more or less flat, undulated surface etc.) have significant influence on the degree of loosening of the moving mass and on the trigger mechanism of the run out. The morphology of the pathway of the run out also has a great influence on run out kinematics (POISEL, PREH, & KOÇ, 2007). Thus finding the best fit parameters and an approximation of a real rockslide run out behavior are a demanding task and require in both cases numerous trial and error experiments.

8 Summary and End Notes

Rock mass falls, especially in mountain ranges like the Alps, belong to natural morphological phenomenon. If they occur near population areas, they comprise great hazard to the human life and to the nearby infrastructure. Thus it is very important to predict any possible occurrence and foresee the likely pathway of the rockslide, so that all precautions can be taken just in time.

The run out of a rock slope failure is a complex process (e.g. dust production, transformation of kinetic energy in heat etc.) (POISEL & ROTH, 2004) and they seldom possess only one reason for their occurrence. Geological conditions, relief, exposition to other effects and even permafrost are the basic parameters, which affect the instability (LATELTIN, 1997).

Modeling rock avalanche run out and predicting their intensity can provide a guidance to estimate the extent of the potential impact area and to design mitigation strategies. A reliable replication of the landslide dynamics requires a good description of the event characteristics to minimize the uncertainty associated to the trial and error calibration of the input parameters to be used in the model (CROSTA, HUNGR, SOSIO, & FRATTINI, 2007).

The Thurwieser rock avalanche is a good example of a rock mass movement for which a large amount of quantitative data has been gathered. The Thurwieser case is the first example of a large-scale rock avalanche which has been recorded on video. Thus the exact value of total duration, from initial position to final position, is available. Also the front velocities of the rock movement on its course in several sectors could be estimated. The landslide involved 2.5 M m^3 of dolomite and shale and traveled over 2.9 km from its original source partially in a glacial environment (CROSTA, HUNGR, SOSIO, & FRATTINI, 2007). The final geometry and characteristics of the deposit have been obtained by GPS measurements and aerial photos and field observations, which were documented by the Landslide Committee in Hong Kong for the attention of Benchmarking Exercise.

On the other hand the Frank Slide case was maybe the first rock avalanche in history, which triggered, due to massive loss of lives and structures, a detailed documentation and examination of possible causes of rock avalanches. The loss was great: a portion of the town was demolished with the moving mass, taking 70 lives with it and maybe because of that the landslide was named after the demolished town: Frank. McCONNELL and BROCK (1904) estimated the original rock mass volume from the deposit as 36.5 M m^3. Later it was reported by CRUDEN and KRAHN (1978) that the formation of the Turtle Mountain, in which the detached rock mass belong to, as dark grey limestone with a little chert. There also existed argillaceous and cherty layers of limestone. The aerial photos of the pathway, deposit margins and the detached rock mass origin has been reported by Landslide Committee for Benchmarking Exercise as in Thurwieser case.

The numerical analysis of the cases were carried out by the program *PFC* (developed by ITASCA CONSULTING GROUP), which is based on the basis of discontinuum mechanics and the distinct element method. A *PFC*-model is composed of two basic elements: two dimensional wall elements, which form in our case the pathway, the surface of the rock avalanche; three dimensional spherical particles (balls), which are used to model the detached rock mass in motion. These ball shaped particles can be positioned arbitrarily. The superiority of *PFC* from other simulation programs could be stated as follows: The program possesses an implemented language tool called *FISH*, which enables the user to calculate run out problems assigning contact models like rolling resistance. Second of all, the program provides at the end of the simulation a movie file, in which the camera view angle could be predefined also by the user. This movie feature of the program allows the user to investigate the constructed simulation thoroughly and makes possible for him to understand whether the model reflects a reasonable run out coinciding with the actual events.

With *PFC*, it is possible to model a rock avalanche, in which all the particle-wall interactions meaning motion types like free falling, bouncing, rolling and sliding are taken into account by the program (PREH & POISEL, 2007). However some adjustments should be taken to adapt the *PFC* model to a real rockslide motion. This adaptation was carried through the implemented *FISH* language, so that the existent contact and damping models could be modified and the requirements for a rockslide modeling could be fulfilled. The primary adaptations were for instance: the viscous (velocity proportional) damping and rolling resistance models.

In order to construct the surface wall elements, on which the running out of the simulation occurs, the digitalized data gathered from the Landslide Forum was used. With the help of the surveying program AUTODESK LANDDESKTOP 3 the predefined terrain points were reconstructed to assist and simplify the triangulation process of *PFC*.

Detecting the best fit parameters required a series of variation of parameters in both cases. The run outs were carried out over the final surface models, which were also divided into several regions according to the surface conditions of the terrain.

At the end it was possible to construct a close resemblance between the designed model and the real rockslide occurrence in both cases. Although the cases showed totally different behaviors, *PFC* successfully simulated the run outs, coinciding with reality.

The run out of a rock slope failure is a complex process (e.g. dust production, transformation of kinetic energy in heat). There is no method taking into account every aspect studied so far. Simulation of the run out of a particular rock slope failure by more than just one model is therefore strongly recommended. For example, PFC is not yet able to model the influence of water on the run out. Only analyses through a combination of methods make a comprehensive assessment of the run out close to reality possible (POISEL & ROTH, 2004).

9 Appendix

9.1 List of Figures used in the Text

9.2 List of Tables used in the Text

10 References

BAGNOLD, R. (1954). Experiments on gravity-free dispersion of large solid spheres in a Newtonian fluid under shear. *R. Soc. London, Proc. 225* , pp. 49-63.

BATHE, K., & WILSON, E. (1976). *Numerical Methods in Finite Element Analysis.* Englewood Cliffs: Prentice-Hall.

BOZZOLO, D. (1987). *Ein mathematisches Modell zur Beschreibung der Dynamik von Steinschlag.* Zürich: Dissertation Nr. 8490 an der ETH.

BROILI, L. (1974). Ein Felssturz im Grossversuch. *Rock Mechanics, Suppl. 3* , 69-78.

BROILLI, L. (1974). Ein Felssturz im Grossversuch. *Rock Mechanics, Suppl. 3* , pp. 69-78.

CRANDELL, D. (1968). *Avalanche, The encyclopedia of geomorphology.* Rheinhold New York.

CROSTA, G., HUNGR, O., SOSIO, R., & FRATTINI, P. (2007). Dynamic analysis of the Thurwieser rock avalanche, Italian Alps. *Geophysical Research Abstracts, Vol. 9* .

CRUDEN, D., & HUNGR, O. (1986). The debris of the Frank Slide and theories of rockslide-avalanche mobility. *Canadian Journal of Earth Sciences 23* , 425-432.

CRUDEN, D., & KRAHN, J. (1978). Frank Rockslide, Alberta, Canada. In B. VOIGHT, *Rockslides and Avalanches, 1 (Natural Phenomena)* (pp. 97-112). New York: Elsevier.

CRUDEN, D., & VARNES, D. (1996). *Landslide types and provesses.* Washington DC.: A.K. Turner and R.L. Schuster.

CUNDALL, P. (1971). A Computer Model for Simulating Progressive Large Scale Movements in Blocky Rock Systems. *Proceedings of the Symposium of the International Society of Rock Mechanics, Vol.1.* Nancy, France.

CUNDALL, P., & HART, R. (1992). *Numerical Modelling of Diskontinua.*

EVANS, S., & HUNGR, O. (1993). The assessment of rockfall hazard at the base of talus slopes. *Canadian geotechnical journal Vol. 30* , pp. 620-636.

FRÜHWIRT, T. (2004). *Numerische Untersuchungen von Felsmassenstürzen im Bereich der Grosshangbewegungen Galgenwald bei Murau mittels PFC3D.* Wien: Dippomarbeit an der TU Wien.

GEONET. (2007). Retrieved from http://www.geonet.org.nz/landslide/glossary.html

GERBER, W., BÖLL, A., RICKLI, C., & GRAF, F. (1995). *Schutzmassnahmen gegen Steinschlag.* Vitznau: FAN.

GINSBERG, J., & GENIN, J. (1984). *Dynamics.* New York: John Wiley and Sons.

GOODMAN, R., TAYLOR, R., & BREKKE, T. (1968). A model for the mechanic of jointed rock. *Journal of Soil Mechanics & Foundation Division, Proc. ASCE 94* , 637.

HAINBÜCHER, E. (2001). *Vergleich von analytischen Berechnungsverfahren mit dem Verfahren der Distinkten Element Methode bei geotechnischen Anwendungen.* Diplomarbeit an der Universität Essen.

HART, R. (1996). An Introduction to Distinct Modelling for Rock Engineering. *Comprehensive Rock Engineering, Vol 2.* , pp. 245-262.

HEIM, A. (1932). *Bergsturz und Menschenleben.* Zurich: Fretz und Wassermuth.

HSÜ, K. (1975). Catastrophic debris streams (Sturzstoms) generated by rockfalls. *Geological Society of America, Bulletin Vol. 86* , pp. 129-140.

HUNGR, O. (1995). A model for the runout analysis of rapid flow slides, debris flows, and avalanches. *Canadian Geotechnical Journal, Vol 32.* , 610-623.

ITASCA. (2007). Retrieved from http://www.itascacg.com/pfc_dem.html

ITASCA. (2006). *User's Manual, PFC 3D.* Minnesota.

IVERSON, R. (1997). The physics of debris flows. *Reviews of Geophysics, Vol. 35* , pp. 245-296.

IVERSON, R., COSTA, J., & LAHUSEN, R. (1992). Debris flow flume at H.J. Andrews Experimental Forest, Oregon, U.S. *U.S. Geological Survey Open-file report* , p. 483.

LATELTIN, O. (1997). Berücksichtigung der Massenbewegungsgefahren bei raumwirksamen Tätigkeiten. (B. B. BRP, Ed.) Bern.

MAIR am TINKHOF, K. (2007). *Numerische Untersuchung von Felsmassenstürzen vom Roten Kögele am Hallstätter Salzberg mittels PFC3D.* Wien: Diplomarbeit an der TU Wien.

MAJOR, J., & IVERSON, R. (1999). Debris flow deposition - effects of pore fluid pressure and friction concentrated at flow margins. *Geological Society of America Bulletin, 111* , pp. 1424-1434.

McCONNELL, R., & BROCK, R. (1904). *Report on the great landslide Frank, Alberta, Canada.* Alberta: Can. Dep. Inter., Annu. Rep.

McCONNELL, R., & BROCK, R. (1904). *The great landslide at Frank, Alberta.* Annual Report 1902-1903.

MINDLIN, R., & DERESIEWICZ, H. (1953). Elastic Spheres in Contact under Varying Oblique Forces. *Journal of Applied Mechanics, 20* , pp. 327-344.

MITCHELL, J. (1976). *Fundamentals of soil behavior.* New York: John Wiley & Sons, Inc.

Organising Committee of "The 2007 International Forum on Landslide Disaster Management, H. K.-L. (2007). Retrieved from www.hkieged.org/LDM2007/index.htm

PETJE, U., MIKOS, M., & MAJES, B. (2006). Motion of rock masses on slopes. *Geologija 49/2* , pp. 393-408.

PIRULLI, M. (2004). Numerical analysis of three potential rock avalanches in the alps. *Felsbau 22, Vol. 2* .

PIRULLI, M. (2005). *Numerical modeling of landslide runout, a continuum mechanics aproach.* Torino.

PIRULLI, M., DELINE, P., MANGENEY, A., MORTARA, G., NOETZLI, J., SCAVIA, C., et al. (2006). The Thurwieser rock avalanche, Ortles-Cevedale Group (Italian Alps): description and dynamic analysis. *Geophysical Research Abstracts, Vol 8* .

POISEL, R., & PREH, A. (2004). Rock slope initial failure mechanisms and their machanical models. *Felsbau 22* , pp. 40-45.

POISEL, R., & ROTH, W. (2004). Run Out Models of Rock Slope Failures. *Felsbau 22* , 46-50.

POISEL, R., PREH, A., & KOÇ, O. (2007). Punta Thurwieser Rock Avalanche and Frank Slide a Comparison based on PFC3D runout models. *The 2007 International Forum on Landslide Disaster Management.* Hong Kong.

POISEL, R., PREH, A., & KOÇ, O. (2007). Punta Thurwieser Rock Avalanche and Frank Slide a Comparison based on PFC3D runout models. *The Presentation at the 2007 International Forum on Landslide Disaster Management, Benchmarking Exercise on Landslide Mobility.* Hong Kong.

POULIQUEN, B., & FORTERRE, Y. (2002). Friction law for dense granular flows: application to the motion of a mass down rough inclined plane. *Journal of Fluid Mechanics, Vol. 453* , 133-151.

PREH, A. (2004). *Modellierung des Verhaltens von Massenbewegungen bei großen Verschiebungen mit Hilfe des Particle Flow Codes (PFC).* Wien: Dissertation an der TU Wien.

PREH, A., & POISEL, R. (2007). 3D Modeling of Rock Mass Falls using the Particle Flow Code PFC. *11th Congress of the International Society for Rock Mechanics.* Lisbon.

PREH, A., & POISEL, R. (2007). 3D modelling of rock mass falls using the Particle Flow Code PFC3D. *11th Congress of the International Society for Rock Mechanics.* Lisbon.

RITCHIE, A. (1963). Evaluation of Rockfall and its control. *Highway research record 17* , pp. 13-28.

ROTH, W. (2003). Dreidimensionale numerische Simulation von Felsmassensturzen mittels der Methode der distinkten Elemente (PFC). *PhD Thesis, Vienna University of Technology* .

SASSA, K. (1988). Geotechnical model for the motion of landslides. In C. BONNARD, *Proc. 5th Int. Symposium on Landslides, Vol. 1* (pp. 37-55). Lausanne, Switzerland.

SAVAGE, S., & HUTTER, K. (1989). The motion of a finite mass of granular material down a rough incline. *Journal of Fluid Mechanics, Vol. 199* , 177-215.

SCHEIDEGGER, A. (1973). On the prediction of the reach and velocity of catastrophic landslides. *Rock Mechanics, Vol. 5* , 231-236.

SCHEIDEGGER, A. (1973). On the Prediction of the Reach and Velocity of Catastrophic Landslides. *Rock Mechanics 5* , 231-236.

SOSSIO, R., & CROSTA, G. (2007). Thurwieser rock avalanche. *International Forum on Landslide Disaster Management in Hong Kong* (pp. 1-3). Hong Kong: University Milan.

SPANG, R., & SÖNSER, T. (1995). Optimized rockfall protection by "Rockfall". *Proc. 8th Int. Rock Mech., Vol. III* , pp. 1233-1242.

USGS. (2007 , July 05). *Landslides 101*. Retrieved December 24, 2007, from http://landslides.usgs.gov/learning/ls101.php

VARNES, D. (1978). Slope movement types and processes. *Landslide, analysis and control: transportation research board* (pp. 11-33). Washington DC.: National Academy of Sciences.

WAGNER, A. (1991). Bergsturz Grossgufer Randa. *Etude structurale et géoméchanique* .

WIKIPEDIA. (2007). Retrieved 2007, from http://en.wikipedia.org/wiki/Ortler_Alps

WILL, J., & KONIETZKY, H. (1998). Neue Techniken der Numerik zur Berechnung von Felsböschungen. *Felsbau 16* , 155-167.